Improving polymer electrolyte fuel cell performance through optimizing flow channels and catalyst layers

Jinbei Tian

Submitted in accordance with the requirements for the degree of

Doctor of Philosophy

The University of Sheffield
Faculty of Engineering
Department of Mechanical Engineering

September 2023

Declaration

I, the author, confirm that the thesis is my own work, and that appropriate credit has been given where reference has been made to the work of others.

This copy has been supplied on the understanding that it is copyright material and that no quotation from the thesis may be published without proper acknowledgement. I am aware of the University's Guidance on the Use of Unfair Means (https://www.sheffield.ac.uk/new-students/unfair-means.).

Publications

Published Journal Papers

1.Tian J, Ismail MS, Ingham DB, Hughes KJ, Ma L, Pourkashanian M. "Multiphase, three-dimensional PEM fuel cell numerical model with a variable cross-sectional area flow channel", International Journal of Numerical Methods for Heat & Fluid Flow. 2023 May 11. - Chapter 3

https://doi.org/10.1108/HFF-02-2023-0075

Journal Papers in Preparation

2. Tian J, Ismail MS, Ingham DB, Hughes KJ, Ma L, Pourkashanian M. Influence of catalyst agglomerate internal structure on PEFC performance investigated by a multiscale numerical model, to be submitted to a special issue in Fuel Journal in October - Chapter 5

3. Tian J, Ismail MS, Ingham DB, Hughes KJ, Ma L, Pourkashanian M. Influence of the agglomerate shape of catalyst on the PEM fuel cell performance investigated by a multiscale model, to be sent to Energies Journal in October - Chapter 6

Acknowledgments

I would like to express my deepest gratitude to Dr. Mohammed S. Ismail. Throughout my entire doctoral journey, he has been an invaluable source of guidance and support, shared with me his profound knowledge and help me overcome all obstacles and challenges. My sincere gratitude is to Prof. Derek B. Ingham who consistently provided timely feedback, "well done" and "keep going," and he has become an essential motivator for me to complete my PhD. I would like to thank my supervisor, Prof. Mohamed Pourkashanian, for his unwavering support. My sincere appreciation also goes to Prof. Lin Ma and Kevin J. Hughes for their expertise, invaluable advice, and the equipment and software support they have provided.

I would like to thank my dear friends Wenjun, Guojun, and Jialun. Thank you for your unconditional support during my toughest times. I would like to express my gratitude to the members of the fuel cell research group: Fatma, Mustafa, Fernando, Fahad, Isaac, Florence, Qizhi, and Dr. Ahmed. It has been my privilege to learn alongside all of you, and I will cherish the wonderful times we spent together in meetings, having coffee, and chatting. I'd like to express my appreciation to my friends from Energy 2050: Karim, Fernanda, Mohammed, Marcin, Lucas, Rahima, JP, Nick, Nicholoy, and Qiulin. Your laughter and companionship have truly enriched these four years.

I am deeply grateful to my parents, sister, and brother. Thank you for your love and support; you have shaped me into a positive, confident, and grateful individual. I hold immense love for all of you.

Abstract

Proton exchange membrane (PEM) fuel cells show great promise and are becoming more prevalent in both the automotive and stationary applications. To enhance their commercial viability, continuous efforts are essential to improve the performance and reduce costs. Consequently, the primary objective of this thesis is to conduct numerical investigations aimed at optimizing the flow channel configuration and the microstructure of the catalyst agglomerate, with the ultimate goal of enhancing fuel cell performance and cost-effectiveness.

Flow-field plates (also known as bipolar plates) are a critical component of proton exchange membrane fuel cells. Their primary function is to house grooves or flow channels responsible for delivering reactant gases to the catalyst layers, where half-reactions occur, via the gas diffusion layers (GDLs). Additionally, they play a vital role in (i) expelling excess water from the core of the fuel cell, which is the membrane electrode assembly (MEA), and (ii) establishing electrical connections between the anodes and cathodes within the fuel cell stack. The impact of the flow channel cross-sectional shapes has been extensively explored in the literature. In this study, optimization to the geometric configuration of the flow channels has been performed. Specifically, a novel and comprehensive three-dimensional multiphase numerical model that combines both conventional square gas flow channels and trapezoidal flow channels has been developed. The proposed "hybrid" configuration flow channel gradually reduces in the cross-section along the direction of gas flow. Unlike similar flow channel configurations proposed in the literature, the "hybrid" flow channel preserves the contact area between the flow channel and the GDL. This not only increases the gas velocity but also facilitates improved reactant exchange and liquid water removal.

The catalyst layer is another important component of PEM fuel cells; it has the following functions: provision of reaction sites for Oxygen Reduction Reaction (ORR) or Hydrogen Oxidation Reaction (HOR), provision of pores for the diffusion of reactants (Oxygen or Hydrogen), provision of the solid phase for electron transfer, provision of membrane phase for ion transfer, and the provision of channels for the transfer of liquid water generated by ORR in the cathode side. It is necessary for the catalysts layer to meet the following requirements: high efficiency, low price and durability. Platinum has always been the best catalyst of choice, but due to its high price and ease to be poisoned, it has prevented PEM

fuel cells from being more widely used. Low-platinum loading and platinum-free catalysts are of great scientific interests; however, further experimental and theoretical investigations are needed. Having reviewed the relevant literature, many research gaps in the knowledge concerning the influence of shape, composition, structural modification and material of the catalyst particles have been identified. For example, the influence of the internal structure and the shape of the agglomerates on the local and/or global performance of the fuel cell has not been well-researched. Multi-scale modelling of the catalyst layer could substantially save time and cost, that are normally associated with the trial and error of the experimentation, and potentially result in designing catalysts that have a positive effect on the efficiency and lifetime of the fuel cell. In this report, a multi-scale numerical model for PEMFCs has been developed. The effects of some key factors of the catalyst (i.e. the platinum loading, the particle size, active surface, the internal structure of the agglomerates, the shape of the agglomerates) on the fuel cell performance have been numerically investigated.

The findings indicate that fuel cells featuring hybrid flow channel cross-sections consistently outperform other configurations, especially under high current densities. Additionally, the results show that the substantial impact of catalyst particle parameters, including platinum loading, particle size, and active surface area, as well as the agglomerate's internal arrangement, shape, and size on the overall fuel cell performance. Optimizing these factors not only enhances performance but also offers the potential for cost reduction.

Contents

List of Tables

List of Figures

Nomenclature

c_p	Specific heat capacity, J/(kg.K)
D_k^{eff}	Effective diffusion coefficient for species k
C_k	Concentration of species k, kg/m^3
D	Diffusion conductance at the face of the control volume
F	Faraday constant, C/mol
i	Current density, A/m^2
K	Permeability, m^2
M_k	Molecular weight of species k, kg/mol
Mw	Molecular weight, kg/mol
P	pressure, Pa
R	Universal gas constant, $Pa.m^3/(mol.K)$
$S_{s,k}$	Source term for species k
S_φ	Charge source term
S	Source term in the conservation equation
S_e	Energy source term
S_m	Mass source term
S_M	Momentum source term
T	Temperature, K
t	time, s

V	Control volume
v	Velocity in x-direction
v	Velocity vector, m/s
Y_k	Mass fraction for species k

Greek symbols

∅	General variable in the conservation equation
φ_m	Electrolyte phase potential, V
φ_s	Solid phase potential, V
μ	Fluid viscosity, Pa.s
ε	Porosity of the porous medium.
ρ	Density, kg/m^3
$\boldsymbol{\Gamma}$	Diffusion coefficient in the conservation equation
δ	The thickness of porous medium, m

Subscripts

Unless stated otherwise, all the subscripts in this thesis are given as follows:

k	Species k
eff	Effective value
o	Reference

Superscripts

Unless stated otherwise, all the superscripts in this thesis are given as follows:

eff	Effective value
′	Corrected value
*	Updated value

Abbreviations

AFC	Alkaline fuel cell
CCM	Catalyst coated membrane
CFD	Computational fluid dynamics
DMFC	Direct methanol fuel cell
GDL	Gas diffusion layer
MCFC	Molten carbonate fuel cell
MEA	Membrane electrode assembly
MPL	Microporous layer
PAFC	Phosphoric acid fuel cell
PEMFC	Proton exchange membrane fuel cell
PTFE	Ploytetraflouroethylene
SEM	Scanning electron microscope
SOFC	Solid oxide fuel cell

Chemical symbols

CO	Carbon monoxide

CO_2	Carbon dioxide
H^+	Proton
H_2	Hydrogen molecule
H_2O	Water molecule
O_2	Oxygen molecule

Chapter 1 Introduction

1.1 Background of fuel cells

Global warming due to excessive greenhouse gas emissions is an international concern. However, fossil fuels are still the main source of energy. This will cause serious environmental problems and worsen the trend of global warming. To comply with the Paris Agreement, it is necessary to reduce the global temperature to below 1.5°C per annum [1]. It is, therefore, crucial to develop clean and sustainable energy technologies that can be universalised. Fuel cells are a promising renewable energy device that can be distributed around the world regardless of weather and geographical conditions. Compared with traditional fossil fuels, hydrogen energy is more sustainable, and hydrogen and water can be converted into each other. Hydrogen energy can be converted into electrical energy through fuel cell technology. Fuel cells can be used as renewable energy to compensate for seasonal changes in energy supply, but can also be used to compensate for the daily mismatch in the energy supply and demand [2]. Also, fuel cells have the advantages of higher energy conversion efficiency, less pollution, and lower noise and maintenance cost. All these advantages have made the fuel cells to become a good candidate to be the power unit in different scenarios.

A fuel cell is an electrochemical reaction device that converts chemical energy in fuel and oxidant into electrical energy through redox reactions. Unlike most batteries, fuel cells require continuous fuel and oxidant to maintain chemical reactions. However, the chemical energy in a battery is generally derived from metals and their ions or oxides, except for the flow in batteries. The fuel cell can continuously generate electricity as long as there is a continuous supply of fuel and oxidant. However, the performance of the battery will decrease

as the charge decreases [3]. This advantage makes fuel cells more promising than most batteries.

Sir Willam Grove invented the first fuel cell in 1838. More than a century later, another scientist, Francis Thomas Bacon, invented the hydrogen-oxygen fuel cells in 1932. NASA has applied alkaline fuel cells in the space program to power satellites and space capsules since the mid-1960s. In 1955, Thomas Grubb further improved the fuel cell by using a sulfonated polystyrene ion-exchange membrane as the electrolyte of the fuel cell [2]. Fuel cells are now used in many different devices and are used as the main and backup power sources in different places such as commercial, industrial and civil buildings and remote or inaccessible regions. Also, fuel cells are used as the power source in vehicles including automobiles, ships, submarines, spaceships, etc.

The performance and energy efficiency of a fuel cell is largely influenced by the thermodynamics, electrode dynamics, electrochemistry, reactant mass transfer, fluid mechanics, and the materials and components that make up a fuel cell [2]. These influencing factors have been extensively studied by scientists in the past decades and many improvements have been made to fuel cells. To enable the fuel cell to be widely used, there are still many problems that need to be solved urgently: (i) reducing the system cost, especially membrane electrodes, (ii) enhancing the reliability and durability of the system, (iii) improving the production, transportation and storage of hydrogen, and a series of supporting technologies, and (iv) enhance the system performance, efficiency and power density [4].

1.2 Basics of the fuel cells

A fuel cell is an electrochemical device that converts chemical energy into electrical energy. In the fuel cell, the fuel is continuously transported to the anode and the oxidant, in most

cases it is the oxygen from the air, is continuously transported to the cathode. The redox reaction occurs continuously in the electrode under the action of the catalyst, and the ions flow through the electrolyte, and, at the same time, water is generated at the cathode, and the current is generated in the external circuit and this provides power to the external load.

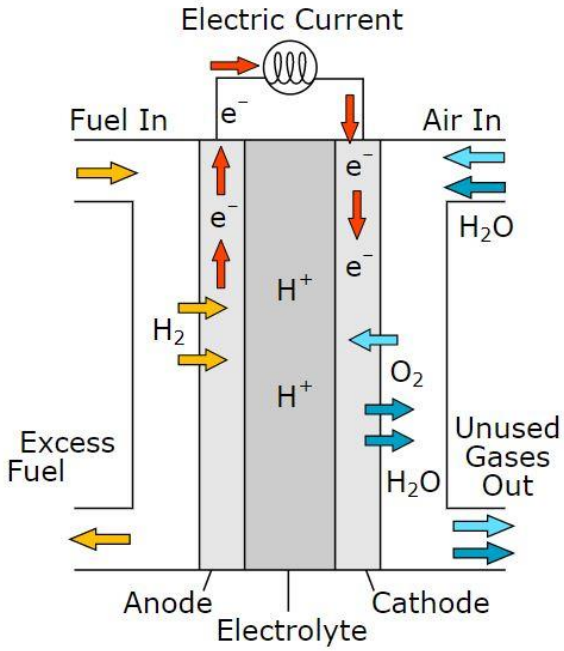

Figure 1.1 Schematic of the Working Principle of a PEM Fuel Cell.

Anode side:

$$2H_2 = 4H^+ + 4e^- \tag{1.1}$$

Cathode side:

$$O_2 + 4H^+ + 4e^- = 2H_2O \tag{1.2}$$

Overall reaction:

$$2H_2 + O_2 = 2H_2O \tag{1.3}$$

Hydrogen is split into protons and electrons at the anode under the action of catalyst oxidation, Equation (1.1), and oxygen undergoes a catalytic reduction reaction at the cathode, Equation (1.2). The protons, transmit from anode to cathode, pass through the electrolyte, and the electrons are forced to reach the cathode electrode through an external circuit with a load. Here the electrons combine with the oxygen and protons and eventually generate water, Equation (1.3) [5].

1.3 Different fuel cells and applications

According to the different operating temperatures and electrolytes, there are six types of fuel cells and each of them can be applied according to different demands. Table 1.1 lists their electrolyte, working temperature, efficiency, and cost[6].

Table 1.1 Comparisons of the of Fuel Cell Technologies.

Fuel Cell Type	Electrolyte	Working Temperature (°C)	Efficiency		Cost (USD/W)
			Cell	System	
Proton Exchange Membrane Fuel Cell	Polymer membrane (ionomer)	50–100 (Nafion) 120–200 (PBI)	50–70%	30–50%	50–100
Direct Methanol Fuel Cell	Polymer membrane (ionomer)	90–120	20–30%	10–25%	125

Fuel Cell Type	Electrolyte	Working Temperature (°C)	Efficiency		Cost (USD/W)
			Cell	System	
Phosphoric Acid Fuel Cell	Molten phosphoric acid (H3PO4)	150–200	55%	40% Co-gen: 90%	4.00–4.50
Alkaline Fuel Cell	Aqueous alkaline solution	< 80	60–70%	62%	
Solid Oxide Fuel Cell (SOFC)	Yttria stabilized zirconia	850–1100	60–65%	55–60%	
Molten Carbonate Fuel Cell	Molten alkaline carbonate	600–650	55%	45–55%	

Fuel cells can be used to generate and supply power in portable devices and distributions. However, a single fuel cell is too small to power most equipment, so they need to be connected in series and stacked together, and this is called the "fuel cell stack". In the stack, the voltage is proportional to the number of the fuel cells, and the current is proportional to the area of the electrodes. Because the range of power that a fuel cell can cover is very large, it can be applied to a variety of scenarios, from fixed power stations to many different portable devices such as vehicles and mobile phones. There are mainly four applications categories: vehicles, fixed power, backup power, and portable power[7].

Many studies have focused on replacing internal combustion engines with fuel cells. The main reason for the development of the automotive fuel cell technology is its high efficiency, low emissions or zero emissions, and the ability to produce fuel locally rather than rely on imported fuel. The typical running time of a vehicle is about 3000 to 5000 hours, and the bus is one of the most suitable types of vehicles for the application of the fuel cell technology in the early stages. The life expectancy of bus engines is longer because usually a city bus can run more than 6000 hours per year on average and start and stop many times. However, the longer service life and intermittent operation pose great challenges to the durability of fuel cells[8].

1.3.1 Direct methanol fuel cell (DMFC)

The direct methanol fuel cell DMFC is a subcategory of proton-exchange fuel cells in which methanol is used as a fuel. Its main advantage is that methanol is easier to transport as a liquid fuel because methanol can maintain a stable energy density under most environmental conditions. The efficiency of this kind of fuel cell is quite low, namely only about 10%, and therefore it is more widely used in portable devices that require a higher energy density [9].

The working mechanism of the PEMFC is schematically presented as figure 1.2, methanol is oxidized in the catalyst layer of the anode where carbon dioxide is formed. Protons (H +) are formed in the electrode at the anode side and transported through the proton exchange membrane to the cathode. Then the proton reacts with oxygen to form water at the cathode. The electrons peeled off from hydrogen are transported from the anode to the cathode through an external circuit, thereby powering the connected equipment [10].

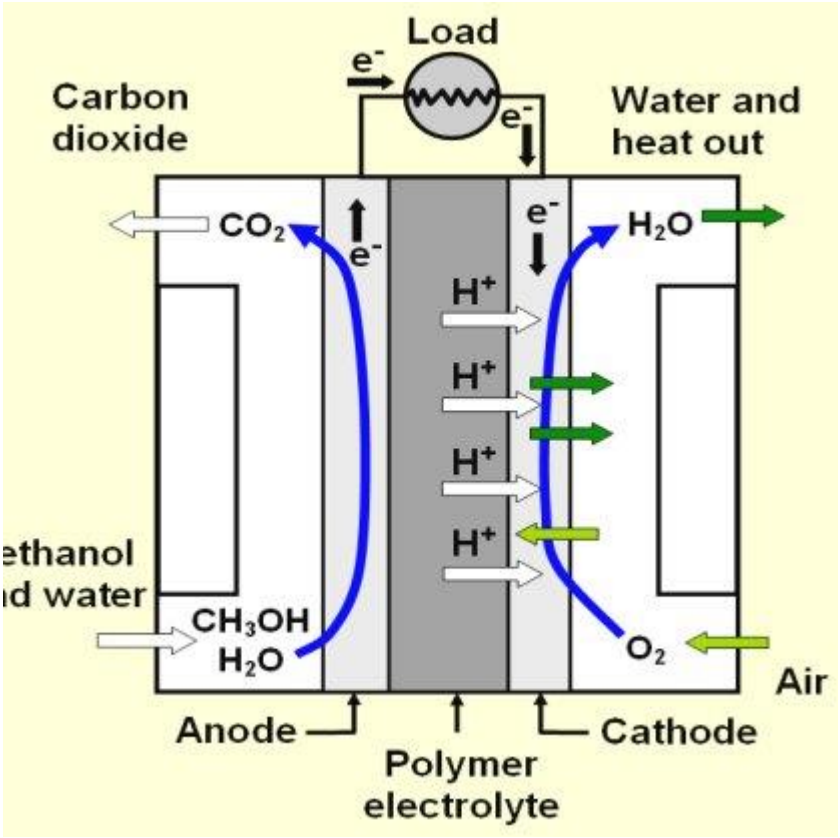

Figure 1.2 Schematic of the Direct Methanol Fuel Cell.

The governing reactions for the DMFC are as follows:

Anode side:

$$2CH_3OH + H_2O = 6H^+ + 6e^- + CO_2 \tag{1.4}$$

Cathode side:

$$\frac{3}{2}O_2 + 6H^+ + 6e^- = 3H_2O \tag{1.5}$$

Overall reaction:

$$CH_3OH + \frac{3}{2}O_2 = 2H_2O + CO_2 \tag{1.6}$$

At the anode of the fuel cell, methanol and water lose protons and generate carbon dioxide under the action of the catalyst, Equation (1.4). At the cathode of the fuel cell, oxygen reacts with hydrogen protons to form water, Equation (1.5). The overall reaction process is a redox reaction of methanol and oxygen, and the final products are water and carbon dioxide, Equation (1.6).

1.3.2 Solid oxide fuel cells (SOFC)

SOFC is different from other fuel cells because, in this fuel cell, the flow direction of ions is opposite to that of other fuel cells, oxygen ions flow from the cathode to the anode. Oxygen enters through the cathode, where it absorbs the electrons to produce oxygen ions, Equation (1.8), and then the oxygen ions pass through the membrane and react with the hydrogen at the anode, Equation (1.7). Water is produced as a by-product at the anode side, electricity is also generated. Sometimes the by-product includes carbon dioxide which depends on the fuel used in the fuel cell. The chemical reactions that occur in the SOFC system can be expressed as follows:

Anode side:

$$2H_2 + 4OH^- = 4H_2O + 4e^- \quad (1.7)$$

Cathode side:

$$O_2 + 4e^- 2H_2O = 4OH^- \quad (1.8)$$

Overall reaction:

$$2H_2 + O_2 = 2H_2O \quad (1.9)$$

The electrolyte of a solid oxide fuel cell is a solid material, such as a ceramic material called yttria-stabilized zirconia and their working temperature is 800-1000 ° C. The working

efficiency can reach 80-85%, and they can run under a variety of fuels and they have less dependence on the precious metals. However, the start-up is slow due to the high operating temperature, and it is not suitable for applications such as in vehicles that require a fast startup [11].

1.3.3 Alkaline fuel cells (AFC)

The alkaline fuel cells, also known as bacon fuel cells, were invented by the British scientist Francis Thomas Bacon. The operating temperature of alkaline fuel cells is 27-90 ° C, and their electrical efficiency is higher than that of the proton exchange membrane fuel cell. (PEMFC). Because it is an alkaline chemical, the ORR at the cathode is much easier than that in acid batteries, thus allowing non-precious metals such as iron, cobalt, or nickel to be used at the anode [12]. The reactions are given as follows:

Anode side:

$$2H_2 + 4OH^- = 4H_2O + 4e^- \quad (1.10)$$

Cathode side:

$$O_2 + 4e^- 2H_2O = 4OH^- \quad (1.11)$$

Overall reaction:

$$2H_2 + O_2 = 2H_2O \quad (1.12)$$

Although the AFC has the advantages of high efficiency and fast start-up and does not depend on platinum-based catalysts, because potassium hydroxide is highly corrosive, thus leakage in the AFC becomes the biggest problem and even though with the tightest seal, it also has a natural leakage trend. Another problem is that if the electrolyte circulates too fast,

or the spacing between the batteries is not enough, and this may cause a short circuit inside the battery.

1.3.4 Molton carbonate fuel cells (MCFC)

Similar to the SOFC, the working temperature is 650 ° C in the MCFC. The electrode of MCFC is lithium potassium carbonate, which transfers to the liquid phase at high temperatures, thus allowing the negative carbonate ions to move inside the battery. Besides, in the anode of MCFC hydrogen-rich gas is formed by converting fossil fuels. There is no need to produce hydrogen externally. In the electrolyte the hydrogen gas reacts with the carbonate ions, the products are water, carbon dioxide, electrons, and small amounts of other chemicals. The electrons transferred through an external circuit and generate before returning to the cathode[9]. Oxygen and carbon dioxide are recovered by reacting with electrons to form carbonate ions, thereby replenishing the electrolyte and forming an electric current. The chemical reaction in MCFC can be expressed as follows[13]:

Anode side:

$$CO_3^- + H_2 = 2H_2O + CO_2 + 2e^- \tag{1.13}$$

Cathode side:

$$CO_2 + \frac{1}{2}O_2 + 2e^- = {CO_3}^{2-} \tag{1.14}$$

Overall reaction:

$$H_2 + \frac{1}{2}O_2 = H_2O \tag{1.15}$$

The main advantages of MCFC are the use of hydrocarbon fuel, low catalyst cost, high efficiency, low sensitivity to poisoning, and fast kinetics. However, due to the characters of

its electrolyte and the required working temperature, the MCFC also has many drawbacks. For example, carbonates are extremely corrosive at high temperatures. Moreover, extra fuel needs to be consumed to heat the fuel cell during startup. The main drawbacks of the MSFC are a slow start-up and response, reduced material selection for the high temperatures, complex fuel cell systems for CO2 cycling, and corrosive electrolytes [14].

1.3.5 Phosphoric acid fuel cells (PAFC)

Phosphoric acid fuel cell is the earliest commercial fuel cell, its electrolyte is liquid phosphoric acid. The working temperature range of PAFC is about 150 to 210°C, and the finely dispersed platinum catalyst is evenly coated on the carbon paper as the electrode. Due to its high working temperature, the discharged water is generally high-temperature steam which can be used to heat air or water. This feature makes the APFC able to be used as a distributed power supply heating device [15]. The governing reactions are as follows:

Anode side:

$$2H_2 = 4H^+ + 4e^- \tag{1.16}$$

Cathode side:

$$O_2 + 4H^+ + 4e^- = 2H_2O \tag{1.17}$$

Overall reaction:

$$2H_2 + O_2 = 2H_2O \tag{1.18}$$

This has the potential to increase the efficiency by up to 70%. Besides, the PAFCs are resistant to carbon dioxide and can even tolerate CO concentrations of about 1.5%, which expands the range of fuels they can use. Although phosphoric acid is a poor ionic conductor at lower temperatures, this leads to more serious CO poisoning of the platinum

electrocatalyst at the anode. Even so, compared with PEMFC and AFC, PAFC is still less sensitive to CO. The disadvantages of PAFC are as follows: lower power density and corrosive electrolyte [15].

1.3.6 Proton exchange membrane fuel cell (PEMFC)

As seen from Figure 1.2, in a typical hydroxide PEMFC, the MEA layer is the most important component, which contains a proton exchange membrane (usually nafion) and a cathode and anode catalyst layer.

Hydrogen diffuses to the anode catalyst and then breaks down into protons and electrons. Protons are conducted to the cathode through the membrane and react with the oxidant. Because the membrane is electrically insulating, the electrons are forced to conduct and power the load in the external circuit. In the cathode catalyst layer, oxygen molecules react with electrons and protons to produce water under the action of the catalyst.

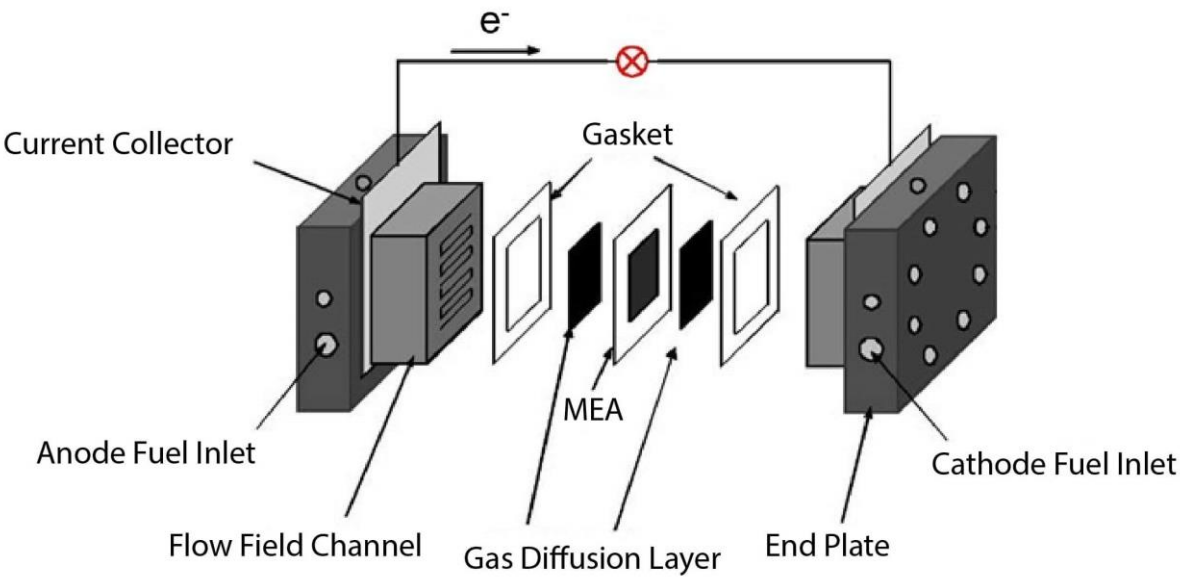

Figure 1.3 Schematic of the Fuel Cell Components.

The components of PEMFC are schematically presented in Figure 1.2: and this consists of a bipolar plate, electrode, catalyst, membrane, and other necessary hardware[16].

Different types of fuel cells use different materials. The main types of bipolar plates are the following: metals, coated metals, graphite, flexible graphite, CC composite materials, carbon polymer composite materials, etc. [17]. The MEA layer is the most important part of the PEMFC and is usually made of two catalyst-coated carbon papers and a proton exchange membrane between them. At present, platinum or similar types of precious metals and their alloys are commonly used in fuel cells as PEMFC catalysts [18].

Flow field plate is an important component of fuel cells, it plays an important role in the distribution of gas, electrical conductivity, thermal conductivity, and drainage in fuel cells, and their performance depends largely on the flow field structure. Single cells are connected in series to form a stack, and each cell is composed of a bipolar plate and a membrane electrode assembly[19]. At present, graphite and metal are usually the main materials of bipolar plates. Graphite has the advantages of good conductivity, corrosion resistance, and stability. Although it is expensive and difficult to process, it is still a common material for fuel cell bipolar plates [20]. As the demand for fuel cells increases, the disadvantage of fuel cells that use graphite as a bipolar plate is becoming increasingly clearer. The advantage of the metal bipolar plate is that it is easy to process, and the cost is lower than graphite. Because it can be processed to be very thin, the thickness of the fuel cell can be reduced. Generally, the flow field is formed on the plate by mechanical processing or chemical etching. The structure of the flow field constitutes the most important feature of the bipolar plate, which directly affects the performance of the stack. The bipolar plate uses various shapes of flow field channels to send the reactants into the electrode. At present, the gas channels on the bipolar plate mainly include : parallel flow channels, serpentine flow channels and interdigitated flow channels[21]. The schematics of different shapes of bipolar plates are presented in Figure 1.4. Among them, the limit current of the serpentine flow field is the largest and the output is stable within the operating current range, but the voltage drop of the

serpentine flow field is also the highest. In addition, parallel flow fields and interdigitated flow fields have higher water content.

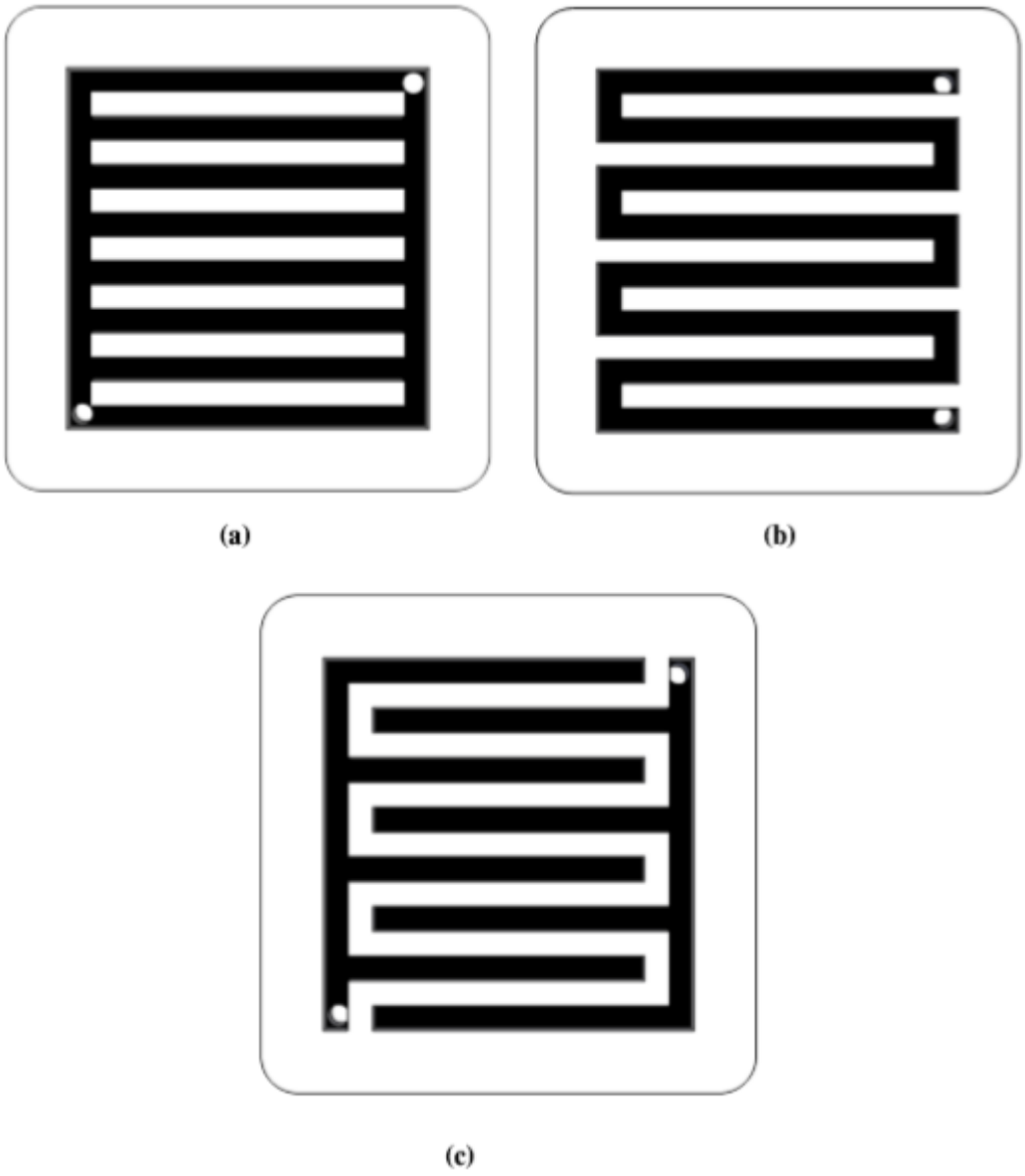

Figure 1.4 Schematics for (a) parallel, (b) serpentine, and (c) interdigitated channels [22]**.**

Gas diffusion layer (GDL) is one of the most important components of the PEM fuel cell. The role of the GDL is to transport reactants and products to and from the reaction site, as well as to conduct the heat and current. The GDL generally uses porous composite materials with a thickness of 100 to 300 microns. In the GDL, the carbon can ensure the conductivity,

and PTFE brings hydrophobic. Figure 1.6 is a cross-sectional view of the gas diffusion layer and MEA, reflecting the microstructure of the GDL, which ensures the reactants and water can transport to the catalyst layer [23]. The ideal GDL has the following characteristics: excellent gas diffusion performance, porosity, surface contact angle, air permeability, water vapour diffusion, hydrophobicity, hydrophilicity, corrosion resistance, crack-free surface morphology, oxidation stability, and durability under various working conditions. By optimizing the composition of the diffusion layer, it can even substantially improve the overall performance and stability of the fuel cell [24].

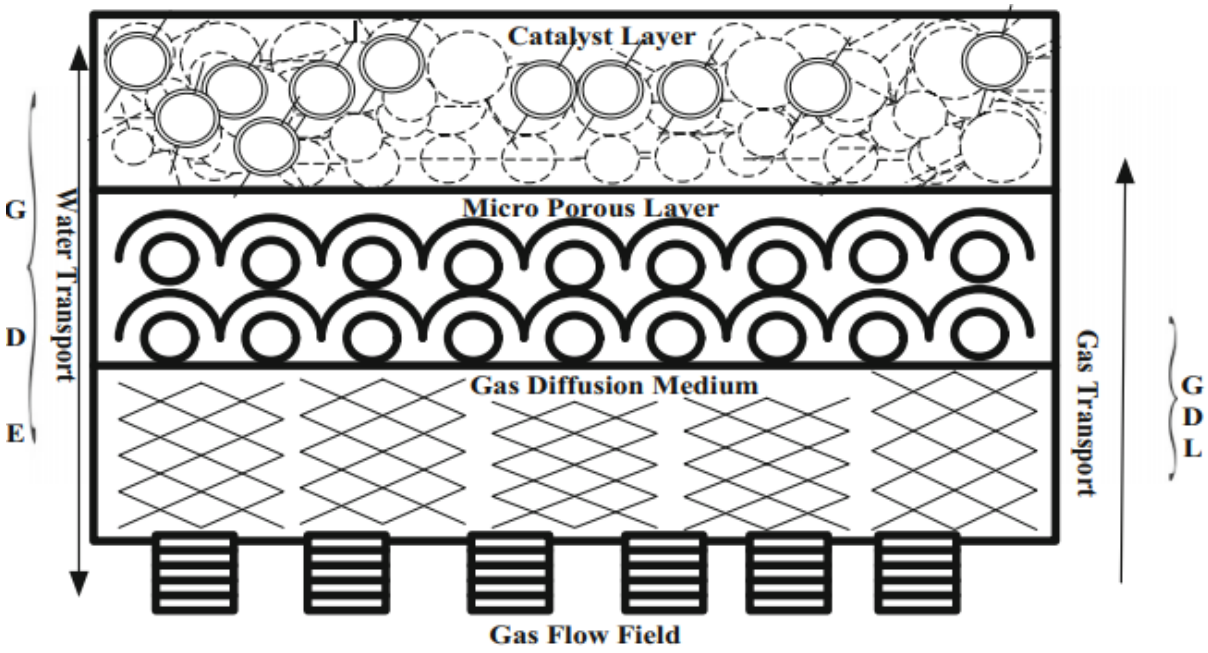

Figure 1.5 Schematics of the GDL, MPL and CL microstructure [24]**.**

The catalyst layer (CL) is one of the components of the MEA layer, which has a huge impact on the performance of PEMFC, mainly composed of electrolyte and catalyst particles, and a gas diffusion layer on the side of the bipolar catalyst. Studies have shown that the main reaction occurs at the catalyst particle/electrolyte (ionomer) interface, and there are a large number of similar interfaces in the catalyst layer to provide active sites for the catalytic reaction [25]. In the cathode catalyst layer, the slow oxygen reduction reaction rate is one of

the limiting factors. At present, the catalyst used in PEM is Pt, and both the low ORR rate and the high cost limits the widespread application of fuel cells [26]. The oxygen reduction reaction (ORR) in the cathode occurs at a comparatively slow rate. The most widely used catalyst, platinum, limits the commercial application of the fuel cell.

1.4 Motivation and research objectives

The motivation for this research stems from the growing promise and increased adoption of proton exchange membrane (PEM) fuel cells in both automotive and stationary applications. To further enhance their commercial viability, it is crucial to continuously improve the performance and reduce costs in the fuel cell technology. The primary objective of this thesis is to employ numerical investigations to optimize the flow channel configuration and the microstructure of the catalyst agglomerate. This optimization process aims to enhance the fuel cell performance and cost-effectiveness.

Flow-field plates, also known as bipolar plates, play a pivotal role in PEM fuel cells by facilitating the flow of reactant gases to the catalyst layers and managing excess water removal and electrical connections within the fuel cell stack. While the impact of flow channel cross-sectional shapes has been explored in the literature, the present research advances and aims to optimize the geometric configuration of these channels by introducing a novel "hybrid" flow channel design.

The catalyst layer serves a multitude of purposes, including providing sites for chemical reactions, facilitating the movement of reactants, enabling electron transfer through the solid phase, and transporting liquid water. It is of utmost importance to ensure that the catalyst layer meets the criteria of high efficiency, cost-effectiveness, and durability. Platinum, the preferred catalyst material, presents challenges due to its exorbitant cost and vulnerability to

poisoning, which have impeded the broader adoption of PEM fuel cells. To this end, one of the key aims is to numerically investigate the potential of platinum loading reduction.

Through the development of a multi-scale numerical model for PEMFCs, an investigation of the effects of the key catalyst factors, including platinum loading, particle size, active surface area, agglomerate internal structure, and agglomerate shape, on the fuel cell performance has been performed. The new and important research aims to bridge the gap between the theoretical understanding and practical applications, offering greater and important insights that could streamline experimentation and ultimately lead to the design of more efficient and cost-effective fuel cells.

Through the development of a multi-scale numerical model for PEMFCs, the effects of key catalyst factors, including platinum loading, particle size, active surface area, agglomerate internal structure, and agglomerate shape, on fuel cell performance were investigated. The present research aims to bridge the gaps between the theoretical understanding and practical applications, offering insights that could streamline experimentation and ultimately lead to the design of more efficient and cost-effective fuel cells.

1.5 Outline of thesis

This thesis comprises seven chapters. The initial chapter offers a brief introduction to the fundamental principles and primary types of fuel cells. It introduces the characteristics, advantages, disadvantages, and applications of each fuel cell type, with a particular emphasis on the PEMFC.

Chapter 2 Reviewed a various of metal and non-metal-based catalysts employed for ORR. Special attention is given to their performance, structure, and preparation processes.

Chapter 3 presents an innovative design featuring a variable cross-section area flow channel, presenting a numerical solution for merging square and trapezoidal designs into a unified configuration. This novel channel design holds the potential for improving mass and heat exchange in PEM fuel cells, thus enhancing the fuel cell performance.

Chapter 4 conducts a parametric study of the fuel cell catalyst layer. Within this chapter, the influence of the catalyst particle factors is scrutinised, including the platinum loading, particle radius, and active area, on the fuel cell performance. This chapter lays the groundwork for both Chapter 5 and Chapter 6.

Chapters 5 and 6 present a multiscale modelling framework that includes a catalyst agglomerate scale model and a fuel cell scale model, both specifically designed for polymer electrolyte fuel cells. In Chapter 5, the effect of the internal structure of the catalyst agglomerate on the fuel cell performance has been investigated, while in Chapter 6, the impact of the shape of the catalyst agglomerate has been explored.

In Chapter 7, the thesis findings are summarized, and the potential future directions for advancing towards more precise numerical models and the development of high-performance, cost-effective PEM catalysts are explored.

In the modeling chapters, Computational Fluid Dynamics (CFD) and multiscale modeling were the primary research methods employed. CFD facilitated a detailed analysis of fluid flow dynamics, while multiscale modeling provided a holistic perspective by integrating multiple scales of the system, enabling a more comprehensive understanding of the agglomerate structure.

Chapter 2 Review of the Theoretical and Modelling Studies of Catalysts

2.1 Introduction

In PEM fuel cells, electrochemical reactions occur in both the anode and cathode catalyst layer (CL). In the reaction of the anode, hydrogen gas is separated into protons and electrons under the action of the catalyst, and the protons flow through the electrolyte to the cathode and the electrons reach the cathode through an external circuit. At the cathode, under the action of a catalyst, hydrogen protons and oxygen ions combine to form water. For fuel cells to have higher efficiency and better application prospects, these reactions need to be further investigated. Therefore, the catalyst layer must have high activity and adequate microstructure. The microstructure of the catalyst layer is mainly composed of four different elements: carbon particles, Pt particles, ionomer network, and pores, these particles form agglomerates. These phases are used throughout the fuel cell. For example, pores and ionomer membranes can provide channels for diffusion of reactive gases; ionomers and pores provide a pathway for water diffusion and absorption; ionomer membranes and catalyst particles provides a path for protons and electrons; at the same time, these microstructures can help transfer heat from the reaction point to the channels and flow field plates [27]. All these processes can affect the performance and durability of the PEM fuel cell, so some key factors must be considered during the research, such as the shape of the catalyst, the thickness of the ionomer film, the platinum loading, the particle size of the platinum and carbon, the ionomer volume fraction, the CL porosity, etc. [28]. Figure 2.1 illustrates the electrochemical processes happening within the CCL. Specifically, the

electrochemical reaction takes place at the triple phase boundary (TPB) where the proximity between protons and oxygen is crucial for the reaction to occur.

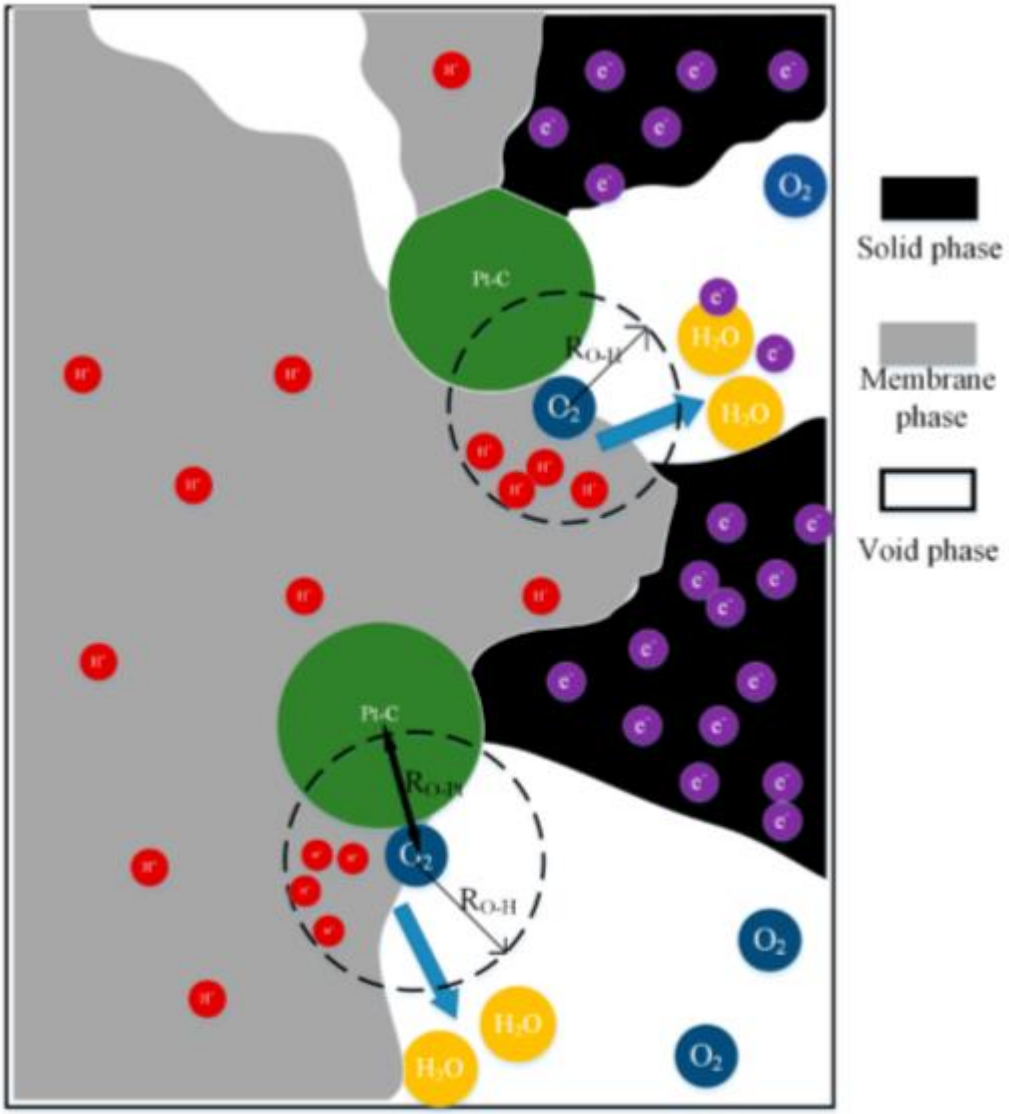

Figure 2.1 Schematic of the catalyst microstructure of the PEM fuel cell [29]**.**

Oxygen reduction reactions can occur in both acidic and alkaline media. For PEM fuel cells, the ORR in the cathode is very important and can influence the overall performance. As shown in Figure 2.2A, by pumping hydrogen into the channel on the anode side, hydrogen is broken down into electrons and protons. Then the electrons flow out of the anode to provide electrical energy and eventually reach the cathode to reduce the oxygen, and the

protons diffuse through the membrane to the cathode and combine with the reduced oxygen ions to form water [30].

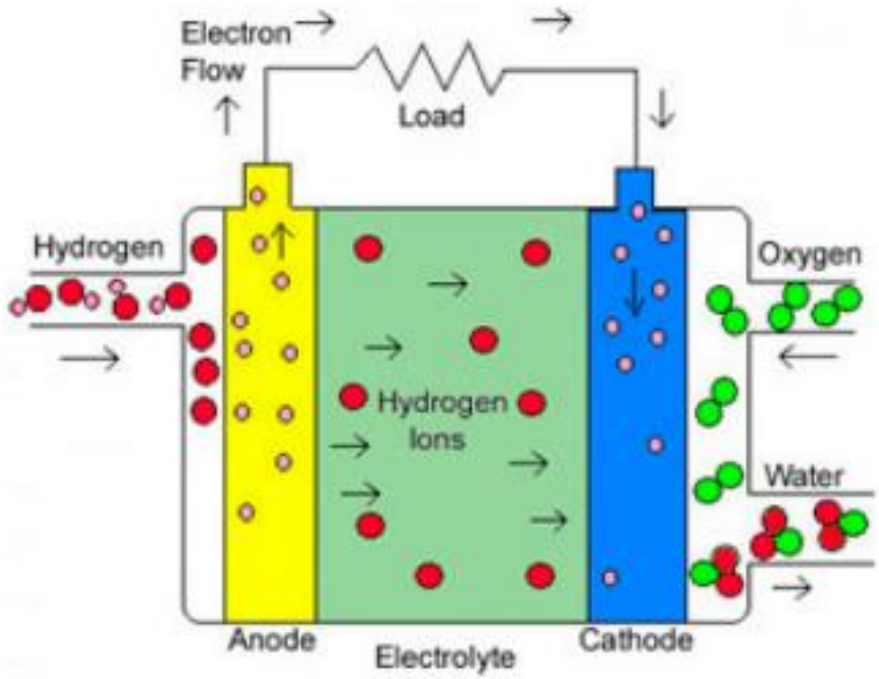

(A)

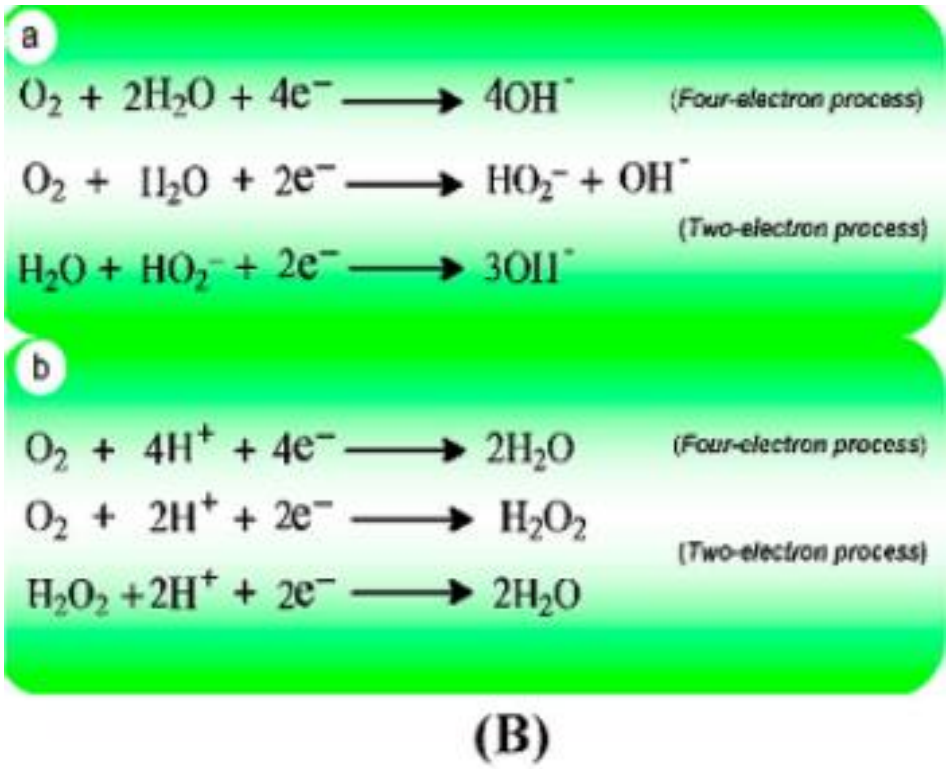

Figure 2.2 (A) Schematics of a fuel cell. (B) ORR in (a) alkaline and (b) acidic medium [31]**.**

It is well known that ORR can form H_2O_2 in an acidic medium in a two-step two-electron path or use HO_2^- as an intermediate product in an alkaline medium or use a four-electron path to reduce oxygen to water or generate OH- in an alkaline medium and then combines with protons to form water (Figure 2.2B). For the most widely used fuel cell technology, it usually uses Pt as the ORR catalyst at the cathode of the fuel cell. Using the Pt particles as catalysts can provide the active site for two-electron or four-electron pathways to effectively adsorb and reduce molecular O_2. In addition to facing high costs, Pt electrodes have suffered other challenges and problems, including drift during long-term use, fuel cross-over effects, and CO poisoning [25]. Therefore, it is necessary to find an alternative material: with a lower cost but more reliable new materials as catalysts for the oxygen reduction reaction in the cathode side of the PEM fuel cell.

Oxygen reduction reactions are usually accompanied by the formation and destruction of O-O bonds and O-H bonds. Adzic and colleagues have discovered that the use of suitable metal materials as platinum support materials (such as Au, Fe, ..., and other transition metals) can even exceed the pure platinum electrocatalytic activity, thereby greatly reducing the load of platinum and the overall cost of the fuel cell [32]. Also, there are a series of non-metallic catalysts that are constantly being developed to replace platinum-based catalysts.

2.2 Theoretical studies of catalysts

2.2.1 Metal based catalysts for ORR

Platinum catalyst. Currently, Pt is the commercialized catalyst used in PEM fuel cells. Its performance is mainly determined by the shape, size, crystallization, morphology, and loading of the Pt catalyst [33]. The catalytic effect of Pt (100) is better than that of Pt (111) because the adsorption rate of the sulfates is different due to the difference in morphology. Hence, controlling the shape and morphology of catalyst particles is one of the keys to controlling the catalytic performance of the ORR [34]. Wang and his colleagues found that the specific activity of the synthesized monodisperse Pt nanoparticles was more than twice higher than the commercially available Pt catalyst. When the Pt nanocube measures 7nm in size, its current density is approximately four times higher than that of the other two shapes, namely the 3nm and 5nm polyhedra. Also, it has been found, from previous studies, that optimizing the Pt shape has a significant effect on improving the ORR [35]. During the oxygen reduction reaction (ORR), the platinum catalyst surface often gets covered by the electrolyte or a hydroxy layer, leading to a reduction in active sites and thereby limiting the catalyst's efficiency. Enhancing ORR activity involves alloying platinum catalysts with different transition metals or shaping them deliberately to weaken the binding strength between platinum atoms and the adsorbed species.

Platinum alloy catalyst. To reduce the cost of PEM fuel cells, the researchers have reduced the Pt usage by alloying Pt with precious metals or transition metals [36]. Stamenkovic and his colleagues found that the ORR activity of the Pt_3Ni (111) surface was 10 times that of Pt (111) and 90 times that of the current commercialized Pt / C catalysts. The Pt_3Ni (111) surface has a special electronic structure (d-band centre position) and the arrangement of surface atoms[37]. By studying the oxygen reduction kinetics on the surfaces of Pt_3Ni and

Pt_3Co, Stamenkovic and his colleagues found that the activity of the catalyst depends on the anion properties of the supporting electrolyte [38]. Adsorption of impurity anions onto Pt nanoparticles significantly impacts the kinetics of the Oxygen Reduction Reaction (ORR). This occurs as these anions occupy crucial surface sites on the catalyst, impeding the molecular oxygen's dissociative adsorption. Additionally, these impurity anions have been observed to accelerate Pt dissolution, leading to a quicker loss of ORR activity for Pt. This isn't the primary focus of our research, so no further discuss into this matter in the upcoming chapters.

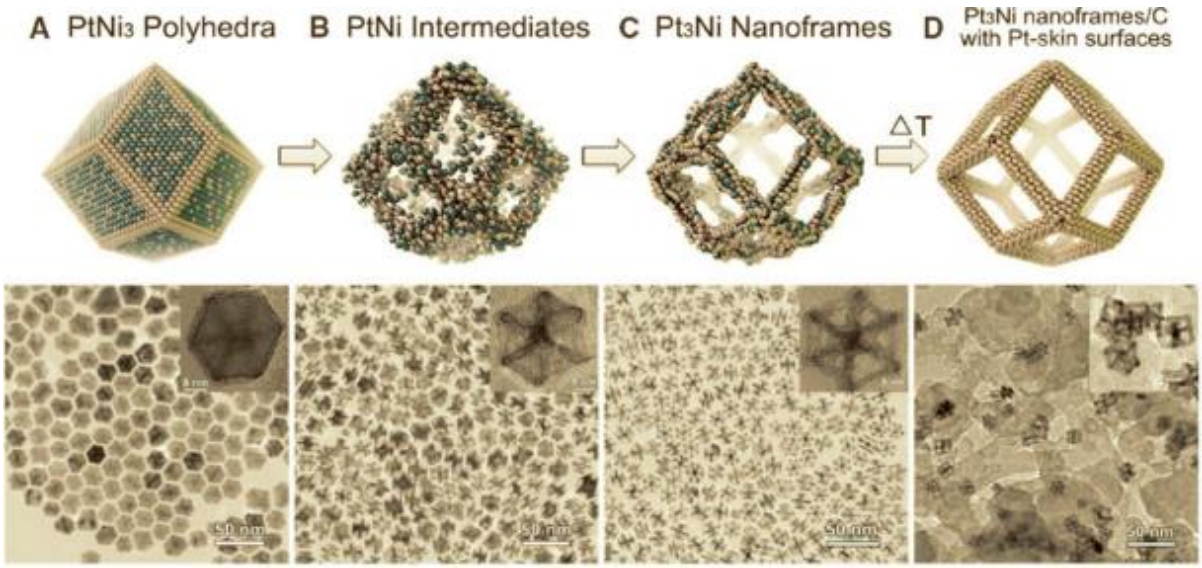

Figure 2.3 Schematics of Pt alloy nanostructure (A)$PtNi_3$, (B) PtNi , (C) Pt_3Ni, and (D) Pt_3Ni nanoframes with Pt(111)-skin−like surface[39]**.**

Recently, Chen and his colleagues used alloy nanoparticles of platinum and nickel to react with oxygen to dissolve the nickel inside the alloy particles, thereby generating a Pt_3Ni nanoframe. This 3D 12-face hollow structure nanoframe removes the nickel-rich central structure and retains the edges of Pt-rich $PtNi_3$ polyhedrons (Figure 2.3). This structure can produce more oxygen and Pt atoms contact so that this Pt_3Ni nanoframe catalyst has higher catalytic activity and stability than Pt / C [39]. The boost in catalyzing the oxygen reduction

reaction (ORR) on Pt3Ni and Pt_3Co compared to Pt was linked to the prevention of $Pt{-}OH_{ad}$ formation on Pt sites encircled by Ni and Co atoms covered with an "oxide" layer beyond 0.8 V. Chen's team suggested that the catalytic enhancement observed in the "Pt-skin" results from electronically altered Pt atoms situated atop the Co-enriched layer beneath.

2.2.2 Metal catalyst supported by carbon materials

Because carbon nanomaterials such as CNT, graphene, and graphite, when compared with carbon black have a larger surface area, better electrical conductivity, and thermal conductivity, makes them become ideal support materials for metal catalysts. At the same time, the carbon support can improve the stability and activity of the metal catalyst. For example, Kongkanand and colleagues found that the activity and stability of the catalyst is enhance when then mixing Pt nanoparticles with SWCNT [40]. It was also observed that the carbon nanotube-supported PtAu alloy has a higher methanol tolerance than pure platinum [41]. Lately, graphene has been employed as a support material for metal catalysts to enhance their Oxygen Reduction Reaction (ORR) performance. For example, Guo and his colleagues enhanced the overall catalytic performance of the ORR by using graphene as a supporter to load / CoO and FePt nanoparticles [42].

By combining heteroatom substitutes (such as nitrogen) with carbon nanomaterials, then this can cause electron conversion to obtain the required electronic structure however, this may become a promising catalyst support [43]. A catalyst featuring Cobalt Oxide (CoO) supported by nitrogen-doped Carbon Nanotubes (NCNT) exhibited a four-electron Oxygen Reduction Reaction (ORR) pathway, achieving a high current density and thereby outperforming a mixture of Co_3O_4 and graphene, as well as conventional Pt/C catalysts, at moderate overpotentials [36]. Wu and his research team discovered that Fe_3O_4 nanoparticles doped with three-dimensional nitrogen-doped graphene can serve as exceptionally efficient

catalysts for the Oxygen Reduction Reaction (ORR). This catalyst offers several benefits, including a high current density, minimal production of hydrogen peroxide (H2O2), a high electron transfer number, and exceptional durability [44]. Although there have been many studies on the use of graphene to improve its catalytic performance, the poor intermediate resistance of graphene is still a problem to be solved. Therefore, to commercialize the fuel cell technology, it is still necessary to develop new ORR catalysts with lower cost and can achieve higher performance and more stable than the commercialized Pt / C catalysts.

2.2.3 Metal-nitrogen- carbon (MNC) catalysts

Recent studies have shown that the simultaneous heating of transition metals at 800-1000 ° C and then introducing nitrogen and carbon may also produce promising ORR MNC catalysts, and the metals usually are Fe and / or Co, see Figure 2.4. Wu and his colleagues discovered a non-noble metal catalyst was prepared by synthesizing Fe and Co in the environment of high temperature and polyaniline (PANI). (NPMCs) [45]. The study found that PANI-Fe-C can be used as an oxygen reduction reaction (ORR) catalyst in acidic media, and its catalytic performance is almost the same as that of the Pt/C catalyst at a potential of 60mV. The ORR performance of the PANI-FeCo-C catalyst is greatly improved and is very durable. In a hydrogen fuel cell, a durability of nearly 700 hours can be obtain under a 0.4 voltage working condition [46]. Transition metals are essential for the formation of highly graphitized carbon. When ethylenediamine and Co are synthesized at high temperature, CNTs and onion-like carbon nanostructures will appear in the product, while cyanamide and Fe precursors are used to synthesize bamboo-like tubular carbon nanostructures. [47].

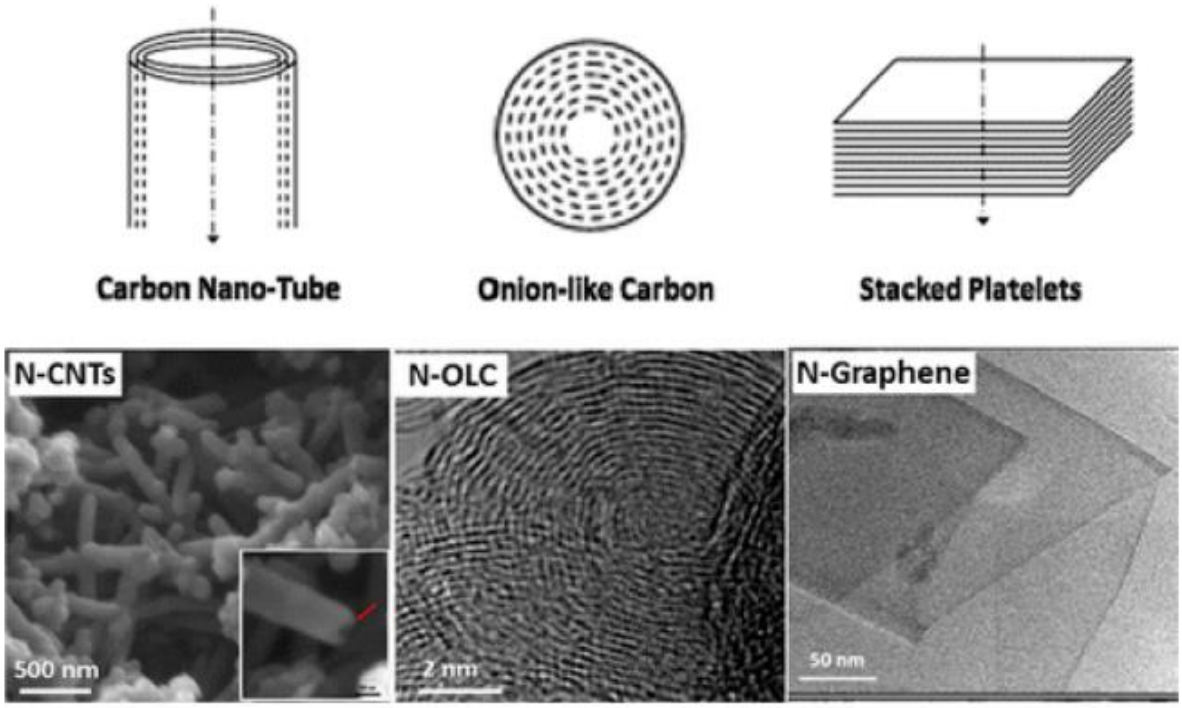

Figure 2.4 Schematics of carbon nanomaterials in MNC catalysts. CNTs (left), onion-like carbon structure (middle), and graphene (right)[48]**.**

Wu and colleagues further demonstrated that the MNC catalyst is rich in the carbon nanostructures, the geometry of the nanomaterial includes tubes, onion-liked structure, plate-liked structure, see Figure 2.4, which formed in the catalyst synthesis process[48]. Throughout the synthesis process, while the introduction of nitrogen species may play a crucial role in enhancing the performance of the active sites in the M-N-C catalyst. The precise mechanism behind the formation of these active sites, their bonding properties, and their interactions with the carbon nanostructure remain unclear. The possible explanation for this is that tube-like, onion-like, and platelet-like carbon materials, when combined with Pt nanoparticles as support, can enlarge the active area of the catalyst agglomerate.In the meanwhile it also provide more active sites for ORR.

2.2.3 Non-metal ORR catalysts

Carbon nanomaterials are widely used. It has extremely high stability, shape, and structural characteristics and this makes it an ideal choice for catalyst supports and even non-metallic catalysts. Common carbon nanomaterials are fullerenes, carbon nanotubes, graphene sheets, and graphite nanosheets. These different carbon nanomaterials provide a new way for catalyst improvement. The introduction of heteroatoms in these carbon nanomaterials may further lead to electronic modulation, thus providing an ideal electronic structure for the catalytic process [49]. In recent years, researchers have been still committed to developing metal-free carbon nanomaterials for various oxidation/reduction catalysis. In this thesis, the focus will be only on carbon nanotubes and graphene for ORR.

Carbon nanotubes. Gong and his colleagues discovered that vertically aligned nitrogen-containing carbon nanotubes (VA-NCNT, Figure 2.5) can be used as highly efficient metal-free ORR catalysts. This metal-free VA-NCNT catalyst can realize a four-electron ORR process. In an alkaline media, compared with commercial Pt catalysts, VA-NCNT is not CO poisoned and has better catalytic performance and it is more robust. Simultaneously, VA-NCNT boasts the benefits of a substantial surface area, strong electrical and mechanical characteristics, and remarkable thermal stability, making it suitable for use in high-temperature environments [50]. Now, researchers have used various methods to prepare new non-metal ORR catalysts by doping heteroatoms with carbon nanomaterials.

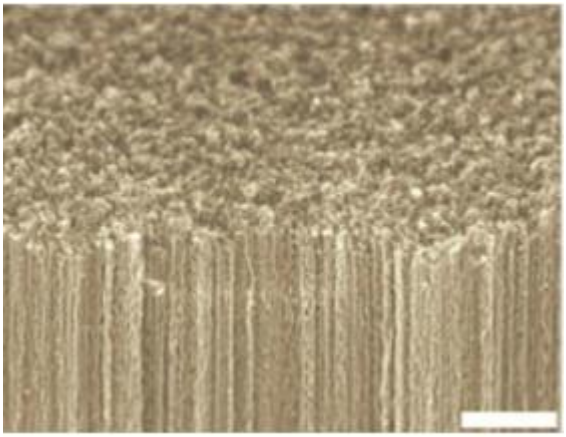

Figure 2.5 Schematics of an SEM image of VA-NCNTs. The scale bar of this figure is 2μm.

Graphene. Graphene represents a promising substitute for metal-free Oxygen Reduction Reaction (ORR) catalysts. Research has indicated that Nitrogen-doped graphene, synthesized via Chemical Vapor Deposition (CVD) in ammonia, exhibits outstanding ORR performance, comparable to that of VA-NCNT containing an equivalent nitrogen content, especially in alkaline environments [51]. Despite variations in CVD types, the fundamental process remains similar, encompassing common elementary steps. Initially, the reactant gases enter the reactor. These gases undergo gas-phase reactions, forming intermediate reactants and gaseous by-products through homogeneous reactions, or they diffuse directly through the boundary layer to the substrate. In both scenarios, the reactant gases and intermediates adsorb onto the heated substrate surface, diffusing across it. Subsequent heterogeneous reactions at the gas-solid interface facilitate the continuous formation of thin films through nucleation, growth, coalescence, and the generation of reaction by-products. Eventually, any gaseous products and unreacted species desorb from the surface, exiting the reaction zone. Although recent research shows that graphene films prepared by the CVD method can reach 30 inches, CVD usually requires the consideration of the scalability and cost. At present, there are two main methods for producing N-doped graphene as an ORR

catalyst, one is by the CVD method, and the other is by heat-treating graphene material with ammonia. Of course, there are other methods besides these two methods. [52]. As in the evolution from NCNT to B-doped CNT, Sheng and his colleagues thermally annealing GO react with boron oxide, boron- graphene was prepared. This boron-doped graphene catalyst is similar to the Pt catalyst and presents good ORR activity in the alkaline electrolyte [53]. In addition to NCNT and BCNT, Wang and others found a simple method for producing BCN and they introduced boric acid and ammonia during the GO annealing. Thus metal-free boron-doped graphene with adjustable B / N doping levels can be obtained, and graphene mixed with B and N can be used as an effective ORR electrocatalyst. BCN graphene proved to have superior ORR catalytic activity than commercial Pt / C [54]. Doping carbon with nitrogen and boron, such as $B_7C_{87}N_6H_{26}$ and $B_{12}C_{77}N_{11}H_{26}$, leads to more carbon atoms with notably higher spin and charge density compared to pure graphene. This augmentation provides additional active sites crucial for catalyzing the Oxygen Reduction Reaction (ORR). Explained through band theory, the G band stems from the bond stretching of all sp^2 bonded pairs, encompassing C-C, B-C, N-C, and B-N bonds, while the D band corresponds to the sp^3 defect sites. Despite minor shifts in the positions of the D and G bands, BCN graphene demonstrates a distinct ID/IG value compared to graphene oxide and N-doped graphene. The ID/IG intensity ratio increases from graphene oxide to N-doped graphene due to the introduction of defects through nitrogen doping. Co-doping with boron and nitrogen further amplifies this intensity ratio of ID/IG.

3D carbon nanomaterials. By doping heteroatoms with carbon nanomaterials can cause charge redistribution, thus showing that these non-metal carbides are potential catalyst replacements. The conductivity is an important character of the electrode and can influence the electrocatalysis performance. Therefore, for practical applications, a larger contact area,

and a better partial diffusion and charge transfer path with the help of a 3D structure are required [55].

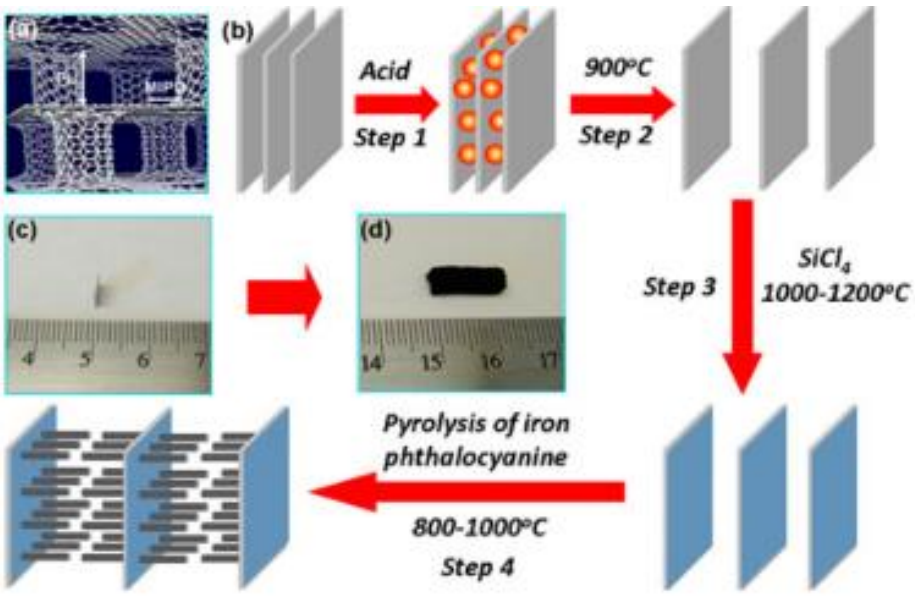

Figure 2.6 A schematic of representation of a 3D VACNT- graphene nanostructure, and the procedure of the preparation. [56]**.**

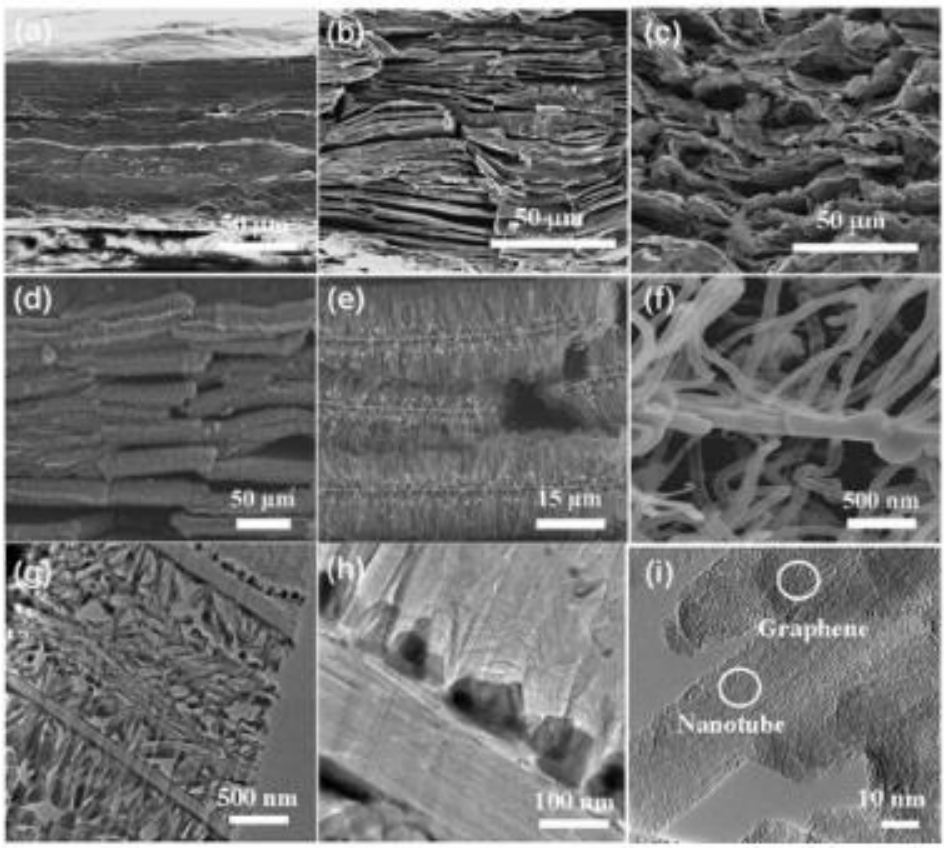

Figure 2.7 SEM images of different structured VACNT-Graphene[55]**. Figure No intext.**

Recent studies have found that the graphene layer supported by VA-CNT not only has better through plane mass transport property but also retain the exceptional catalytic performance of both compensates [57]. Furthermore, when doping this 3D nanostructured material with lithium ions, it demonstrates excellent potential as a medium for hydrogen storage purposes. The simulation results indicate that these VA-CNT-graphene structures with large surface area, see Figure 2.6, have excellent mechanical and electrical properties and have the potential to be applied to ORR catalysts [55]. Figure 2.7 shows the microstructure of VACNT with different treatment. a-e is the SEM image, which shows the structure changing after acid treatment. f-i is the TEM image, which shows the VACNT architecture under different magnifications.

2.2.4 Carbon nanomaterials doped with heteroatoms

As can be seen from the above discussion in Section 2.2.3, the latest research on non-metal ORR catalysts mainly focused on alkaline electrolytes. However, acid electrolytes fuel cells, especially polymer electrolyte fuel cells, have greater market prospects. Some of the non-metal carbon nanomaterials and heteroatom-doped non-metal carbon nanomaterials shown earlier have good ORR catalysis both in alkaline and acidic electrolytes. For example, Kundu and his team reported that compared to undoped NCNT, prepared by pyrolysis of acetonitrile demonstrate increased and sustained Oxygen Reduction Reaction (ORR) activity in a 0.5 M H_2SO_4 environment. Wang and his colleagues found that NH_3 treated nitrogen-doped OMCS have potential to be a promising candidate for metal-free catalysts. Compared with Pt-based catalyst, it has higher ORR activity and better stability in acidic solution.

Compared with other non-metal catalysts, CNTs-graphene complexes have higher ORR activity, more robustness and are more stable in an acidic media. Among them, graphene controls the catalytic activity, and the inner wall of the three-dimensional structure maintains its electrical conductivity to ensure the transfer of charges generated during the catalytic process.

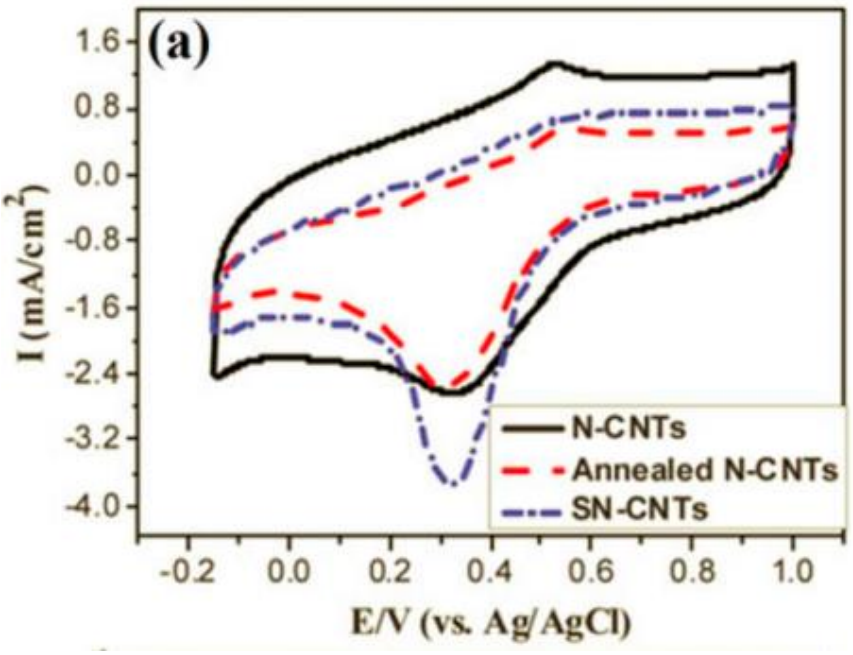

Figure 2.8 Comparison of Cyclic Voltammograms (CVs) for ORR using N-CNTs and Annealed N-CNTs Catalysts in 1 M $HClO_4$ Aqueous Solution [58]**.**

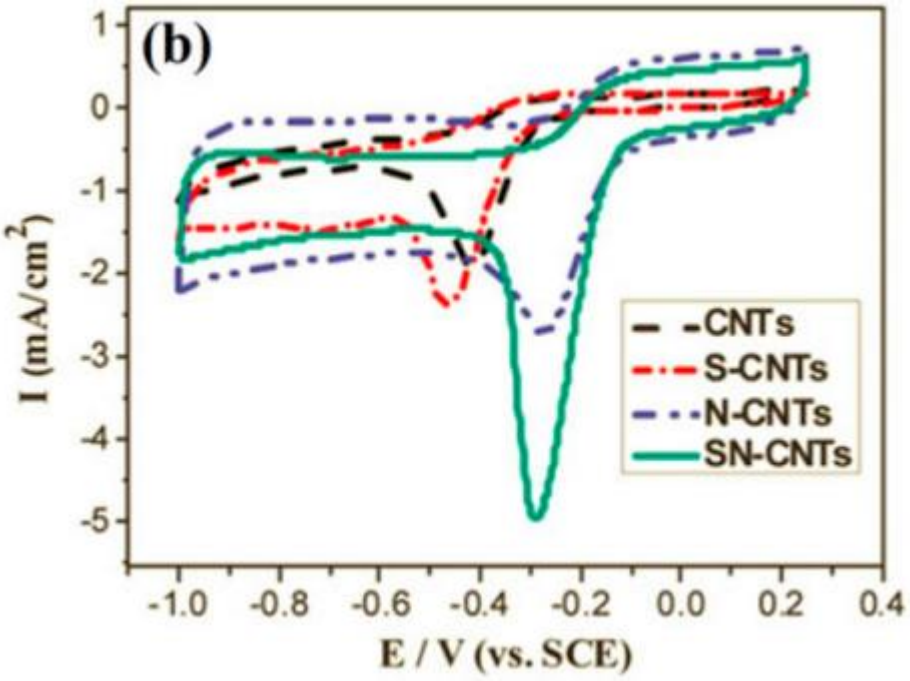

Figure 2.9 Comparison of Catalysts in 0.1 M KOH Aqueous Solution and LSV Profiles of SN-CNTs in Oxygen-Saturated 1 M $HClO_4$ Solution[58]**.**

Recently, Shi and his team prepared a new non-metal catalyst by doping sulfur and nitrogen to CNT (SN-CNT). When compared with N-CNT it exhibits superior Oxygen Reduction Reaction (ORR) performance in both acidic and alkaline environments [58]. Figure 2.8 illustrates a comparative analysis of cyclic voltammograms (CVs) between N-CNT and SN-CNT in both acidic and alkaline environments. As shown in figure 2.9, when subjected to oxygen-saturated solutions in acidic and alkaline conditions, SN-CNT displays oxygen reduction peaks at approximately +0.29 V and -0.3 V, respectively. This observation, in contrast to the highest peak current among CNT, N-CNT, and S-CNT, suggests that the co-doping of sulfur and nitrogen significantly enhances the activity of the Oxygen Reduction Reaction (ORR). In the meanwhile, compared with Pt / C, SN-CNT, it has also good durability. After 10,000 cycles, the current retention rate is still close to 90% but after 10,000 cycles, the current retention rate of Pt/C decreased by 40% compared to SN-CNT. In addition, the co-doping of S and N enhances the ORR activity of SN-CNT. Enhancements in the nitrogen state within N-CNT, along with the creation of asymmetric spin and charge density, lead to an improved Oxygen Reduction Reaction (ORR) performance in SN-CNT. These SN-CNTs, applicable in acidic environments, have demonstrated the potential to serve as a viable substitute for Pt/C catalysts in Proton Exchange Membrane Fuel Cells (PEMFCs). This also opens up a promising avenue for the exploration of novel non-metallic catalysts suitable for use in acidic conditions.

In addition to the SN-CNTs described above, many other non-metallic catalysts can be applied to acidic electrolytes, such as N-doped SWNTs (Yu et al., 2010), the vapour phase polymerized PEDOT (Winther et al., 2008) and [60], N-doped graphene, and 3D-structured graphene-CNT. Although these non-metallic catalysts all have ORR catalytic activity in acidic media, the catalytic performance still cannot meet the current commercial needs and thus requires to be further improved.

Chapter 3 Novel design of a variable cross-sectional area flow channel

3.1 Abstract

This chapter aims to investigate the impact of three different flow channel cross-sections on the performance of the fuel cell. A comprehensive three-dimensional polymer electrolyte membrane fuel cell model has been developed and a set of conservation equations have been solved. The flow is assumed to be steady, fully developed, laminar and isothermal. The investigated cross-sections are the commonly used square cross-section, the increasingly used trapezoidal cross-section and a novel hybrid configuration where the cross-section is square at the inlet and trapezoidal at the outlet. The results show that a slight gain is obtained when using the hybrid configuration and this is due to increased velocity which improves the supply of the reactant gases to the catalyst layers and removes heat and excess water more effectively compared to other configurations. Further, the reduction of the outlet height of the hybrid configuration leads to even better fuel cell performance and this is again due to increased velocity in the flow channel. The data generated in this study will be highly valuable to engineers interested in studying the effect of fluid cross-sectional shape on fuel cell performance. This study proposes a novel flow field with variable cross-section. This design can supply a higher amount of reactant gases to the catalyst layers, dissipates heat and remove excess water more effectively.

3.2 Introduction

Hydrogen conversion technologies including hydrogen electrolysers [61], [62] and hydrogen fuel cells[63], [64] will play a pivotal role in decarbonising industrial, heating and

automotive sectors in the near future. Notably, polymer electrolyte membrane (PEM) fuel cells have been increasingly used in a multitude of portable, automotive and stationary applications and this is due their high efficiency and low-temperature operation [2]. However, PEM fuel cell technology needs to be even more efficient to compete with the conventional power conversion technologies [65]. Among them, the uniformity of reactants in the flow field of the PEM fuel cell is a key issue that needs to be considered, because it can affect the uniformity of the current density distribution, heat distribution, and water distribution and transfer [66]. Flow-field plates (also know as bipolar plates) are one of the key components for PEM fuel cells. They are, through hosting the grooves or the flow channels, mainly responsible for supplying reacting gases to the catalyst layers (where the half-reactions take place) through the gas diffusion layers (GDLs). They also assist in: (i) removing excess water from the heart of the fuel cell, which is the membrane electrode assembly (MEA), and (ii) electrically connecting between the anodes and the cathodes of the cells in a fuel cell stack. The impact of the shape of the cross-section of the flow channel has been extensively investigated in the literature.

Carcadea et al. [67] investigated the effect of the depth of the flow channel on the performance of the fuel cell. They found that the maximum current density increased by around 7% with the smallest depth and this is due to better removal of excess water and better membrane humidification. Ahmadi et al. [68] developed a three-dimensional PEM fuel cell model with conventional flow channels and found that the humidity of the inlet gases and membrane hydration are the most important parameters that affect the fuel cell performance and mass transfer within it. Samanipour et al. [69] numerically developed cylindrical designs for PEM fuel cells and showed that they outperform the conventional design with square flow channels. Ashrafi et al. [70] reported that the fuel cell with serpentine flow channels demonstrate a better performance and less liquid water

accumulation than that with parallel flow channels. Yan et al. [71] showed that the best fuel cell performance is obtained with a height taper ratio of 0.5 and a width taper ratio of 1.8 and this is due to the improved fuel utilisation efficiency and water removal. Fontana et al. [72] investigated the impact of the inclination of the flow channel and they found that the peak power density increases by 8% with an inclination of 0.75°. Kumar and Reddy [73] developed a numerical model to study the influence of different cross-sectional shapes of the flow field on the performance of PEM fuel cell. They showed that the triangular and semi-circular cross-sections can increase the hydrogen consumption rate by up to 9%. Zeng et al. [74] optimised the cross-sectional shape of fuel cell channels by using a genetic algorithm. In this study, the width of the bottom and the top edges of the channel were the variables, and the output power of the fuel cell was the objective function. The fuel cell had the best performance when the width of the bottom and the top edges of the trapezoidal channel were around 1.3 mm and 0.9 mm, respectively. Namely, at 0.5 V, the output power of the optimised design was found to be around 8 % higher than that of the conventional square flow channel. This is due to the fact that the optimised design provides a larger contact area between the flow channel and the gas diffusion layer, resulting in higher and more uniform supply of reactant gases to the catalyst layer [74].

Liu et al. [75] used a genetic algorithm to optimise the channel structure of the PEM fuel cell. The variables in the study were the heights of the inlet and the outlet of the channel. The output power was the objective function and used to evaluate the fuel cell performance. The best performance was obtained for the conical channel with inlet height of ~ 0.39 mm and outlet height of 0.20 mm. This is because this conical structure, relative to other configurations, provides a higher pressure increase along the channel, thus reducing the mass transfer resistance.

Ahmed et al. [76] numerically studied three different channel cross-sections: rectangular, trapezoidal, and parallelogram on the PEM fuel cell performance. Their results showed that the distribution of the reactant gas becomes more uniform at the interface between the cathode GDL and the membrane as the width of the rib decreases, thereby assisting in reducing the mass concentration losses. The results also showed that, compared to other investigated cross-sections, the rectangular cross-section channel provides a higher cell voltage, while the trapezoidal cross-section achieves a more uniform current density distribution at the interface between the cathode GDL and the membrane. Owejan et al. [77] experimentally investigated the influence of rectangular and triangular cross-sections on the PEM fuel cell performance. The study showed that there is less water accumulated in rectangular channels than in triangular channels of the same cross-sectional area as more water is retained at the corners of the triangular channels adjacent to the GDL. Wang et al. [71] numerically studied the influence of the flow channel area ratio, which is the ratio between the cathode flow channel area to the total reaction area, on the fuel cell performance. Their study shows that, for both parallel and interdigitated flow configurations, the larger is the flow channel area ratio, the better is the fuel cell performance and this is mainly due to the increase in the contact area between the reactant gas and the GDL. However, the impact of this parameter (i.e. the flow channel area ratio) is less with the interdigitated flow configuration and this is because the baffle configuration already forces the reactant gas to enter the GDL and subsequently the catalyst layers. Higier and Liu [78] locally measured the current under the rib and channel in a variety of single pass serpentine flow fields of a PEM fuel cell. Their findings revealed that a 1mm channel width enhanced the bipolar plate's contact, lowered resistance, and minimized concentration losses, resulting in a higher current density. While they didn’t specify the narrowest width, it's important to note that excessively narrow channels might impede effective removal of excess water from the fuel cell.

Metallic flow-field plates have been increasingly used and this is due to ease of manufacture and their superior mechanical strength compared to the conventionally-used graphitic flow-field plates [79]. These metallic plates are normally produced through stamping or hydroforming processes which result in trapezoidal flow channels [80]. Ismail et al.[81] numerically investigated the impact of some geometrical parameters, including the sidewall angle on the key flow characteristics, including the Poiseuille number and the incremental pressure drop. They found that the impact of the rounded corners could not be overlooked for very low channels heights or very high sidewall angles.

Although the influence of the gas channel configurations on the performance of the PEM fuel cells has been thoroughly investigated in the literature [82], [83], [84], in this work some new and important improvements and optimizations of the flow channel geometry have been made. Namely, a novel and comprehensive three-dimensional multiphase numerical model that combines the conventional square gas flow channel and trapezoidal flow channel has been developed. The proposed new "hybrid" configuration flow channel has a decreasing cross-section along the gas flow direction. Unlike the similar flow channel configurations proposed in the literature, the "hybrid" flow channel retains the contact area between the flow channel and the GDL. This not only increases the gas velocity but also enables better reactant exchange and liquid water removal.

3.3 Model description

The computational domain of the base case or Case 1 (where the cross-section of the channel is square) of the modelled fuel cell is shown in Figure 3.1. As shown in the Figure, only a portion of the fuel cell which incorporates a single straight channel for each side of the fuel cell (the cathode and the anode) has been modelled in order to save the computation time.

The dimensions of the computational domain are 50 mm × 2 mm × 3.47 mm. The main assumptions considered in the study are that:

i. The operation of the fuel cell is steady state.
ii. The flow in the channels is laminar since the Reynolds number is small.
iii. The gaseous mixtures are considered as an ideal gas.
iv. The GDL, the CL layer and the membrane electrolyte are all isotropic.
v. The membrane is impermeable to gases.
vi. The interfacial contact resistances are between the various fuel cell components are negligible.

The other two computation cases investigated in this study are the modelled fuel cell with (a) trapezoidal channels (Figure 3.2a) which have the same cross-sectional areas as the square channels (the width of the smaller base is 0.5 mm and the height of the channel is 1mm) and (b) hybrid channels where the cross section at the inlets of the channels is square and trapezoidal at the outlets (Figure 3.2b). The cross-sectional area in the latter design continually decreases from the inlet to the outlet. It should be noted that the same flow channel flow configurations were maintained for both the cathode and the anode sides of the fuel cell. Table 3.1 displays the physical and geometrical characteristics.

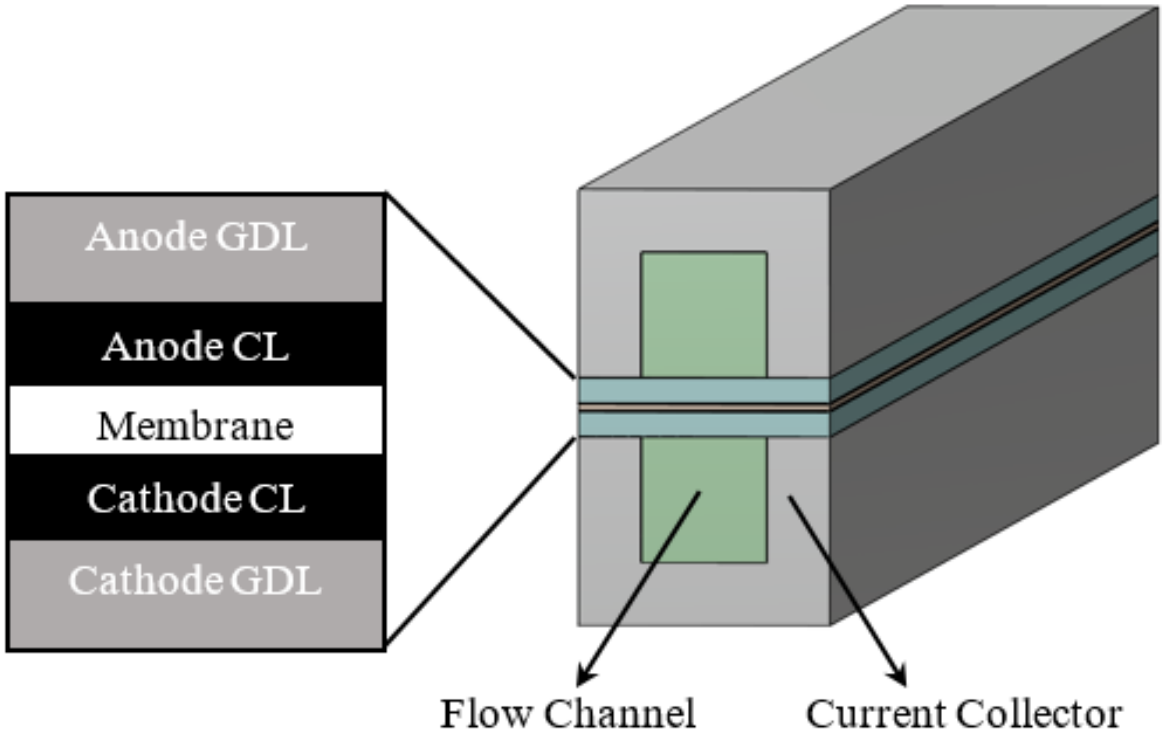

Figure 3.1 A schematic diagram of the base case of the PEM fuel cell model.

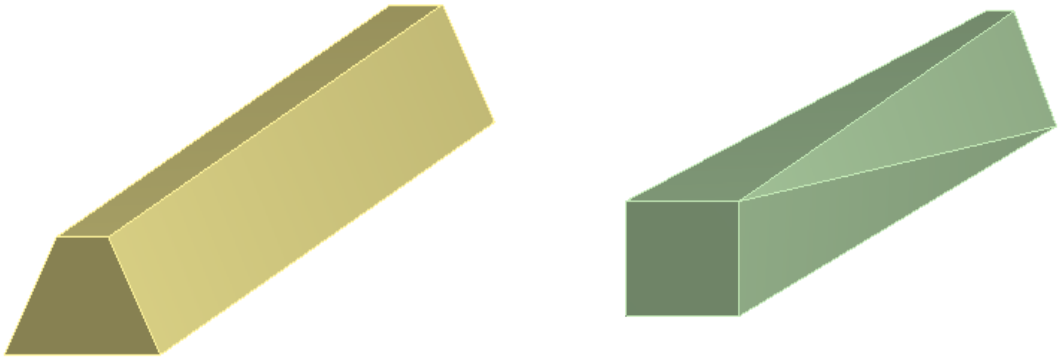

(a) (b)

Figure 3.2 Schematics for the modelled flow channels with (a) trapezoidal (Case 2), and (b) "hybrid" (Case 3) cross-sections.

3. 3.1 Governing equations

The following conservation equations were used in the model. The conservation of mass, or the continuity equation, is given by [85], [86]:

$$\nabla \cdot (\varepsilon \rho \vec{u}) = S_m \tag{3.1}$$

where ρ is the density of the fluid, $\vec{u}$ is the velocity vector, ε is the porosity and S_m is the mass source term which is the sum of the source term of the chemical species in either the cathode or the anode (see Equation. (3.3) and Table 3.2). The conservation of momentum equation is given as follows [85]:

$$\nabla(\varepsilon \rho \vec{u}\vec{u}) = -\varepsilon \nabla \mathrm{p} + \nabla(\mu \nabla \varepsilon \vec{u}) + S_u \tag{3.2}$$

where p is the fluid pressure, μ is the dynamic viscosity, and S_u is the momentum source term. The conservation of species could be expressed as follows [87]:

$$\nabla\left(\varepsilon \rho \vec{u} Y_{ij}\right) = \nabla\left(\rho D_{ij}^{eff} \nabla Y_i\right) + S_i \tag{3.3}$$

Where Y_i is the mass fraction of the species *i*, D_i^{eff} is the effective mass diffusion coefficient of the species *i* into *j*, and S_i is the source term of the species *i* (O_2, H_2 or H_2O) which is given in Table 3.3.

The energy transport equation could be expressed as follows [87]:

$$\nabla \cdot \left(\rho c_p \vec{u} T\right) = \nabla(k \nabla T) + S_T \tag{3.4}$$

Where ρ is the density of the fluid is, $\vec{u}$ is the velocity vector, *k* is thermal conductivity, S_T is the thermal source term which is listed in Table 3.3. Conservation of charge equations are obtained as follows [87]:

$$\nabla(\sigma_c \nabla \emptyset_c) = S_c \tag{3.5}$$

$$\nabla(\sigma_{mem} \nabla \emptyset_{mem}) = S_{mem} \tag{3.6}$$

$$\sigma_m = (0.514\lambda - 0.326) \cdot \exp\left(1268 \cdot \left(\frac{1}{303} - \frac{1}{T}\right)\right) \tag{3.7}$$

Where σ_c and σ_m are respectively the electrical and the ionic conductivities, $\emptyset_c$ and $\emptyset_m$ are respectively the electrical and protonic potentials, λ is the dissolved water content. S_c and S_m are the charge source terms and are equal to the volumetric current density obtained by the Butler-Volmer equation [17]:

$$J_a = i_a^{ref} \zeta_{eff} \left(\frac{P_{H_2}}{C_{H_2}^{ref} H_{H_2}}\right)^{0.5} \left(exp\left(\frac{\alpha_a F}{RT}\eta_a\right) - exp\left(\frac{-\alpha_c F}{RT}\eta_a\right)\right) \tag{3.8}$$

$$J_c = i_c^{ref} \zeta_{eff} \left(\frac{P_{O_2}}{C_{O_2}^{ref} H_{O_2}}\right)^{0.5} \left(-exp\left(\frac{\alpha_a F}{RT}\eta_c\right) + exp\left(\frac{-\alpha_c F}{RT}\eta_c\right)\right) \tag{3.9}$$

Where i^{ref} is the reference exchange current density of a unit active surface area, ζ_{eff} is the active surface area, C^{ref} is the reference value of the local species concentration, α is the charge transfer coefficient for either the cathode or the anode electrode, and F is Faraday's constant. η_a and η_c are the anodic and cathodic overpotentials and are obtained using the following expressions:

$$\eta_a = \phi_s - \phi_{mem} \tag{3.10}$$

$$\eta_c = \phi_s - \phi_{mem} - V_{oc} \tag{3.11}$$

Where V_{oc} is the open –circuit potential [88]:

$$V_{oc} = 1.229 - 8.456 \times 10^{-4}(\mathrm{T} - 298.15) + 4.31 \times 10^{-5}\mathrm{T}\log\left(P_{H_2} P_{O_2}^{0.5}\right) \tag{3.12}$$

The water in a PEM fuel cell have three phases: gaseous, liquid, and dissolved. The conservation of dissolved water could be expressed as follows [87]:

$$\nabla \cdot \left(\vec{\imath}_m \frac{n_d}{F} M_{H_2O}\right) = \nabla\left(M_{H_2O} D_w \nabla\lambda\right) + S_\lambda + S_{gd} + S_{ld} \tag{3.13}$$

where λ is water content, n_d the is osmotic drag coefficient, D_w is the diffusion coefficient, S_λ is the water generation rate at the cathode catalyst layer, S_{gd} is the change rate of water between the gaseous and dissolved phases, S_{ld} is the change rate of water between the liquid and dissolved phases. The mathematical definitions for all the source terms are presented in Table 3. The osmotic drag coefficient is given as follows [89]:

$$n_d = \frac{2.5\lambda}{22} \tag{3.14}$$

The diffusion coefficient of water content is obtained as follows [89]:

$$D_w^m = \frac{\rho_m}{EW} \cdot M_{H_2O} D_l \nabla\lambda \tag{3.15}$$

Where ρ_m and EW are the membrane dry density and membrane equivalent weight. The membrane water diffusivity is given as follows:

$$D_l = f(\lambda) e^{2416\left(\frac{1}{303} - \frac{1}{T}\right)} \tag{3.16}$$

Where $f(\lambda)$ is defined as follows:

$$f(\lambda) = \begin{cases} 10^{10} & \lambda < 2 \\ 10^{10}\lambda\left(1 + 2(\lambda - 2)\right) & 2 \le \lambda \le 3 \\ 10^{10}\lambda\left(3 - 1.67(\lambda - 3)\right) & 3 \le \lambda \le 4.5 \\ 1.25 \times 10^{10}\lambda\left(3 - 1.67(\lambda - 3)\right) & 4.5 \le \lambda \end{cases} \tag{3.17}$$

Water content is expressed as follows:

$$\lambda = \begin{cases} 0.043 + 1718a - 39.85a^2 + 36a^2 & (a < 1) \\ 14 + 1.4(a - 1) & (a > 1) \end{cases} \tag{3.18}$$

Water activity, a, is given as follows:

$$\mathrm{a} = \frac{P_{wv}}{P_{sat}} + 2s \tag{3.19}$$

where s is saturation of water vapour and P_{wv} is water vapour pressure:

$$P_{wv} = \chi_{H_2O} P \tag{3.20}$$

P_{sat} is saturation pressure:

$$\log_{10} P_{sat} = -2.1794 + 0.02953 \cdot (T - 273.15) - 9.1837 \cdot 10^{-5} \cdot (T - 273.15)^2 + 1.4454 \cdot 10^{-7} \cdot (T - 273.15)^3 \tag{3.21}$$

The impact of the liquid water on the operation of the fuel cell is accounted for by using the conservation of water saturation equation [87]:

$$\nabla \cdot \left(\frac{\rho_l K K_r}{\mu_l} \nabla (P_c + \mathrm{p}) \right) = S_{gl} \tag{3.22}$$

where μ_l is the dynamic viscosity of liquid water, P_c is the capillary pressure of the liquid water and K is the absolute permeability. S_{gl} is the mass change rate between the gas and liquid phases; its mathematical expression is shown in Table 3.3. K_r is the relative permeability and is given as follows:

$$K_r = \begin{cases} \dfrac{\frac{M_{H_2O}}{\rho_l}\lambda_{s=1} + \frac{EW}{\rho_i}}{\frac{M_{H_2O}}{\rho_l}\lambda + \frac{EW}{\rho_i}} & in\ the\ membrane \\ s & in\ the\ GDL\ and\ the\ CLs \end{cases} \tag{3.23}$$

P_c is the capillary pressure and is given as follows:

$$P_c \tag{3.24}$$

$$= \begin{cases} \sigma\cos(\theta)\left(\frac{\varepsilon}{K}\right)^{\frac{1}{2}} 1.417(1-s) - 2.12(1-s)^2 + 1.263(1-s)^3 \ (\theta < 90°) \\ \sigma\cos(\theta)\left(\frac{\varepsilon}{K}\right)^{1/2} 1.417s - 2.12s^2 + 1.263s^3 (\theta > 90°) \end{cases}$$

σ denotes the surface tension and θ is the contact angle.

D_{ij}^{eff} is calculated as follows: [88]

$$D_{ij}^{eff} = (1-s)^{1.5}\varepsilon^{1.5})(\frac{1}{D_{i,m}} + \frac{1}{D_{Kn}})^{-1} \tag{3.25}$$

$$D_{i,m} = D_i^{ref}(\frac{101325}{P})(\frac{T}{300})^{1.5} \tag{3.26}$$

$$D_{Kn} = \frac{1}{3} d_{pore}(\frac{8RT}{\pi M})^{0.5} \tag{3.27}$$

In this equation d_{pore} in this equation is defined as 0.2μm.

The parameters in Table 3.1 were chosen based on realistic data and consultation with other research studies.

Table 3.1 The parameters used in the model.

Parameter	**value**
Reference exchange current density at anode (i_a^{ref})	6000 A/m^2
Reference exchange current density at cathode (i_c^{ref})	0.0044 A/m^2
Thickness of membrane	0.05 mm

Thickness of catalyst layer	0.01 mm
Thickness of GDL	0.2 mm
Length of channel	50 mm
Height of channel	1 mm
Width of channel	1 mm
Cathode charge transfer coefficient (α_a)	0.5
Anode charge transfer coefficient (α_c)	1
Anode/cathode specific surface area (ζ_{eff})	1×10^6
Dry membrane density (ρ_m)	1980 kg/m^3
Membrane equivalent weight (EW)	1100 kg/kmol
H_2 molar concentration ($c_{H_2}^{ref}$)	54.6×10^{-3} kmol/m^3
O_2 molar concentration ($c_{O_2}^{ref}$)	3.39×10^{-3} kmol/m^3
Porosity of anode/cathode CL (ε)	0.4
Porosity of anode/cathode GDL (ε)	0.7

GDL/CL permeability (K)	$3 \times 10^{-12}/2 \times 10^{-13}$ m^2
GDL/CL contact angle (θ)	$110/95°$
Hydrogen diffusion coefficient (D_{H_2})	9.15×10^{-5} m$^2/s$
Oxygen diffusion coefficient (D_{O_2})	2.2×10^{-5} m$^2/s$
Nitrogen diffusion coefficient (D_{N_2})	2×10^{-5} m$^2/s$
Water vapor diffusion coefficient (D_{H_2O})	2.56×10^{-5} m$^2/s$
Thermal conductivity of CC	100 W/m/K
Thermal conductivity of GDL	21 W/m/K
Thermal conductivity of CL	0.3 W/m/K
Thermal conductivity of membrane	0.25 W/m/K
Electric conductivity of current collector (σ_{CC})	200000 S/m
Electric conductivity of gas diffusion layer (σ_{GDL})	5000 S/m
Electric conductivity of catalyst layer (σ_{CL})	2000 S/m
Hydrogen viscosity (μ)	8.411×10^{-6} Pa s

Liquid water viscosity (μ)	3.517×10^{-4} Pa s
Oxygen viscosity (μ)	1.919×10^{-5} Pa s
Water vapour viscosity (μ)	1.34×10^{-5} Pa s
Nitrogen viscosity (μ)	1.663×10^{-5} Pa s
Surface tension of water (σ)	0.0625 N/m
Gas mass exchange rate γ_{gd}	0.5
liquid mass exchange rate γ_{ld}	0.5
Water activity ($\lambda_{a=1}$)	9.2
Hydrogen diffusion coefficient ($D_{H_2}^{ref}$)	9.15×10^{-5}
Oxygen diffusion coefficient ($D_{O_2}^{ref}$)	2.2×10^{-5}
Water vapor diffusion coefficient ($D_{H_2O}^{ref}$)	2.56×10^{-5}
Water content at saturation ($\lambda_{s=1}$)	16.8

Source: [90],[91],[92]**.**

Table 3.2 The expressions for the source terms used in the governing equations.

Source term
$S_u = \frac{\mu}{K}\vec{u}$
$S_{H_2} = -\left({}^{M_{H_2}}/_{2F}\right) j_a \quad in\ ACL$
$S_{O_2} = -\left({}^{M_{O_2}}/_{4F}\right) j_c \quad in\ CCL$
$S_{H_2O} = -\frac{n_d j}{F} M_{H_2O} \quad in\ ACL$
$S_{H_2O} = \frac{n_d j}{F} M_{H_2O} + \left({}^{M_{H_2O}}/_{2F}\right) j_c \quad in\ CCL$
$S_c = \begin{cases} = -j_a & in\ ACL \\ = +j_c & in\ CCL \end{cases}$
$S_{mem} = \begin{cases} = +j_a & in\ ACL \\ = -j_c & in\ CCL \end{cases}$
$S_T = \begin{cases} \frac{i_s^2}{\sigma_{sol}} - S_{gl} & in\ GDLs \\ j_a\left(\eta_a - \frac{T\Delta S_a}{2F}\right) + \frac{i_s^2}{\sigma_{sol}} + \frac{i_s^2}{\sigma_{mem}} - \left(S_{ld} + S_{gl}\right)\cdot L & in\ ACL \\ j_c\left(\eta_c - \frac{T\Delta S_c}{2F}\right) + \frac{i_s^2}{\sigma_{sol}} + \frac{i_s^2}{\sigma_{mem}} - \left(S_{ld} + S_{gl}\right)\cdot L & in\ CCL \\ \frac{i_s^2}{\sigma_{mem}} & in\ CCs \\ 0 & in\ channels \end{cases}$

$$S_{gd} = (1-s)\gamma_{gd} M_{H_2o} \frac{\rho_m}{EW} (\lambda^{eq} - \lambda) \quad in\ membrane, ACL\ and\ CCL$$

$$S_{ld} = s\gamma_{ld} M_{H_2o} \frac{\rho_m}{EW} (\lambda^{eq} - \lambda) \ \ in\ membrane, ACL\ and\ CCL$$

$$\lambda^{eq} = 0.3 + 6a(1 - \tanh(a - 0.5) + 0.69(\lambda_{a=1} - 3.52)a^{0.5} \cdot (1 + \tanh\left(\frac{a - 0.89}{0.23}\right) + s(\lambda_{s=1} - \lambda_{a=1}))$$

$$S_{gl} = \begin{cases} \gamma_{gl}\varepsilon s D_{gl} \frac{M_{H_2o}}{RT} p \ln \frac{p - p_{sat}}{p - p_{wv}} & p_{wv} \le p_{sat} \\ \gamma_{gl}\varepsilon (1-s) D_{gl} \frac{M_{H_2o}}{RT} p \ln \frac{p - p_{sat}}{p - p_{wv}} & p_{wv} > p_{sat} \end{cases}$$

$$D_{gl} = \begin{cases} 0.365 \cdot 10^{-4} \left(\frac{T}{343}\right)^{2.334} \left(\frac{10^5}{p}\right) & in\ ACL \\ 1.79 \cdot 10^{-4} \left(\frac{T}{343}\right)^{2.334} \left(\frac{10^5}{p}\right) & in\ CCL \end{cases}$$

*** Abbreviations used in the table stand for the following: ACL: anode catalyst layer; CCL: cathode catalyst layer; CC: Current collector; GDL: gas diffusion layer.**

Sources: equations [87] [90],[91],[92]**.**

3.3.2 Boundary conditions and numerical procedure

The inlet boundary conditions, in terms of the mass fractions, temperatures, and relative humidity, are listed in Table 3. In addition, the zero-temperature flux and concentrations of the chemical species and zero-gauge pressures are set at the outlets of the flow channels:

$$\frac{\partial \mathrm{T}}{\partial \mathrm{n}} = 0 \tag{3.28}$$

$$\frac{\partial C}{\partial n} = 0 \tag{3.29}$$

$$P_g = 0 \tag{3.30}$$

where n is the normal vector and P_g is the gauge pressure. The solid phase potentials are set as follows:

$$\Phi_s = 0 \text{ at the anodic terminal} \tag{3.31}$$

$$\Phi_s = V_{cell} \text{ at the cathodic terminal} \tag{3.32}$$

where V_{cell} is the cell voltage and ranges between 0.4 V and the open circuit voltage. The other boundary conditions in table 3.3 are determined according to the realistic testing operating conditions.

The numerical model is solved using the PEMFC model within the ANSYS Fluent 2019 R3 software. The model is three-dimensional and multiphase and all of its governing equations (i.e. the conservation equations of each of: the chemical species, energy, charge, mass, momentum, water content, liquid saturation and user-defined scalars) are solved. To discretize the equations spatially, a second-order upwind method is used for all the equations. Three different mesh sizes were used to check for mesh-independent solutions: 100 × 15 × 50, 150 × 30 × 100 and 200 × 45 × 150 for the axes X, Y and Z, respectively. The difference in the current density at 0.5 V between the first and the second meshes was about 1.3% and between the second and the third meshes was about 0.5%. Therefore, the second mesh (150 × 30 × 100) was considered in this study to ensure both reasonable accuracy and computation time. Figure 3.3 shows the meshed geometry for the base case and Figure 3.4 shows the back views of the meshed geometries for the investigated cases. Note that the fuel cell flow

channels in Cases 1 and 2 have identical inlets and outlets, while the flow channels in Case 3 have dissimilar inlets and outlets, namely: rectangular inlets and trapezoidal outlets.

Table 3.3 The boundary conditions used in the simulation model.

Parameter	**Value**
Air/fuel stoichiometric ratio	$1.5/2$
Anode/cathode pressure	1/1
Mass fraction for H_2O at cathode inlet	0.103
Cathode/anode relative humidity	100%
Temperature at the channel inlets	353 K

Source: [88]

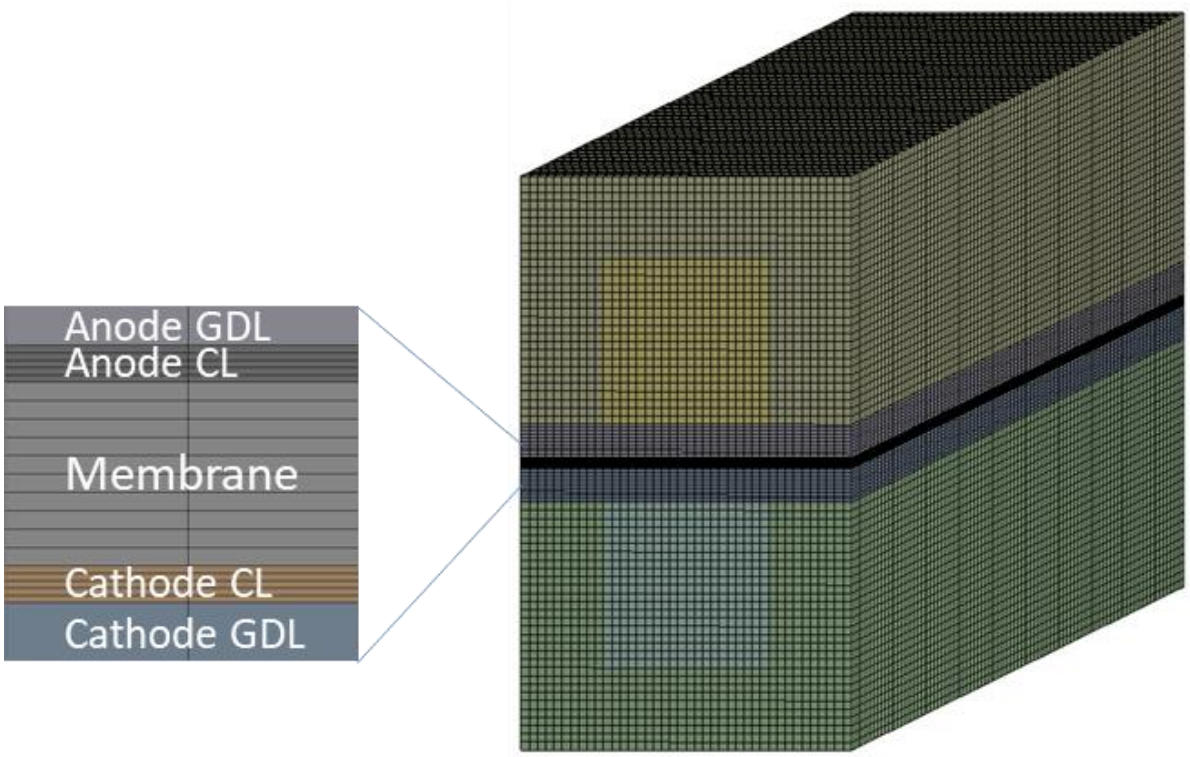

Figure 3.3 The meshed geometry of the base case. The zoomed-in picture shows the mesh across the membrane electrode assembly.

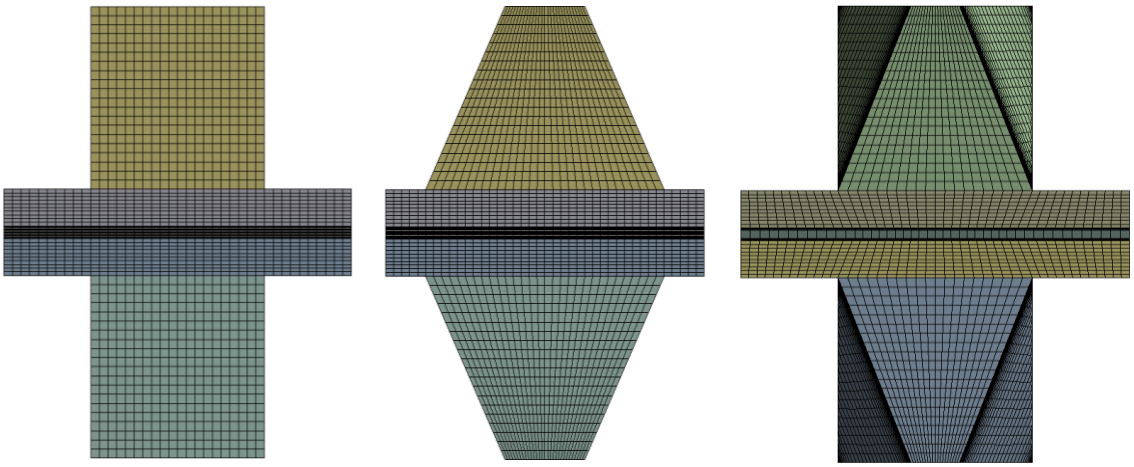

a b c

Figure 3.4 The back view of the meshed geometries for the investigated cases (a) Case 1 (rectangular cross-section), (b) Case 2 (trapezoidal cross-section), and (c) Case 3 (hybrid cross-section).

3.4 Results and discussion

Figure 3.5 shows that the modelling output in the form of the polarisation curve of the base computation case (the modelled fuel cell with square flow channels) are in reasonably good agreement with those reported by Wang et al. [92], thus imparting confidence into the predictions of the new proposed model.

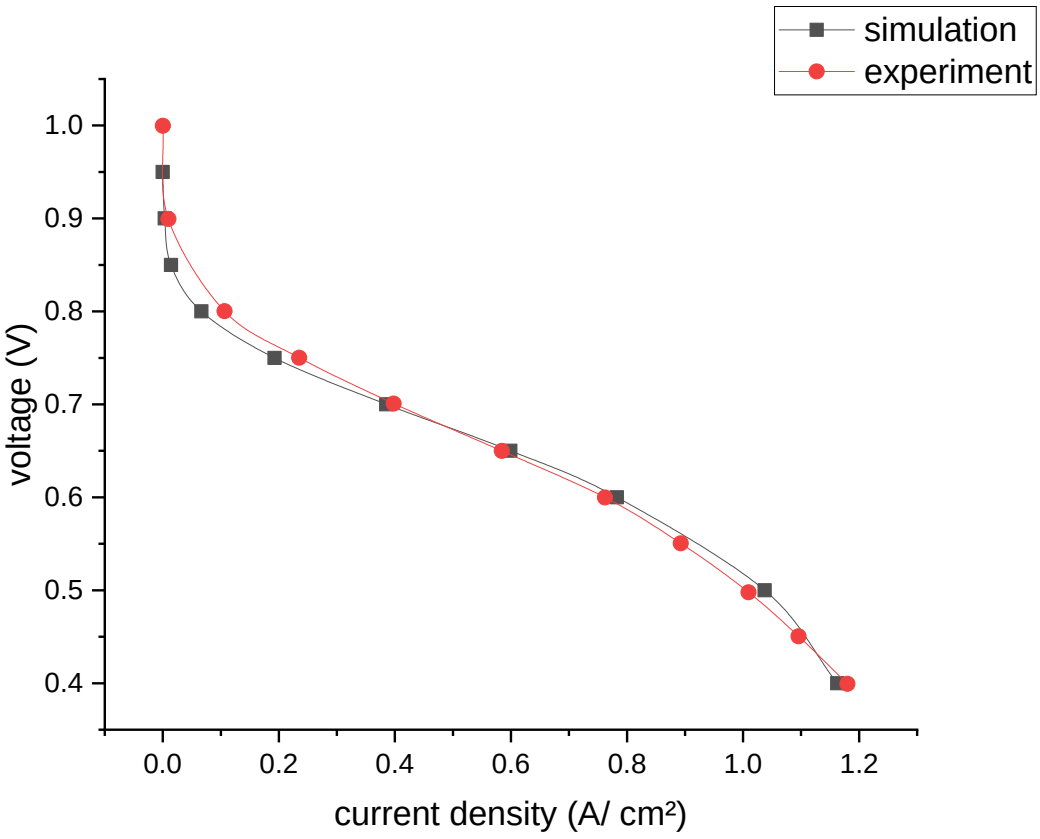

Figure 3.5 The polarisation curve generated by the modelled fuel cell for the base case as compared with the experimental polarisation curve taken from Wang et al. [92]**.**

Influence of the cross-sectional shape of the flow channel

Figure 3.6 displays the polarisation curves of the simulated fuel cell with flow channels of different cross-sectional geometries, namely, square, trapezoidal, and hybrid. The results

indicate that the variation in fuel cell performance is negligible for Cases 1 (square cross-section) and 2 (trapezoidal cross-section) with respect to a given cross-sectional area. This suggests that switching from a square to a trapezoidal cross-section has minimal impact on the fuel cell performance. However, Case 3 (hybrid cross-section as described in Section 3.2) demonstrates a slightly better performance at low cell potentials (e.g., 0.5 V) compared to Cases 1 and 2, with the current density at 0.4 V increasing by approximately 5% upon switching from a square to a hybrid cross-section. This important improvement can be attributed to the decrease in the channel cross-section from the inlet to the outlet, which results in an increase in the channel gas velocity (Figure 3.7) and subsequently and importantly facilitates the supply of reactant gases (oxygen or hydrogen) to the catalyst layers via convective flow in the Gas Diffusion Layers (GDLs) and Catalyst Layers (CLs). The availability of oxygen (Figure 3.8) at the cathode GDL-CL interface is also affected, with less oxygen being available for Case 3, thus indicating that more oxygen is supplied and consumed at the catalyst layer for this case. It is worth noting that the transport of species within typical GDLs, where the gas permeability is around 10^{-13} m², is dominated by diffusion (Ismail et al., 2012). This partly explains the slight improvement observed in the fuel cell performance when using the hybrid channel cross-sections.

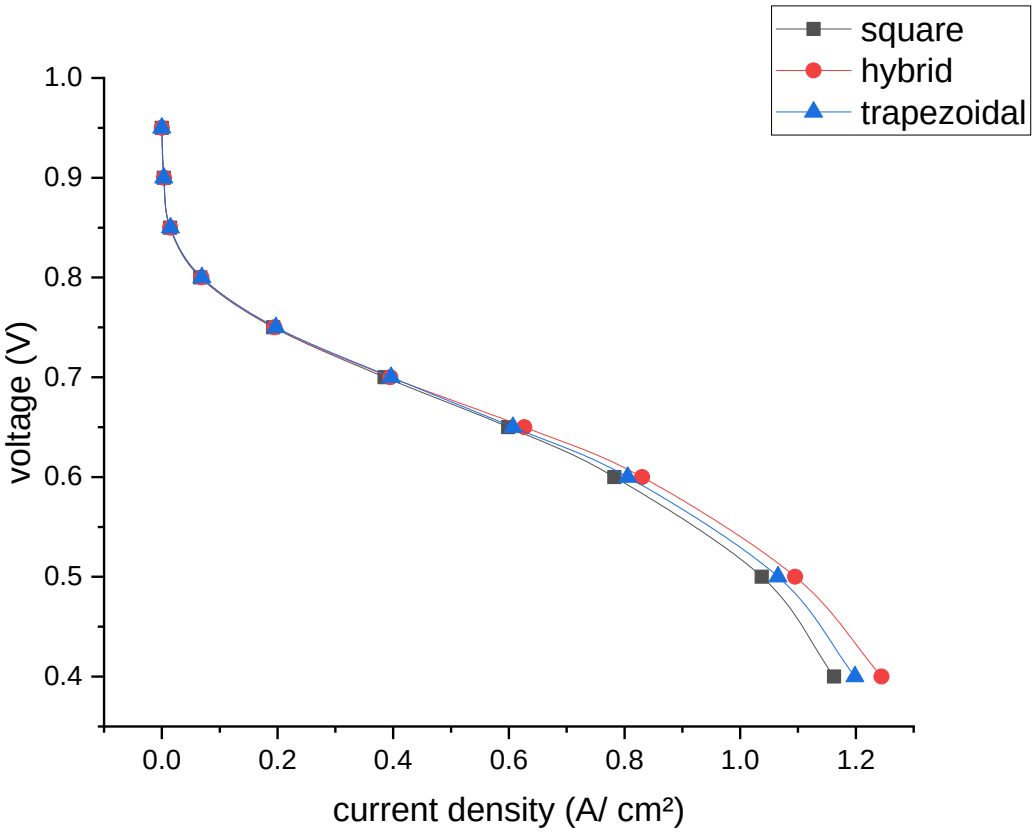

Figure 3.6 The polarisation curves of the modelled PEM fuel cell with square, trapezoidal and hybrid flow channels.

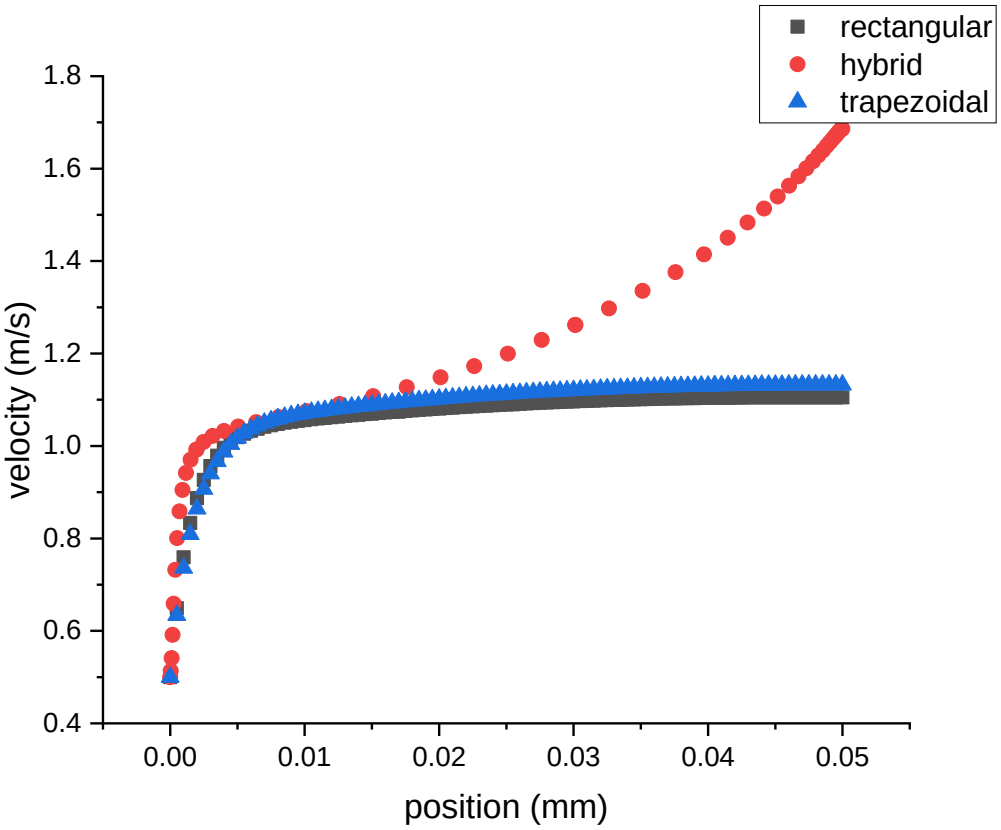

Figure 3.7 The velocity profile at 0.5 V along the middle line of the cathode flow channel with: rectangular, trapezoidal and hybrid cross-sections.

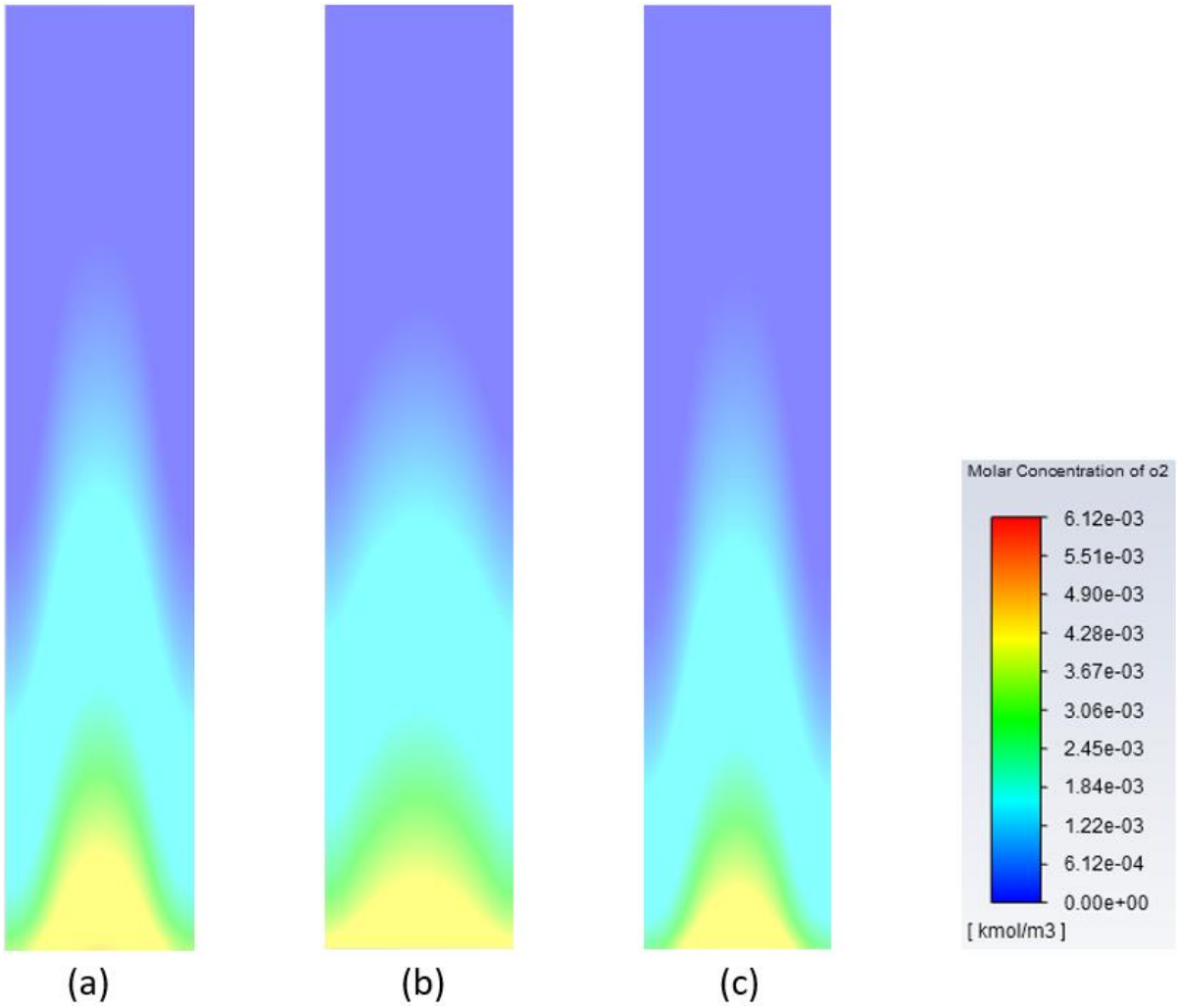

Figure 3.8 The contours of the oxygen concentration (kmol/m^3) at the interface between the cathode CL and GDL at 0.5V with various cross-section shapes: (a) rectangular, (b) trapezoidal and (c) hybrid cross-sections.

Table 3.4 presents the pressure drop data obtained for the different channel cross-sections investigated. It is interesting and important to note that the results reveal that the use of the hybrid cross-sections leads to an increase in the pressure drop along the cathode channel, which promotes higher convective flow rates and, subsequently, better heat and excess water removal. This is demonstrated by the temperature difference along the channel and the water concentration at the exit of the cathode channel, both of which show an improvement when using the hybrid cross-sections compared to the other cases investigated. In addition, the

average temperature difference along the channel increased by 0.05°C when switching from the square to the hybrid cross-sections. Similarly, the liquid water exiting the cathode channel increased when using the hybrid cross-sections compared to the square or trapezoidal cross-sections. Comparable observations can be made for the anode flow channels (not shown), although the effect is less pronounced due to the lower flow rates used in those channels. Moreover, Table 3.4 shows that the use of trapezoidal cross-sections results in a slightly higher pressure drop along the channel compared to the square cross-sections, thereby improving the heat dissipation and excess water removal. Also, the temperature difference and water concentration at the channel exit for trapezoidal cross-sections are comparable to those of the hybrid cross-sections. These findings confirm the hypothesis that switching from a square to a trapezoidal cross-section or to the novel proposed hybrid flow channel has a positive impact not only on the fuel cell performance but also on other key performance indicators.

Table 3.4 The pressure drop, temperature difference along the cathode channel and water concentration at the cathode channel exit for the investigated cases.

Cross-section shape	**Pressure drop along cathode channel (Pa)**	**Temperature difference (°C)**	**Water concentration at channel exit (kmol/m^3)**
Rectangular	13.3	0.17	0.0138
Trapezoidal	15.1	0.20	0.0151
Hybrid	19.0	0.22	0.0154

Influence of the outlet height

The modelled fuel cell with hybrid flow channels shows slightly better performance than those with square or trapezoidal flow channels. However, to further improve the performance of the fuel cell, the height of the outlet of the hybrid channel has been varied from the original case of 1 mm to 0.75, 0.50, and 0.25 mm. Figure 3.9 shows that the limiting current density increases slightly as the outlet height decreases. Specifically, the current density at 0.4 V increases by about 6% when the channel height decreases from 1 to 0.25 mm. According to the Bernoulli's principle, as the cross-sectional area of the flow channel decreases, and the mass flow rate remains constant, the velocity must increase to maintain the same mass flow rate. Thus this nozzle like configuration will increase the velocity of the gas flow, which is beneficial to the reactant to transport to the reaction area. In addition, high speed flow can increase the magnitude of the diffusion term in the species conservation equation, which describes how molecules move and diffuse through the gas channel. This can intern affect the convection term of the equation, which describes the transport of the molecules due to the bulk flow of the gas. As shown in Figure 3.10, the velocity magnitude increases when the height of the channel decreases in the direction of the gas flow; this enhances the supply of the reactant gases to the reactive areas in the catalyst layer through the increased convective flow and the convective diffusion within the porous media. Considering the conservation of mass principle and ignoring the slight amount of the reactant gases being consumed at the catalyst layers, the mass flow rate in the flow channel flow remains constant. This means that as the cross-section area of the flow channel decreases (as is the case in the proposed hybrid flow channel), the velocity increases in order to conserve the mass. Figure 3.11 demonstrates that the concentration of oxygen at the interface between the cathode GDL and the CL decreases as the channel height decreases, indicating that more oxygen is supplied to and consumed at the catalyst layer. This suggests that decreasing the channel

height can improve the performance of the fuel cell. However, it is important to note that decreasing the channel height can also increase the pressure drop along the channel, which may have negative effects on the performance of the fuel cell and should be considered in further optimization investigations.

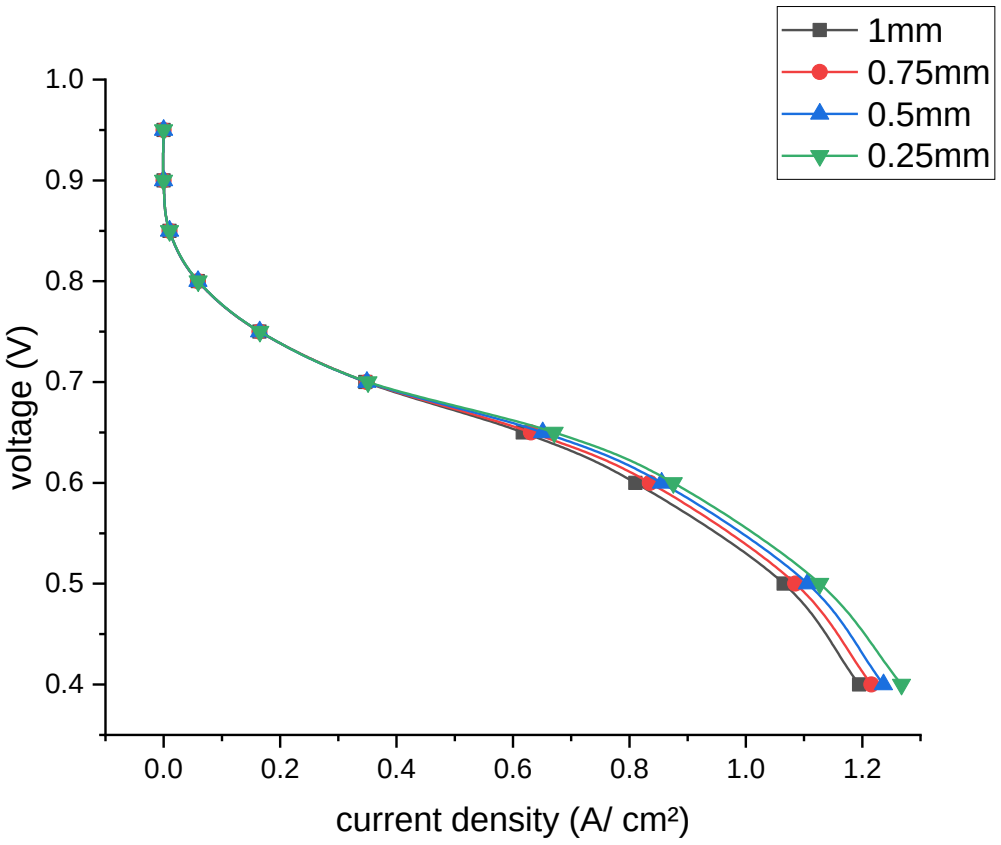

Figure 3.9 The polarisation curves of the modelled PEM fuel cell with varying outlet heights for hybrid channels.

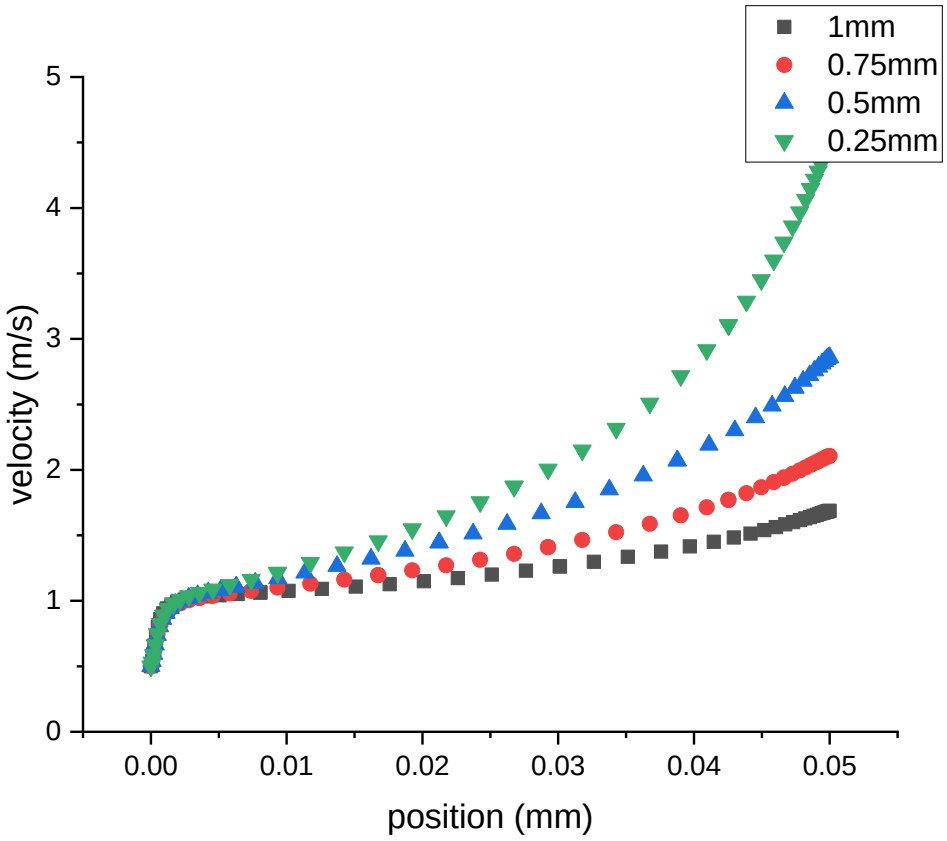

Figure 3.10 The velocity profiles at 0.5 V along the middle line of the hybrid cathode flow channel with varying outlet heights.

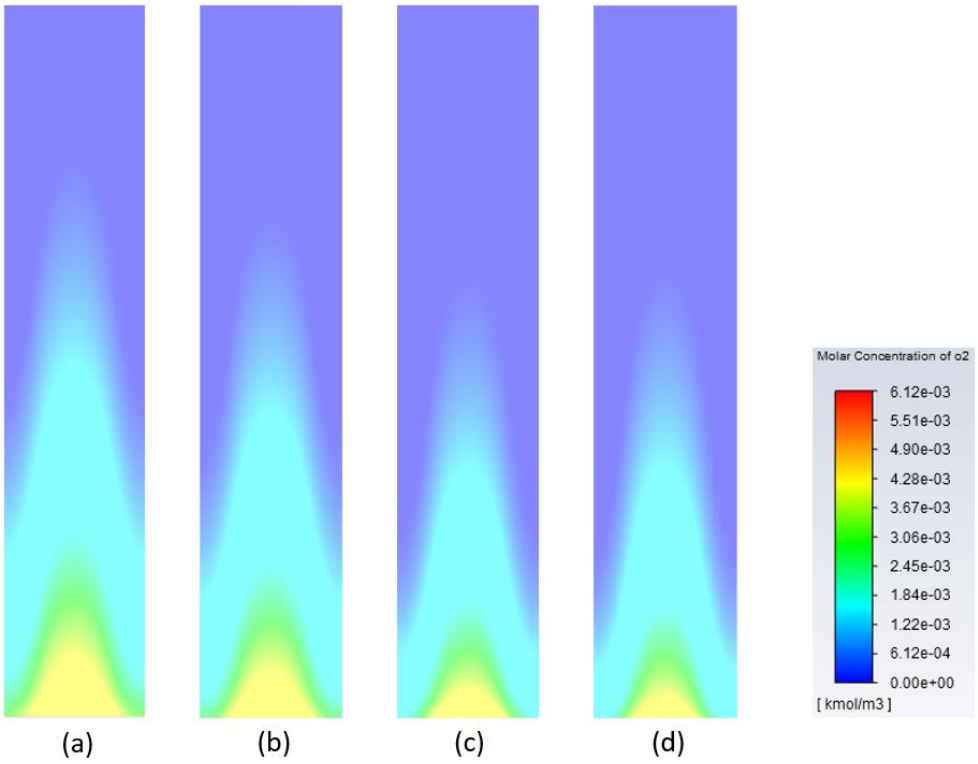

Figure 3.11 The contours of the oxygen concentration at the interface between the cathode GDL and the CL at 0.5V with different heights at the outlet: (a) 1.0mm, (b) 0.75mm, (c) 0.5mm and (d) 0.25mm.

Table 3.5 presents the impact of the outlet height on the additional key performance indicators of the modelled fuel cell. The table shows that as the outlet height decreases from 1 to 0.25 mm, the pressure drop along the cathode flow channel increases almost fourfold, and this is primarily due to the increase in the gas velocity. This increase in velocity improves the heat dissipation and excess water removal. Specifically, the difference in the temperature between the inlet and outlet of the cathode channel, averaged across the channel, increases by 0.77 °C, and the amount of liquid water exiting the cathode flow channel slightly increases from 0.0154 to 0.0157 kmol/m³. However, it should be noted that the increased pressure drop requires relatively high pumping power to maintain the flow rate, which can decrease the system efficiency and increase the costs. Therefore, optimizing the pressure drop along the flow channels in real-life fuel cell systems is critical to ensure both acceptable efficiency and

cost-effectiveness. Overall, all the above findings highlight the importance of considering multiple key performance indicators when evaluating the performance of a fuel cell, rather than focusing on the polarisation curve as a single performance indicator. In doing so, researchers can obtain a better understanding of the multifaceted impacts of the various parameters; this ultimately leads to having better insights on how to improve the efficiency and the effectiveness of the fuel cell.

Table 3.5 The pressure drop, temperature difference along the cathode channel and the water concentration at the cathode channel exit as they change with outlet height.

Outlet height (mm)	Pressure drop along cathode channel (Pa)	Temperature difference (°C)	Water concentration at channel exit (kmol/m^3)
1.00	19.0	0.22	0.0154
0.75	22.1	0.88	0.0155
0.50	32.5	0.95	0.0156
0.25	77.6	0.99	0.0157

3.5 Conclusions

A comprehensive three-dimensional numerical model has been created for a polymer electrolyte membrane fuel cell. This has been performed to investigate the impact of switching from a commonly used square flow channel cross-section to an increasingly used trapezoidal cross section and a hybrid cross-section (where the cross-section at the inlet is square and the cross-section at the outlet is trapezoidal) on the global and local performance

of the fuel cell. The results show that the fuel cell with hybrid flow channel cross-sections generally perform better than other configurations, particularly at high current densities. Namely, the current density increased by around 5% at 0.4 V when switching to hybrid configuration. This is attributed to the increased velocity in the hybrid flow channel (due to gradually decreasing cross-section from the inlet to the outlet) which is responsible for supplying higher amount of reactant gases to the catalysts layers. Further, this hybrid configuration, compared to other configurations, results in better heat dissipation and removal of excess water. Furthermore, reducing the height of the outlet of the hybrid cross section demonstrates a better fuel cell performance. For example, reducing the height of the outlet from 1 to 0.25 mm for this configuration results in an increase in the current density at 0.4 V by 6%. As with the first investigation, this is evidently due to increased velocity with decreasing outlet height which brings more amounts of reactant gases to the catalyst layers, dissipates heat and remove excess water more effectively. As a future work, the proposed hybrid flow channel design could be applied to other common flow configurations, particularly serpentine flow configuration. It could be also applied to the entire fuel cell. Such applications should provide insights on the sensitivity of the performance of the fuel cell equipped with the proposed flow channel design to the flow configuration and the size of the computation domain (i.e. single turn of the fuel cell versus the full fuel cell); the sensitivity of other key parameters (e.g. water and thermal management) could be also investigated. These insights would ultimately lead to better flow channel designs and more efficient fuel cells.

Chapter 4 Exploring catalyst microstructure parameters in PEM fuel cells through numerical modelling

4.1 Abstract

This chapter focuses on the catalyst layer's (CL) microstructure, a pivotal element influencing PEM fuel cell performance. The choice of the agglomerate model in this study is justified by its comprehensive treatment of mass transfer losses, including microstructural effects, setting it apart from thin-film and macro-homogeneous models, which often produce results surpassing experimental data due to their neglect of microstructure. Furthermore, this research investigates the impact of catalyst properties, including Pt loading and particle size, on PEM fuel cell performance. The optimal Pt particle size for catalytic activity remains a subject of interest, with diverse research outcomes necessitating further exploration. The chapter concludes by highlighting the promise of carbon-based materials, particularly graphene, as catalyst supports within PEM fuel cells. These materials exhibit the potential to augment electrochemical performance and enhance mass transfer efficiency. In essence, this chapter underscores the pivotal role of microstructural considerations and modelling in advancing PEM fuel cell technology, with a specific focus on catalyst layer properties and their profound implications for fuel cell performance and design.

4.2 Introduction

In the past three decades, numerical models of PEM fuel cells from 1D to 3D have been well-developed. The model's restrictive assumptions have been substantially reduced, and the degree of simplification has also become much smaller. The early one-dimensional mathematical model was mainly dedicated to the simulation of the basic electrochemistry,

gas diffusion layer, catalyst layer and proton exchange membrane. The one-dimensional mathematical model explains the most basic electrochemical and transport phenomenal in PEM fuel cells. Next, the model was further improved, adding considerably to the change in reactant concentration in the direction of the gas flow [89]. The early two-dimensional model helped solve the problem of reactant distribution and local current density in the flow direction [93]. With the development of computational fluid mechanics, new models have been used to simulate physics in the entire components of the flow channels, gas diffusion layers and catalyst layers.

At present, the three-dimensional numerical models of PEM fuel cells are well developed. In these three-dimensional models, the conservation equations of mass, momentum and species have been solved in the gas flow channels, the membrane electrolyte and the porous media (the gas diffusion layers and the catalyst layers) [94]. These three-dimensional models are now used to study and optimize the catalyst layer, improve the overall performance and durability of the fuel cell, and they have achieved good agreement between the numerical and experimental results. The following subsections present the governing equations, parameters and the boundary conditions that are normally used for the PEMFC models. The chapter ends with a presentation for the meshed geometry of the modelled fuel.

The catalyst layer is a porous network composed of agglomerates. The size of the agglomerates is about 200 nm, and there are void spaces inside. The pores in the agglomerates that are less than 20 nm are called primary pores [95]. Between the agglomerates, the secondary pore size is greater than 20 nm. Pores smaller than 2 nm may be blocked by Pt particles and pores 2-20 nm may be occupied by ionomers [96]. The secondary pores with larger sizes are mainly used as gas transmission channels [97]. The catalyst layer within the fuel cell comprises three phases: the ionomer phase, Pt/C, and gas pores. Figure 4.1 (a) presents a schematic of the catalyst layer's microstructure. The ionomer

serves as both a proton conductor and a binder for the Pt/C, aiding in retaining moisture and preventing membrane dehydration. Meanwhile, Pt/C provides active sites for catalysis and pathways for electron transport. The porous structure facilitates the reach of reactants to the reaction sites and offers pathways for the removal of produced water at the cathode side. Figure 4.1 (b) depicts the interface between Pt/ionomer and gas/ionomer. In this interface, the ionomer envelops the Pt/C particles, assuming a spherical and evenly distributed agglomerate within the CL[98]. Numerical simulation is a very suitable approach to study the effects of the catalyst microstructure on the performance of PEM fuel cells. At present, three models are developed to describe the microstructure of the CL: thin-film models [99], macro-homogeneous models [100] and agglomerate models [90].

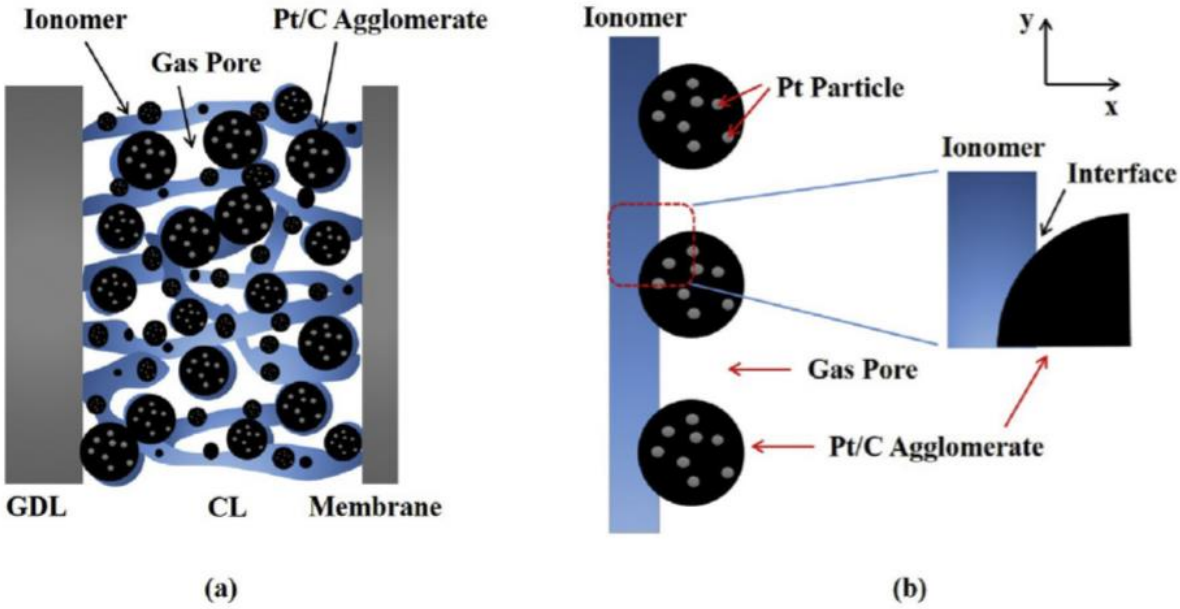

Figure 4.1 (a) Schematic of the catalyst layer (CL) microstructure with ionomer, Pt/C agglomerate and gas pores, and (b) simplified CL microstructure with a detailed interface of Pt/C agglomerate [98]**.**

A large number of studies have shown that because the catalyst agglomerate model takes into account the influence of the microstructure, it is the only model that can simulate all mass transfer losses. Compared with the agglomerate model, the simulation results of the

thin film models and the macro-homogeneous models will be higher than the actual experimental results. This is because of the effect of the microstructure on the mass transfer and the resistance is not considered in the thin film model. In the macro-homogeneous model, the formation of agglomerates is ignored. Therefore, it cannot reflect the dissolution of the reactants at the interface of the gas and ionomer. The diffusion and reaction of the reactants in the pore structure is also neglected. The agglomerate models can be used to describe all transmission processes in the CL. For example, the transport and reactant in the gas and dissolute phase in the pores of the catalyst; transport of ions, and conduction of electrons in the electrolyte phase.

The activity and durability of the catalyst are the key indicators that can influence the performance of the fuel cell. In the PEM fuel cell using a carbon-supported Pt catalyst, the activity and durability of the electrochemical catalyst are related to the catalyst loading and catalyst size. At present, the goal of the research of catalysts in PEM fuel cells is to reduce the Pt loading to 0.125 mg /cm^2 . However, in the future, the Pt loading of commercial fuel cells will be further reduced.

High Pt loadings will accelerate the rate of the oxygen reduction reaction because more catalyst provides more catalyst surface area. Similarly, if one requires to reduce both the Pt loading and the catalyst to maintain a high catalytic rate, then the simple and very effective method is to increase the active surface area of the catalyst by reducing the diameter of the platinum particles [101]. In the past research, Peuckert et al. found that the radius of the Pt particle that makes the catalyst the most catalytically active is 4nm [102]. However, if the particle radius is too small, the catalytic performance will also be significantly reduced. In a large number of simulations, particles of radius 2-5 nm are used as simulation parameters (Malek et al., 2011). Soboleva et al. found that the microstructure of the carbon support can also determine the distribution of the Pt particles in the catalyst layer [96]. However, some

researchers have found that even if the radius is reduced to 1.4 nm, no clear effect of the particle size is found (Watanabe et al., 1988). The above inconsistent research conclusions indicate that the microstructure of the catalyst layer and its influence on the fuel cell system still needs to be further studied.

The ionomer volume fraction is another important parameter that affects the PEM fuel cells. The network structure of the ionomer can be used as a medium for the reactants to reach the reaction site and can also provide a channel for the diffusion of oxygen. Some researchers have studied the content of ionomers and found the optimized ionomer volume fraction that can make the fuel cell obtain the best performance[105]. The role of the ionomer is to bind the Pt particles and carbon black particles together; therefore, it is necessary to analyse all the components in this structure. Carbon black is currently the most commonly used catalyst support in PEM fuel cells. In addition to supporting the Pt particle catalyst, and it also serves as an electron transfer material to conduct electrons to the site of catalyst action. In addition to the high porosity, the porous carbon-based material with a pore size of 2-20nm has good electrical conductivity and thermal conductivity. These characteristics ensure that it has better mass transfer performance [106]. However, if the pore size is too small, such as when the pore size is less than 2 nm, the catalyst particles may block these pores, thereby reducing the overall mass transfer efficiency [96]. These structures with a pore size of less than 2 nm are considered to be the active sites for platinum deposition and do not affect the performance of the fuel cell. The designed carbon nanostructures, such as graphene, can replace carbon black due to its microstructure that can increase the surface area, as well as good thermal conductivity, electrical conductivity, and excellent stability. In recent years, the Cardadea research group and others have studied the use of graphene as a catalyst layer and found that graphene can improve the electrochemical performance and thus the performance of PEM fuel cells [107]. Using graphene as the fuel cell catalyst can provide more channels, thus

allowing more efficient transportation of reactants and products, as well as better particle and electron conductivity. These improvements benefit from the new structure, multiple active sites and pores, provided by graphene. In addition to graphene, other carbon nanomaterials and heteroatom-doped carbon nanomaterials have also become potential replacement materials for oxygen reduction reactions, and further research is needed in the future. In this research, the effect of different microstructure of the catalyst such as, Pt particle radius, Pt loading, and specific surface area on the performance of the fuel cells are studied.

4.3 Model description

The model presented in this section is developed based on the conservation equations for mass, species, charge, and energy. This has been elaborated in detail in the previous chapter. The assumptions used in this model are as follows: the fuel cell operates under steady conditions, the gas-phase reactants are non-compressible and exhibit laminar flow. The gases are considered ideal. This model is employed to investigate the influence of the catalyst layer's microstructure, necessitating the consideration of micro parameters. Regarding the catalyst, the assumption is that it takes the form of spherical agglomerates consisting of platinum particles, ionomer, and porous areas. The pores are filled with ionomer and water, thus enabling the transport of ions and the gas transfer.

4.2.1 Governing equations

The current density is determined using the Butler-Volmer equation, the specific surface area ζ_{eff}, can be influenced by the microstructure of catalyst and these are presented in the following equations:

$$J_a = i_a^{ref} \zeta_{eff} \left(\frac{P_{H_2}}{C_{H_2}^{ref} H_{H_2}} \right)^{0.5} \left(exp\left(\frac{\alpha_a F}{RT} \eta_a \right) - exp\left(\frac{-\alpha_c F}{RT} \eta_a \right) \right) \quad (4.1)$$

$$J_c = i_c^{ref} \zeta_{eff} \left(\frac{P_{O_2}}{C_{O_2}^{ref} H_{O_2}} \right)^{0.5} \left(-exp\left(\frac{\alpha_a F}{RT} \eta_c \right) + exp\left(\frac{-\alpha_c F}{RT} \eta_c \right) \right) \quad (4.2)$$

Where i^{ref} represents the reference exchange current density per unit active surface area, ζ_{eff} is the active surface area, C^{ref} stands for the reference value of the local species concentration, α denotes the charge transfer coefficient for either the cathode or the anode electrode, and *F* corresponds to Faraday's constant.

Specific active surface area ζ_{eff} is determined by the loading of the Pt particles (m_{pt}) and electrochemically active surface (a_{ECSA}) [108]:

$$\zeta_{eff} = (a_{ECSA} \cdot m_{pt}) / \delta_{cl} \quad (4.3)$$

The radius of Pt particles, r_p (m) is expressed by the following equation [109][109] :

$$r_p = 3/(a_{ECSA} \cdot \rho_{pt}) \quad (4.4)$$

4.2.2 Boundary Conditions and Parameters

Commercial software ANSYS Fluent 2019 R3 has been used to solve the conservation equations listed in the previous section. The boundary conditions and the physical parameters used in this study are shown in Tables 4.1 and 4.2, respectively. To generate the polarisation curve for the fuel cell, the solid phase potential on the anode side was set to 0 V and the solid and between 0 V and the open-circuit voltage for each run. For more detail, please revisit Chapter 3.

Table 4.1 The parameters used in the model.

Parameter	value
Reference exchange current density at anode (i_a^{ref})	6000 A/m^2
Reference exchange current density at cathode (i_c^{ref})	0.0044 A/m^2
Thickness of membrane	0.05 mm
Thickness of catalyst layer	0.01 mm
Thickness of GDL	0.2 mm
Length of channel	50 mm
Height of channel	1 mm
Width of channel	1 mm
Cathode charge transfer coefficient (α_a)	0.5
Anode charge transfer coefficient (α_c)	1
Anode/cathode specific surface area (ζ_{eff})	1×10^6
Dry membrane density (ρ_m)	1980 kg/m^3

Membrane equivalent weight (EW)	1100 kg/kmol
H_2 molar concentration ($c_{H_2}^{ref}$)	54.6×10^{-3} kmol/m^3
O_2 molar concentration ($c_{O_2}^{ref}$)	3.39×10^{-3} kmol/m^3
Porosity of anode/cathode CL (ε)	0.4
Porosity of anode/cathode GDL (ε)	0.7
GDL/CL permeability (K)	$3 \times 10^{-12}/2 \times 10^{-13}$ m^2
GDL/CL contact angle (θ)	$110/95°$
Hydrogen diffusion coefficient (D_{H_2})	9.15×10^{-5} m$^2/s$
Oxygen diffusion coefficient (D_{O_2})	2.2×10^{-5} m$^2/s$
Nitrogen diffusion coefficient (D_{N_2})	2×10^{-5} m$^2/s$
Water vapor diffusion coefficient (D_{H_2o})	2.56×10^{-5} m$^2/s$
Thermal conductivity of CC	100 W/m/K
Thermal conductivity of GDL	21 W/m/K
Thermal conductivity of CL	0.3 W/m/K

Thermal conductivity of membrane	0.25 W/m/K
Electric conductivity of current collector (σ_{CC})	200000 S/m
Electric conductivity of gas diffusion layer (σ_{GDL})	5000 S/m
Electric conductivity of catalyst layer (σ_{CL})	2000 S/m
Hydrogen viscosity (μ)	8.411×10^{-6} Pa s
Liquid water viscosity (μ)	3.517×10^{-4} Pa s
Oxygen viscosity (μ)	1.919×10^{-5} Pa s
Water vapour viscosity (μ)	1.34×10^{-5} Pa s
Nitrogen viscosity (μ)	1.663×10^{-5} Pa s
Surface tension of water (σ)	0.0625 N/m
Gas mass exchange rate γ_{gd}	0.5
liquid mass exchange rate γ_{ld}	0.5
Water activity ($\lambda_{a=1}$)	9.2
Hydrogen diffusion coefficient ($D_{H_2}^{ref}$)	9.15×10^{-5}

Oxygen diffusion coefficient ($D_{O_2}^{ref}$)	2.2×10^{-5}
Water vapor diffusion coefficient ($D_{H_2O}^{ref}$)	2.56×10^{-5}
Water content at saturation ($\lambda_{s=1}$)	16.8

Table 4.2 The boundary conditions used in the simulation model.

Parameter	**Value**
Air/fuel stoichiometric ratio	$1.5/2$
Anode/cathode pressure	1/1
Mass fraction for H_2O at cathode inlet	0.103
Cathode/anode relative humidity	100%
Temperature at the channel inlets	353 K

4.2.3 Geometry and mesh

The computational domain shown is developed with the ANSYS FLUENT 2019 R3 software. A mesh with approximately 510,000 elements was found to give mesh-independent solution. The fuel cell in the present study has a symmetrical structure on both sides, therefore a single channel pair is used for the numerical studies. In the numerical study, the flow fields on the anode and cathode sides are the same and are parallel single channels.

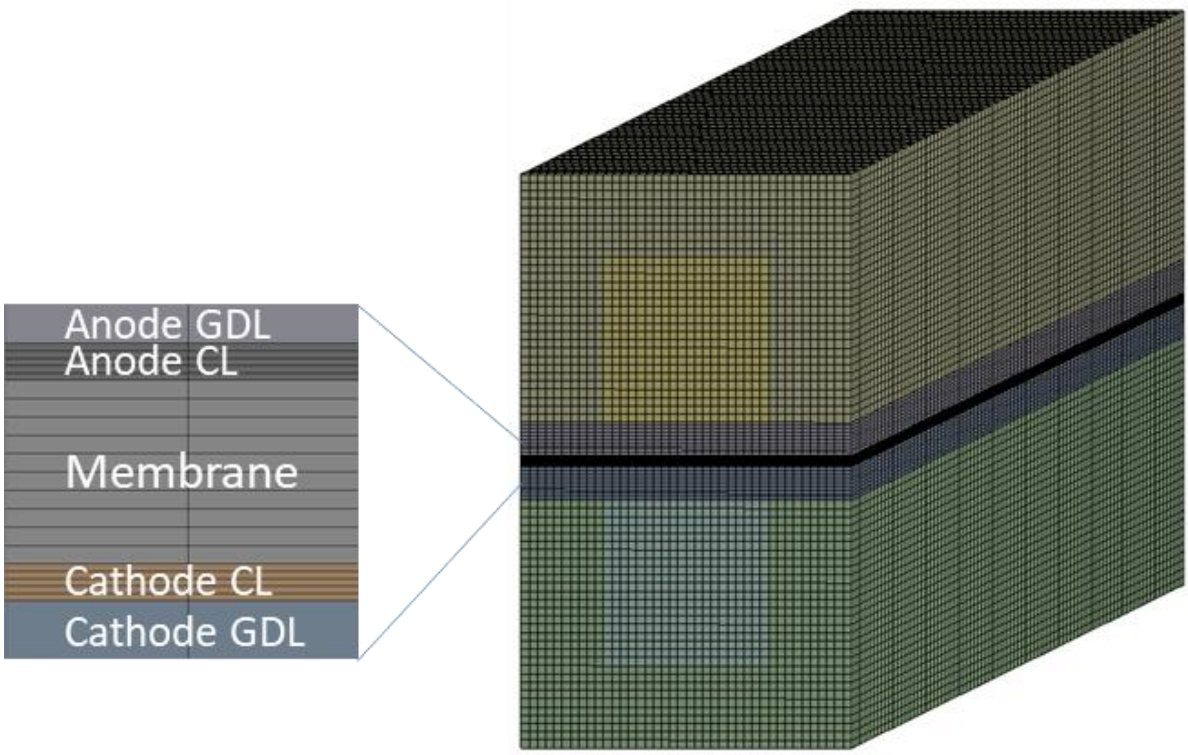

Figure 4.2 The mesh and geometry of the model.

4.4 Results and discussion

A numerical investigation of a single-channel PEM fuel cell is presented, exploring the impact of different catalytic microstructures (such as Pt particle radius, Pt loading, and specific surface area) on fuel cell performance. Platinum serves as a crucial element in PEM fuel cell catalysts, and most commercial PEM fuel cells employ carbon powder as a catalyst support. The numerical model built in this study has been validated using experimental data generated by Marinoiu et al. [107] Figure 4.3 shows an excellent agreement (correlation coefficient r=0.9374) between the output of the current model and the experimental data. Different cathode catalyst layers have different electrochemically active areas (a_{ECSA}) resulting in different microstructural properties. The electrochemical active area measurement was performed by cyclic voltammetry. The results showed that the higher the (a_{ECSA}) value of the catalyst, the better the performance. Utilizing Equation 4.1 and the catalyst performance data, the simulation indicates that the Pt particle radius in the model is 4.38 nm, and the porosity is 0.7, as specified in Table 4.1. Based on these attributes, it can be concluded that the numerical simulations accurately represent the electrochemical performance as depicted by polarization curves (experimental) and points (CFD simulation) shown in Figure 4.2. The close resemblance between the CFD results and the experimental data establishes the successful validation of the model.

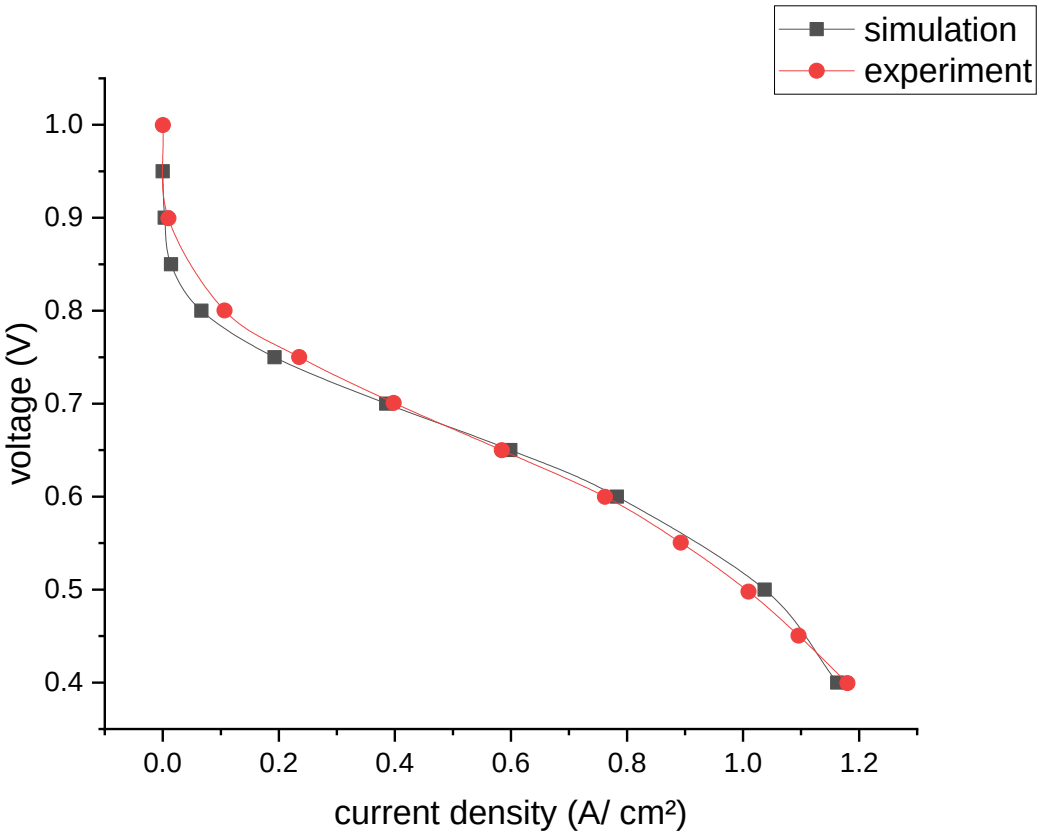

Figure 4.3 The validation of the numerical model against the experimental data.

4.3.1 Platinum loading

Platinum loading emerges as a pivotal parameter necessitating thorough analysis, given that it has a profound influence on fuel cell performance. The architecture of platinum supported on a carbon catalyst involves the intricate amalgamation of Nano-scale platinum particles with a matrix of high surface area carbon powder. Contemporary trends lean toward adopting a relatively modest platinum loading, approximately around 0.125 mg /cm^2or, in some cases, even lower. In the catalyst layer, a higher catalyst loading typically enhances performance. However, increased loading results in larger particle clusters, creating a longer path for reactants to reach the catalyst agglomerate's core. Conversely, if the loading is too low, it leads to underutilization of the contact surface, thereby diminishing the reaction rate. A

particularly efficacious avenue for achieving reduced Pt loading involves the meticulous reduction of Pt particle size. To simplify the model and based on equation 4.1, 4.2, 4.3 and 4.4, here the assumption of the relationship between catalytic activity and particle radius/volume/size is linear. In this research the catalyst particles were assumed uniformly distributed and the size are the same. It is within the confines of this conceptual framework that our model takes shape. In this study, the platinum loading was systematically manipulated, spanning a range from 0.05 to 0.4 mg/cm^2.

Evidently, as depicted in Figure 4.3, the augmentation in the catalyst platinum loading corresponds to a discernible rise in the current density. However, the trajectory of the curve shows a point of saturation after a certain platinum loading threshold. This intriguing phenomenon can be rationalized by the heightened reaction rate at elevated loadings, thus leading to a surplus production of water molecules. Consequently, an excessive presence of water molecules can impede the efficient transfer of oxygen molecules to the catalyst layer, resulting in the observed plateau effect.

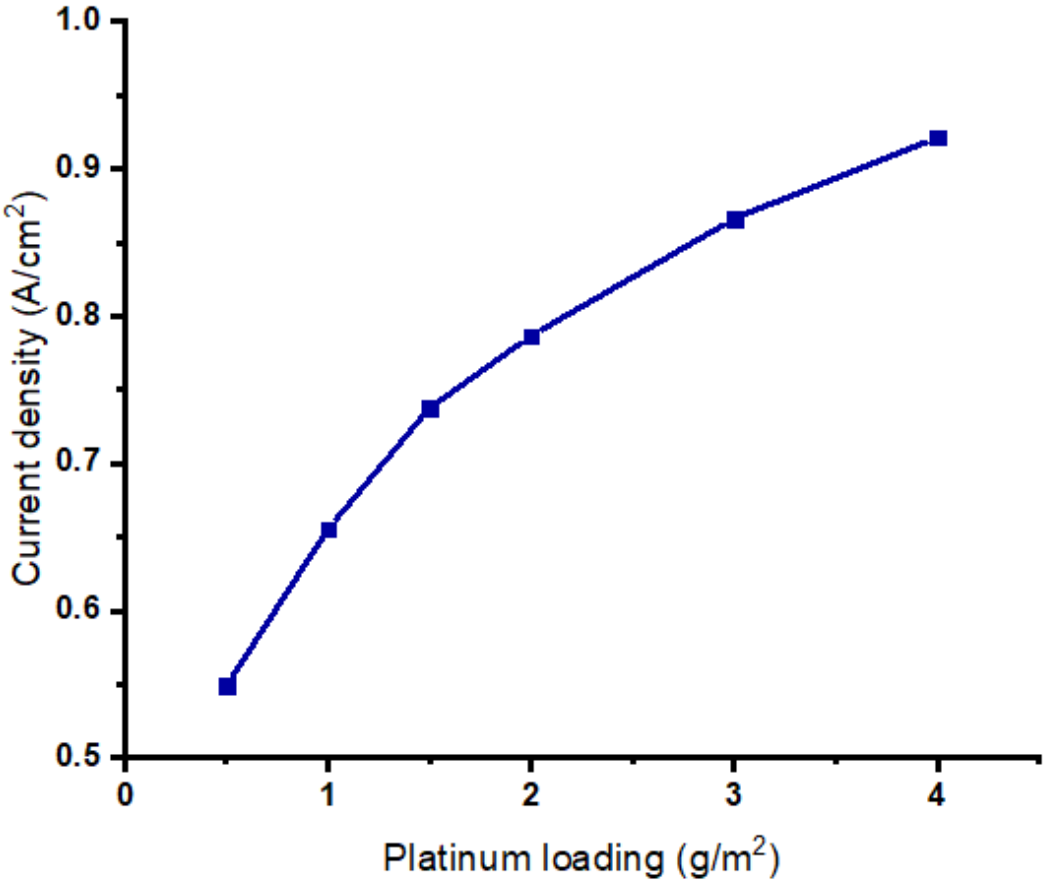

Figure 4.4 Platinum mass loading influence on the current density at 0.6 V.

4.3.2 Particle radius

Figure 4.4 shows the relationship between the platinum particle radius and current density at a cell voltage of 0.6 V. In may be observed that the performance of PEM fuel cells improves as the diameter of the platinum particles decreases. These results are consistent with those observed in other papers[105]. The optimal ORR activity and better performance can be obtained in the range of 2nm to 5nm. A more thorough and in-depth examination of the catalyst microstructure and its associated parameters can aid in enhancing the performance of PEM fuel cells. By reducing the size of platinum particles, it becomes possible to augment the number of reaction sites on the catalyst surface, resulting in a greater electrochemically active area.

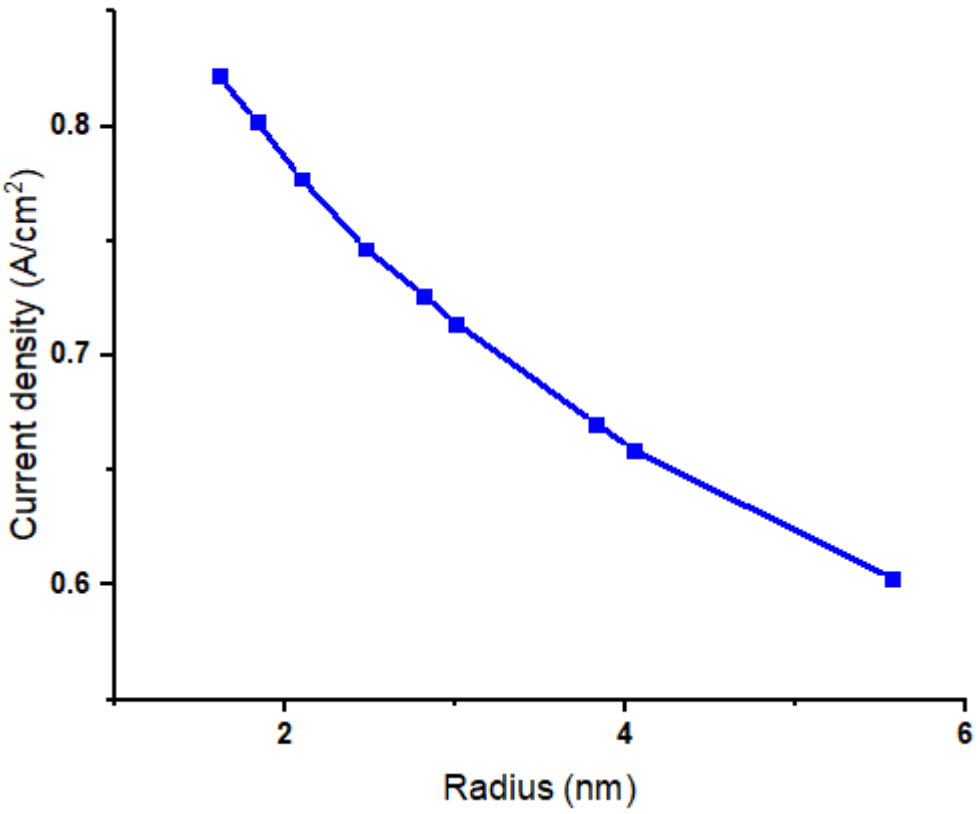

Figure 4.5 The effect of the Pt particle radius on the current density.

4.3.3 Electrochemical Active Area

Platinum particles must be ideally dispersed on the surface of the catalyst support (usually carbon powder) in order to increase the electrochemical reaction area. Additionally, these supports provide pathways for the transfer of mass, heat and charge. Further research on various carbon supports is required to identify candidates that boost the fuel cell performance. Figure 4.5 shows that as the electrochemical active area of the catalyst support increases, the performance of the PEM fuel cell can significantly improve.

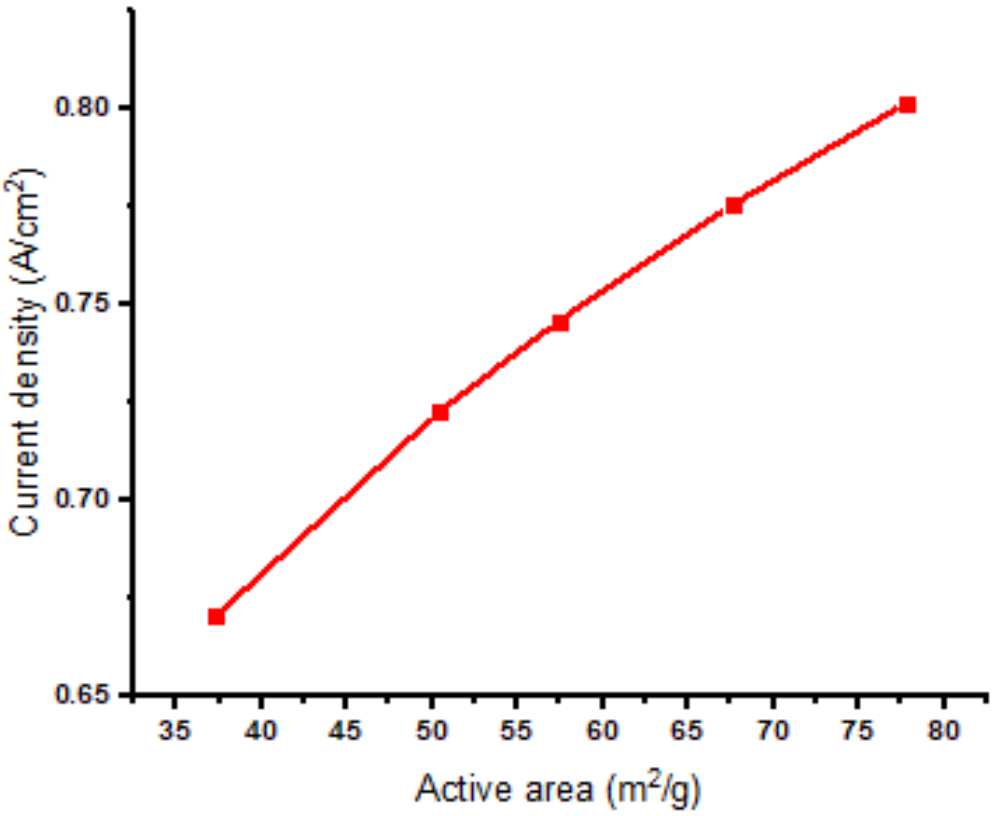

Figure 4.6 Current density (A/cm^2) for the various electrochemical active area(a_{ECSA}) at 0.6 V.

4.5 Conclusions

A three-dimensional numerical model has been created for a PEM fuel cell to conduct a parametric study investigating the effects of the catalyst layer microstructure. The initial results were found to be in excellent agreement with those reported in the literature. The key findings of the study may be summarised as follows:

1. Higher platinum loading and smaller platinum particle radius were found to improve the PEM fuel cell performance.
2. The electrochemical active area (a_{ECSA}) is an important parameter to consider when designing catalysts for PEM fuel cells. The results show that the larger is the value of the electrochemical active region, the better is the performance of the PEM fuel cell and this is due availability of more sites for the reaction. Higher electrochemical active area could be obtained through adjusting the structure of the catalyst.
3. The agglomerate model takes into account the microstructure of the catalyst, so it can more accurately simulate the operation and performance of PEM fuel cell. The homogeneous model ignores the microstructure of the catalyst, so it cannot accurately capture the consumption and production of oxygen and water, thus overestimating the performance of the fuel cell in the concentration loss region.

Chapter 5 Influence of catalyst agglomerate internal structure on PEFC performance investigated by a multiscale numerical model

5.1 Abstract

A multiscale modelling framework, which consists of a catalyst agglomerate scale and fuel scale models, has been developed for polymer electrolyte fuel cells (PEFCs). The agglomerate model's performance is connected to the fuel cell model using an interpolation function that encapsulates the agglomerate's behavior, such as provide reaction site, provide path for the reactants and water, more details is provided in the section on the microscale model of the catalyst agglomerate. This framework liberates the constraints imposed by conventional agglomerate PEFC models, enabling researchers to explore the catalyst agglomerate's structure and composition more flexibly. Consequently, the investigation delves into how the internal structure of the catalyst agglomerate affects fuel cell performance. The results have shown that the fuel cell performs better with catalyst agglomerates embodying “separate” active clusters and this impact becomes more profound as the size of the agglomerate increases. Also, it has been shown that the performance of the catalyst agglomerate becomes significantly better as the agglomerate size decreases. These outcomes and other outcomes have been presented and fully discussed.

Keywords: Polymer electrolyte fuel cells; Catalyst layer; Multiscale model; Agglomerate model

5.2 Introduction

Polymer electrolyte fuel cells (PEFCs) are promising power conversion technologies and this is due to their high efficiency (~ 50 %), low operating temperatures (typically between 20 and 80°C) and ease of construction [110], [111], [112], [113], [114], [115]. However, PEFCs experience some voltage losses that impact its widespread commercialisation, one of which is the activation voltage losses which are mainly caused by the slow kinetics of the oxygen reduction reaction taking place at the cathode electrode and the low utilisation of conventional platinum-based catalysts [116], [117], [118]. The catalyst layer comprises platinum, carbon black, and ionomers, forming a porous structure [119]. Evidently, there is a pressing need to optimize the utilization of precious platinum in Proton Exchange Membrane Fuel Cells (PEFCs) to simultaneously lower costs and maximize catalyst efficiency. Many researches have shown that increasing the specific area can maximise the utilisation of the catalyst and subsequently the fuel cell performance; this could be achieved by employing Nano-manufacturing methods [106], [120]. Optimising catalyst loading through only experimental means is costly and time-consuming. On the other hand, adopting mathematical modelling-aided experimentation saves a considerable amount of time and cost, especially when considering the increasingly improved accuracy of the numerical models [121],[122], [123], [124], [125].

There are two commonly used models for PEFC catalyst layers: (i) homogeneous and (ii) agglomerate models. In contrast, homogeneous models postulate that the catalyst layer functions as a porous medium composed of a consistent mixture of ionomers, platinum, and carbon, as depicted in prior studies [126],[127],[128],[129]. In addition, homogeneous models could resolve the spatial variation of the key variables within the catalyst layer. However, they do not capture the impact of the microstructure of the catalyst. On the other

hand, agglomerate models posit that the catalyst layer is composed of evenly dispersed spherical agglomerates coated with ionomers. These spherical agglomerates are made up of a blend of ionomers, carbon, and platinum, as demonstrated in previous research [130],[131],[132],[133],[134],[131]. The spherical agglomerate model enhances validity by realistically depicting catalyst layer structure and addressing reactant gas dissolution, but variations in accuracy may arise. Despite improved consistency with experimental results, limitations within the model may affect predictive accuracy, necessitating further research and validation. This structure overcomes the shortcomings of the homogenous model as it accounts for the dissolution of the reactant gas in the ionomer phase and reasonably captures the effects of the catalyst microstructure on the fuel cell performance. Many studies have shown that the simulation results of this agglomerate model are more consistent with the experimental results [128],[135],[136]. The agglomerate model was utilized to explore how the shape and size of catalyst agglomerates impact fuel cell performance. Jain et al. [130] proposed a two-dimensional model to analyse how the agglomerate's shape affects fuel cell performance, revealing that fuel cell performance is significantly influenced by agglomerate shape (spherical, plate-like or cylindrical) and that it is significantly enhanced when the size of the agglomerates is reduced.

Recently, only a limited number of multiscale PEFC models have been created, connecting the performance of catalyst agglomerates to fuel cell performance. These models offer flexibility, enabling researchers to explore the impacts of catalyst agglomerate composition, structure, and shape more freely. In other words, the user of the multiscale model is not limited to the three basic shapes (spherical, plate-like or cylindrical) as is the case in the conventional agglomerate model. What follows are the very few studies that have been performed on the multiscale PEFC models. Kamarajugadda and Mazumder [137] developed a flooded agglomerate model and subsequently coupled it with a two-dimensional fuel cell

model. This combination allowed them to examine how overlapping agglomerates and variations in agglomerate sizes could impact the performance of fuel cells.

Their investigation revealed that the agglomerate shape has minimal influence on fuel cell performance when the agglomerate size is small (e.g., 100 nm), but has a significant impact when the agglomerate size is large (e.g., 1000 nm) Moore et al. [138] established a multi-scale model that integrated a 1D catalyst agglomerate model with a 2D fuel cell model. Their investigation revealed that properties of the agglomerates, such as proton conductivity, presented a notable influence on the current density within the catalyst layer, consequently affecting the overall fuel cell performance. Ismail et al. [119] developed a multiscale model to study the impact of the catalyst agglomerate shape on the fuel cell performance. Firstly, the three-dimensional agglomerate model was solved, and then the results (in the form of volumetric current density as a function of the dissolved oxygen concentration and activation overpotential) were numerically coupled with a 1D fuel cell cathode model. According to their research, they discovered that fuel cell performance reaches its peak when using a cylindrical catalyst agglomerate. This enhanced performance can be attributed to the relatively larger specific surface area provided by this particular shape.

Notably, the above-mentioned multiscale PEFC models assumed that the active area, which consists of the catalysts and the ionomer, within the catalyst agglomerate is uniform. However, the micrographs of the catalyst layer shows that this is mostly not the case: the catalyst agglomerate consists of separate, contacting and/or overlapping active regions and non-active regions which mostly consist of the ionomer phase and/or pores [139][140][141]. Hence, this study aims to explore how the internal structure of the catalyst agglomerate impacts fuel cell performance. To achieve this goal, we've established a multiscale PEFC modelling framework. Within this framework, the performance of a three-dimensional agglomerate model is intricately connected to that of a one-dimensional PEFC model.

Additionally, we've examined how the modelling outcomes are influenced by variations in the size of the catalyst agglomerate.

5.3 Model description

To explore how the internal structure of the catalyst agglomerate affects PEFC performance, we've created two numerical models that vary in length scale. The first model focuses on the nanoscale/microscale catalyst agglomerate (shown on the right in Figure 5.1), while the second model is a macroscale PEFC model (shown on the left in Figure 5.1). These models are interconnected to examine how the catalyst agglomerate's internal structure impacts fuel cell performance [142]. The following two subsections describe each model and detail the governing equations for each one. In the micro-scale model the realistic data sets for the oxygen concentration(C_{O_2})and over-potential(η)for the agglomerate model, then it will be solve repeatedly the average current density will be computed under all conditions(C_{O_2} , η). Then the average current density will be used in the macro scale model to compute the local current density.

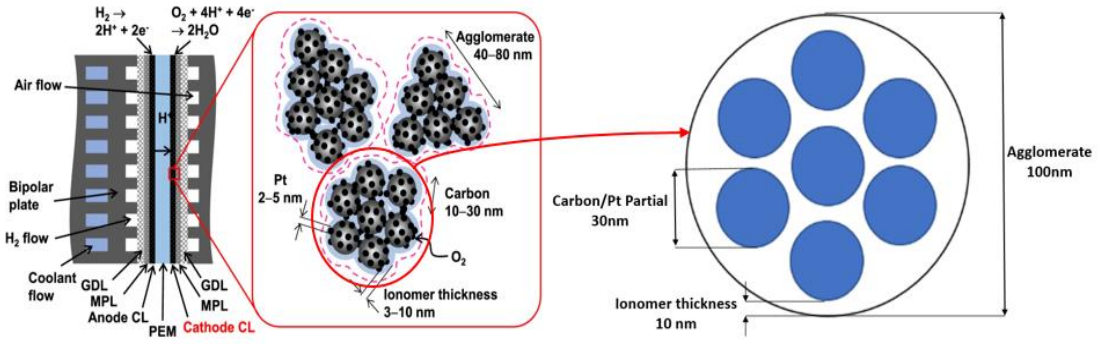

Figure 5.1 Schematic presentation of the multi-scale structure of the catalyst layer [141]**.**

5.3.1 Microscale model of the catalyst agglomerate

Consulting Figure 5.1 and other related micrographs [143], [144], [145], in this study, the catalyst agglomerate is assumed to be spherical and composed of spherical active clusters interspersed with non-active regions. These active clusters, depicted in red in Figure 5.2, are assumed to comprise a consistent catalyst blend (specifically, platinum carried by carbon particles, filled with pores and ionomer) while the non-active region (grey areas in Figure 5.2) was assumed to be ionomer and pore. For simplicity, the active clusters are assumed to be identical, and they are either: (i) separate from each other, (ii) contacting each other or (iii) overlapping with each other; see Figure 5.2. Note that the catalyst agglomerate may contain more than one internal structure; it may contain for example "separate" and "contacting" active clusters. However, for simplicity and to meet the objective of this study, which is to show the impact of ignoring the internal structure of the catalyst agglomerate, the cases investigated were limited to the above "simplified" structures. In all the structures, the minimum distance between the active clusters and the outer surface of the agglomerate was assumed to be one tenth of the radius of the agglomerate; for example, if the radius of the agglomerate is 100 nm, then this distance is 10 nm [119]. It's important to mention that, because the geometry is rotational symmetry, for the sake of computational efficiency, only one eighth of the catalyst agglomerate was taken into consideration.

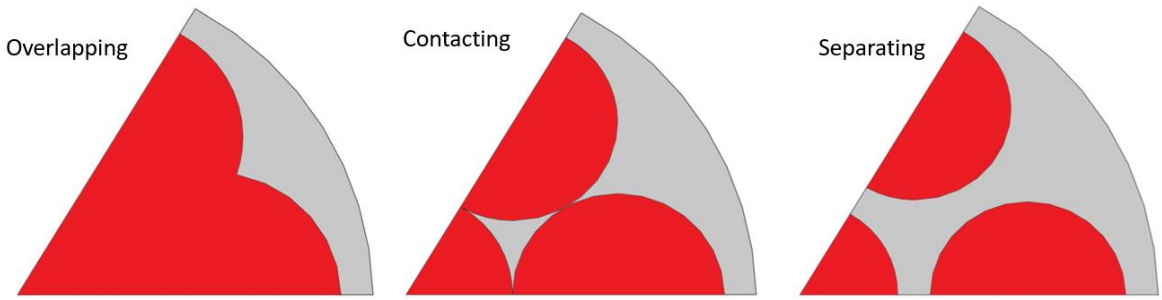

Figure 5.2 A schematic of the internal structure of the agglomerate.

The following are the equations used to simulate the physics in the catalyst agglomerate. The reactant gas (i.e. oxygen in this case) is realistically assumed to be transported within the agglomerate by diffusion and reacts in the active clusters of the agglomerate [146]:

$$\nabla D_e^{eff} \nabla C_{O_2} - R_{exn,O_2} = 0 \tag{5.1}$$

In this equation, C_{O_2} stands for the molar concentration of dissolved oxygen, while ∇D_e^{eff} represents the effective diffusivity of dissolved oxygen within the ionomer phase. This effective diffusivity is determined using the Bruggeman correlation [26]:

$$D_e^{eff} = \begin{cases} D_e & \text{in the non-active region} \\ \varepsilon_e^{1.5} D_e & \text{in the active clusters} \end{cases} \tag{5.2}$$

where, D_e signifies the diffusivity of dissolved oxygen within the ionomer, while ε_e represents the volume fraction of the ionomer phase within the active region. Additionally, R_{exn,O_2} denotes the molar consumption of oxygen:

$$R_{exn,O_2} = \begin{cases} 0 & \text{in the non-active region} \\ kC_{O_2} & \text{in the active clusters} \end{cases} \tag{5.3}$$

$$k = \frac{i_0 a}{4F C_{O_2}^{ref}} \exp\left(\frac{-\alpha F}{RT}\eta\right) \tag{5.4}$$

In this equation, k represents the reaction rate constant, i_0 denotes the exchange current density, F stands for Faraday's constant, $C_{O_2}^{ref}$ signifies the reference concentration of dissolved oxygen, α is the charge coefficient, T represents temperature, R corresponds to the

universal gas constant, η represents the activation over-potential (an essential input variable for the model), and a denotes the specific surface area of the catalyst [108]:

$$a = \frac{l_{pt} A_{pt}}{L_{cl}} \tag{5.5}$$

In this equation, l_{pt} stands for platinum loading, electrochemical surface area of the platinum catalyst defined as A_{pt}, and the thickness of the catalyst layer is L_{cl}. Faraday's law is employed to calculate the average current density of the agglomerate $\overline{I_{agg}}$:

$$\overline{I_{agg}} = 4Fk\overline{C_{O_2}} \tag{5.6}$$

where $\overline{C_{O_2}}$ is the average concentration in the active clusters. Equation (4.1) is solved using boundary conditions which presented in Figure 5.3. Constant dissolved oxygen concentration ($C_{O_2,o}$) is used for the surface of the agglomerate and zero flux of the dissolved oxygen concentration (∇C_{O_2}=0) is used for the symmetrical lines in the computational domain.

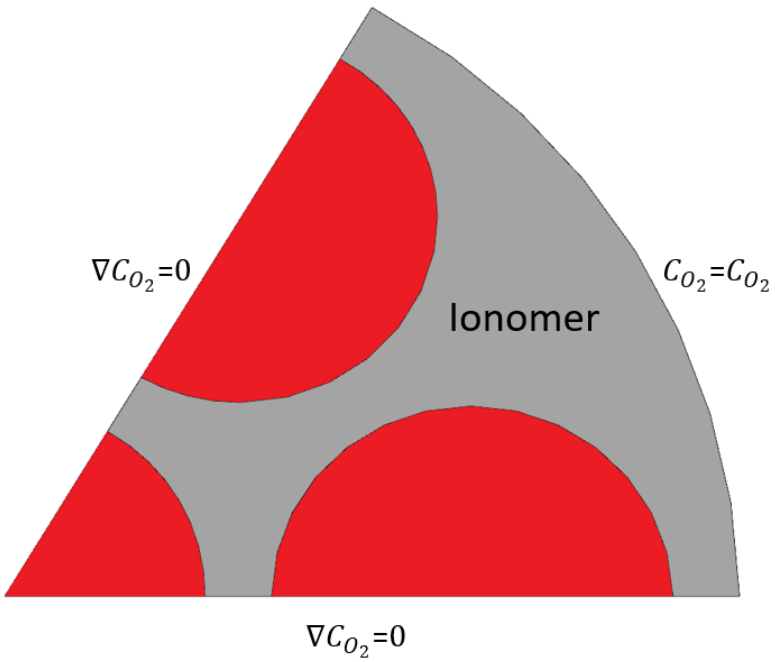

Figure 5.3 The boundary conditions for the agglomerate model.

In order to solve Equation (5.1), COMSOL Multiphysics 6.0 was used and the iterative linear solver GMRES (Generalised Minimum Residual) was applied. A mesh independence study was performed. Namely, the maximum mesh size was decreased from 0.003 to 0.0003 µm and the average current density was found to change by less than 1%. Hence, the mesh with a maximum mesh size of 0.003 µm was used. For this mesh, the number of elements was found to be around 110 K; Figure 5.4 shows a meshed 2D cut of the modelled catalyst agglomerate with separate active clusters. The computational time required for generating the mesh and solving the model was, using an Intel Xeon 3.80 GHz processor, about 60 minutes.

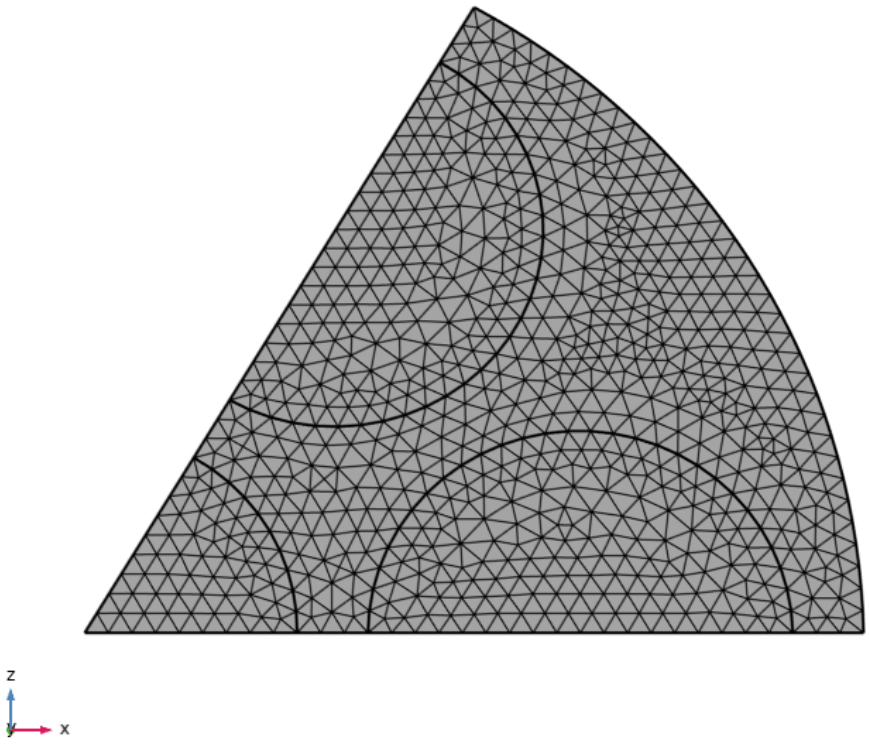

Figure 5.4 A 2D meshed cut of the modelled catalyst agglomerate.

5.3.2 Macroscale PEFC model

Figure 5.5 provides a schematic representation of boundary conditions that employed in the one-dimensional PEFC model (these boundary conditions will be discussed further in this section's conclusion). For simplicity, the fuel cell is assumed operates under isothermal and low-humidity conditions, thus allowing the isolation of thermal and saturation effects. Consequently, the model exclusively incorporates the conservation equations for chemical species and charge. The following sections outline the governing equations employed in this model.

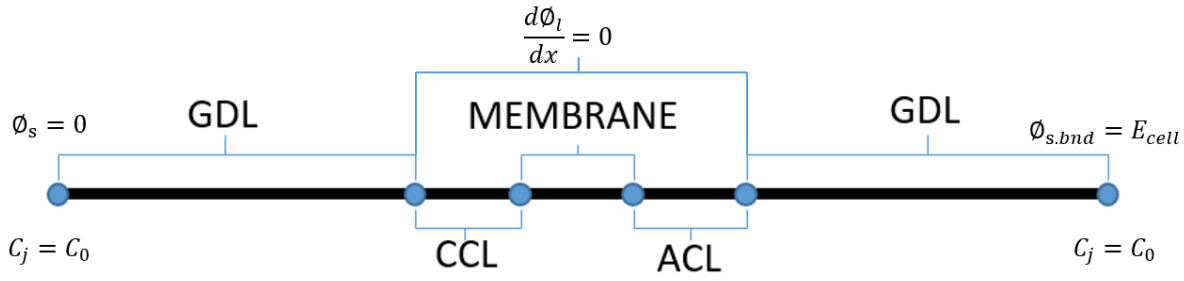

Figure 5.5 A schematic demonstration of the boundary conditions used in the 1-D PEFC model.

The continuity equation is given by:

$$\nabla \cdot (\rho \vec{u}) = 0 \tag{5.7}$$

where $\vec{u}$ is the velocity vector and ρ is the density of the gaseous mixture. The conservation of species equations is obtained using the following equation:

$$\rho(\vec{u} \cdot \nabla) = -\nabla(j_i) + R_i \tag{5.8}$$

where j_i is the mass flux relative to the mass averaged velocity of species i, and R_i is the source term representing the production or consumption rate. j_i is defined as follows [119]:

$$j_i = -\rho\omega_i \sum_k D_{ik}^{eff} \frac{M}{M_k} (\nabla\omega_k + \omega_k \frac{\nabla M}{M}) \tag{5.9}$$

where ω_i is the mass fraction of the species i, $D_{ik,eff}$ is the effective diffusivity of the chemical species i (e.g. oxygen) into the chemical species k (e.g. nitrogen). For ideal gas mixtures, the density is given by:

$$\rho = \frac{pM}{RT} \tag{5.10}$$

where p is the absolute pressure. The molecular weight of the gas mixture, M, is given by:

$$M = \sum \chi_i M_i \tag{5.11}$$

where χ_i and M_i are the mole fraction and the molar mass of the chemical species i, respectively. $D_{ik,eff}$ in the GDL or the catalyst layer (CL) is calculated by:

$$D_{ik,eff} = \begin{cases} 0.008e^{4.81\varepsilon} D_{ik} & in\ the\ GDLs \\ \varepsilon^{1.5} D_{ik} & in\ the\ CLs \end{cases} \tag{5.12}$$

where ε is the porosity. The source term R_i shown in Equation (5.8) is given by:

$$R_i = \frac{I}{nF} \tag{5.13}$$

where n is the number of electrons transferred in the reaction (4 for oxygen and 2 for hydrogen and water), by solving the agglomerate model, the volumetric current density I can be obtained and presented subsequently. Water vapor calculations are conducted through the following equation:

$$S_{H_2o} = 2R_i + nd\nabla \cdot i/F \tag{5.14}$$

where nd is the drag coefficient. The conservation of charge equations are given by:

$$\nabla(-\sigma_s \nabla \phi_s) = \nabla \cdot i \tag{5.15}$$

$$\nabla(-\sigma_l \nabla \phi_l) = -\nabla \cdot i \tag{5.16}$$

where σ_s and σ_l are the electrical conductivity and the ionic conductivity of the solid phase and ionomer phase, respectively, and ϕ_s and ϕ_l are the solid-phase and the ionomer-phase potentials, respectively. Note that Equation (5.15) is applicable to the GDLs and the CLs while Equation (5.16) is applicable to the CL and the membrane electrolyte. The local activation over-potential η in the cathode catalyst layer, η_c,is given by:

$$\eta_c = \phi_s - \phi_l - E_{eq} \tag{5.17}$$

Nernst equation is used to calculate E_{eq}, which stands for the theoretical cell potential [146] and found to be 1.221V. The local activation over-potential in the anode catalyst layer, η_a, is given by:

$$\eta_a = \phi_s - \phi_l \tag{5.18}$$

The local volumetric current density within the cathode catalyst layer, I_c, is computed using the following equation [119]:

$$I_c = \overline{I_{agg}}(1 - \varepsilon_{cl}) \tag{5.19}$$

where $\overline{I_{agg}}$ is the average volumetric current density of the modelled agglomerate which is obtained using Equation (5.6) and ε_{cl} is the porosity of the catalyst layer. Note that I_c changes with cathode activation overpotential and concentration of dissolved oxygen;

therefore, $\overline{I_{agg}}$ is repeatedly solved for using a realistic set of cathode activation overpotential (ranging between -0.1 and -1 V) and concentration of dissolved oxygen (ranging between 0 and 0.86 mol/m³) [9]. Then the average volume current density $\overline{I_{agg}}$ is used to calculate I_c by employing a interpolation function; Figure 5.6 shows a typical interpolation function for the agglomerate volumetric current density. On the other hand, the anodic local volumetric current density, I_a, is obtained using the following conventional form of Butler-Volmer equation:

$$I_a = i_o a \left(exp\left(\frac{\alpha_a F \eta_a}{RT}\right) - exp\left(\frac{-\alpha_c F \eta_a}{RT}\right)\right) \tag{5.20}$$

where i_o is the reference exchange current density of a unit active surface area, a is the specific surface area, which is calculated by Equation (5.5), α_a and α_c are the anodic and cathodic charge transfer coefficients and η_a is the anodic activation overpotential which is calculate by Equation (5.18). At a defined cell potential, calculate the local cathodic or anodic volumetric current density are calculated by averaging it across the length of the catalyst layer. This averaged value is then multiplied by the layer's length to obtain a data point on the polarization curve. Figure 5.5 illustrates the boundary conditions utilized to solve the model. Specifically, concentration boundary conditions have been defined for both the left and right sides of the computational domain, while solid-phase potential has been set at both ends of the computational domain.; the solid-phase potential was defined at both side of the domain, it equals the cell potential at the outermost point of the cathode GDL and equals zero at the outermost point of the anode GDL. On the other hand, zero-flux ionomer-phase boundary conditions were used at the outermost points of the catalyst layers. The governing equations (5.7), (5.8), (5.15) and (5.16) were solved using COMSOL Multiphysics® 6.0. The solver employed for this task was MUMPS, which is a sparsely direct and massively parallel linear system solver. The domain was discretised, the

computational domain of the interface between the catalyst layer and the GDL is refined and the mesh independent should be obtained. The maximum mesh size was established at 0.012 μm, the maximum mesh growth rate is set to be 1.2. The mesh, which was deemed solution-independent, comprised roughly 125 elements. Table 5.1 presents the parameters utilized for solving both the agglomerate scale and the fuel cell scale models.

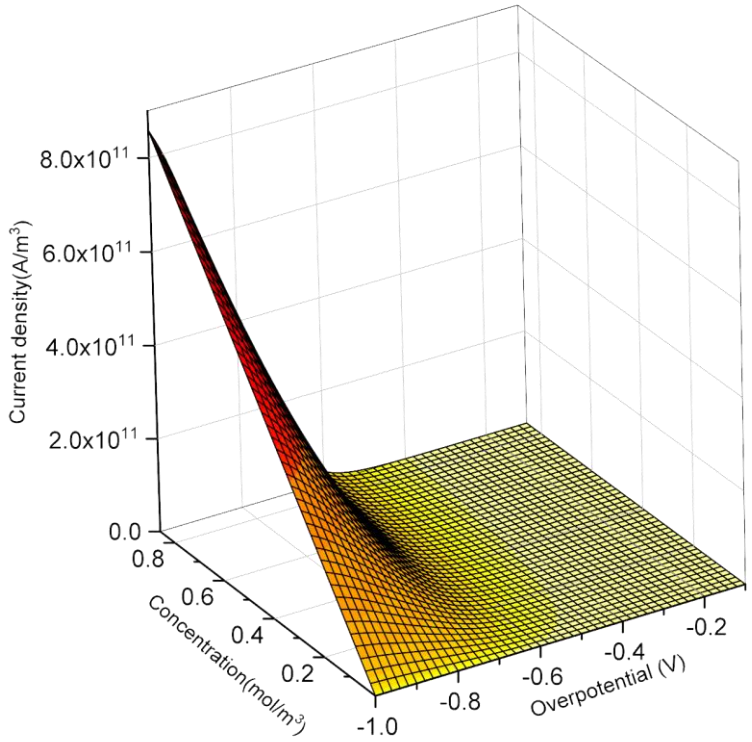

Figure 5.6 A typical plot for the interpolation plot of volumetric current density as a function of dissolved oxygen concentration and activation overpotential for a modelled agglomerate with 100 nm radius and separate active clusters.

Table 5.1 The parameters used in the agglomerate scale and the fuel cell scale models [119], [146], [147]

Parameter	value
Thickness of membrane (L_{mem})	30um
Thickness of catalyst layer (L_{cl})	15um
Thickness of GDL (L_{GDL})	250um
Cathode charge transfer coefficient (α_a)	3.39
Pressure (p)	1.5atm
Temperature (T)	353K
Faradays' constant (F)	96485Cmol^{-1}
Universal gas constant (R)	$8.314\text{mol}^{-1}\text{K}^{-1}$
Henry's constant	31664 $\text{Pa}\cdot\text{m}^3\text{mol}^{-1}$
Electrochemical active area of platinum particles (A_{pt})	$40\text{m}^2\text{g}^{-1}$ [147]
Platinum loading (l_{pt})	0.4mgcm^{-2}
Anode Exchange current density ($i_{0,a}$)	100Am^{-2}

Cathode Exchange current density ($i_{0,c}$)	0.015Am^{-2}
Reference dissolved O_2 concentration ($c_{O_2}^{ref}$)	0.85molm^{-3}
Porosity of anode/cathode CL (ε_{cl})	0.48
Porosity of anode/cathode GDL (ε)	0.6
Ionomer volume fraction in the agglomerate (ε_e)	0.5
Oxygen diffusivity in the ionomer (D_{e})	8.45×10^{-10} m$^2/s$ [146]
Oxygen in nitrogen diffusivity ($D_{O_2-N_2}$)	1.86×10^{-5} m$^2/s$ [146]
Oxygen in Water vapour diffusivity ($D_{O_2-H_2o}$)	2.47×10^{-5} m$^2/s$ [146]
Water vapour in nitrogen diffusivity ($D_{H_2o-N_2}$)	2.58×10^{-5} m$^2/s$ [146]
Electric conductivity of gas diffusion layer (σ_{GDL})	100 S/m
Electric conductivity of electrolyte σ_m	0.85 S/m
Electric conductivity of catalyst layer (σ_{CL})	30 S/m

a: proton conductivity is calculated by using Springer model

5.4 Results and discussion

5.4.1 Validation of the multi-scale model

To validate the current multi-scale model, it is essential to compare the output from this modeling framework, represented as a polarisation curve, with the corresponding output produced by the conventional model. For the conventional model, the agglomerate influence is analytically coupled with the fuel cell model. Assuming spherical agglomerates, the cathodic current density used in the verification is given by [137], [138]:

$$\nabla \cdot i_c = 4F(1-\varepsilon_{cl})C_{O_2,o}\frac{{r_{agg}}^3}{\left(r_{agg}+\delta_{agg}\right)^3}\left(\frac{1}{E_r k}+\frac{r_{agg}\delta_{agg}}{a_{agg}(r_{agg}+\delta_{agg})D_e}\right)^{-1} \quad (5.21)$$

In this equation, $C_{O_2,o}$ refers to the defined dissolved oxygen concentration at the surface of the ionomer film, which can be computed using the following expression:

$$C_{O_2,o} = \frac{C_{O_2,g}RT}{H} \quad (5.22)$$

In the equation, $C_{O_2,g}$ represents the concentration of oxygen in the gas phase before it dissolves into the ionomer film's surface, and H stands for Harry's constant. The specific surface area of the spherical agglomerate, denoted as a_{agg}, is determined by the following expression [20]:

$$a_{agg} = \frac{3}{r_{agg}} \quad (5.23)$$

In this validation case, where the agglomerate radius r_{agg} is set to 100 nm, the effectiveness factor E_r of the spherical agglomerate used in Equation (5.21) is defined as follows[148], [146]:

$$E_r = \frac{1}{\Phi_L}\left(\frac{1}{\tanh(3\Phi_L)} - \frac{1}{3\Phi_L}\right) \tag{5.24}$$

where Φ_L is the Thiele modulus which is given by:

$$\Phi_L = \frac{r_{agg}}{3}\sqrt{\frac{k}{D_e^{eff}}} \tag{5.25}$$

Figure 5.7 shows that the polarisation curves as generated by: (i) the present multiscale modelling framework for the case in which the core of the agglomerate is assumed to be wholly chemically active and uniform (see Figure 5.1) and (ii) the conventional agglomerate model (represented by Equations (5.21-5.25)). The figure illustrates a high degree of agreement between the two generated polarisation curves, instilling confidence in the precision of the predictions made by the multi-scale model developed in this study.

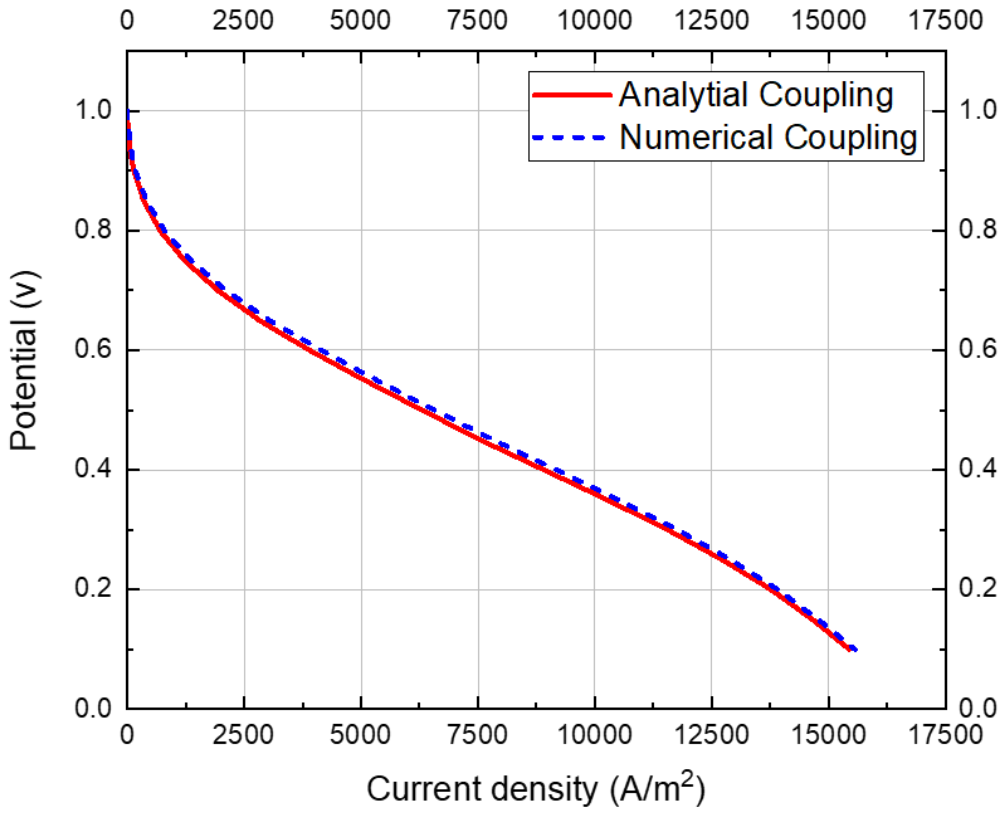

Figure 5.7 The polarisation curve of the multi-scale model (blue line) and analytical model (red line).

5.4.2 Effect of the size and internal structure on the agglomerate current density

Figure 5.8 shows the performance curves obtained from the agglomerate scale models for the agglomerate with different sizes (100 and 1000 nm) and internal structure ("separate", "contacting" and "overlapping"). The first observation is that the catalyst agglomerate performs better with decreasing size. For example, for the agglomerate with "separate" internal structure, the average volumetric current density increases by two orders of magnitude when decreasing the agglomerate radius from 1000 nm to 100 nm. This could be attributed to better catalyst utilisation as demonstrated by the smaller agglomerates. In other

words, the reactant gas (which is oxygen in this case) is largely consumed as soon as it enters the active clusters in the agglomerate (particularly at high overpotential values) which means that most of the active region remains largely non-utilised (see Figure 5.9); this phenomenon becomes more profound with larger catalyst agglomerates and leads to less volumetric current density by larger agglomerates.

The second observation is that, regardless of the agglomerate size, the agglomerates with separate active clusters perform better than the agglomerates with contacting active clusters and these agglomerates in turn perform better than those with overlapping active clusters. This phenomenon can be explained by the observation that agglomerates featuring separate active clusters have the maximum total surface area, while those with overlapping active clusters have the minimum. As the surface area of the agglomerate's active region increases, the catalyst utilization becomes increasingly efficient. As explained in Section 5.2, the graphs shown in Figure 5.8 were used as interpolation functions for the PEFC scale model.

100nm **1000nm**

(a)separate

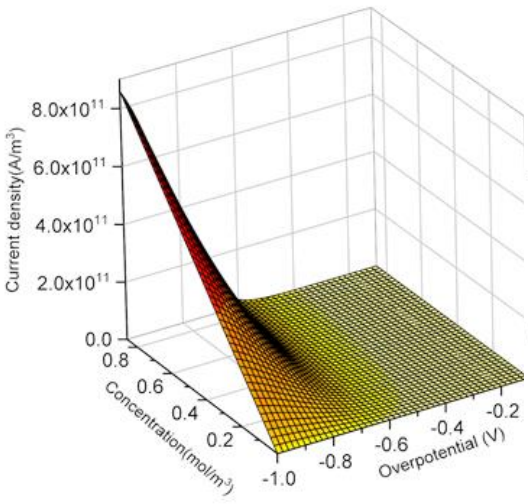

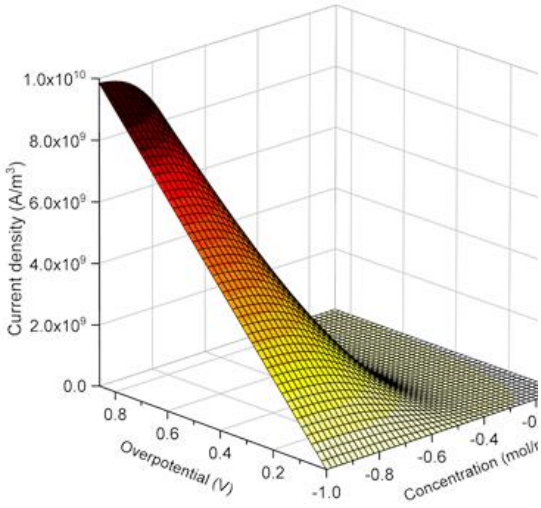

(b)Conating

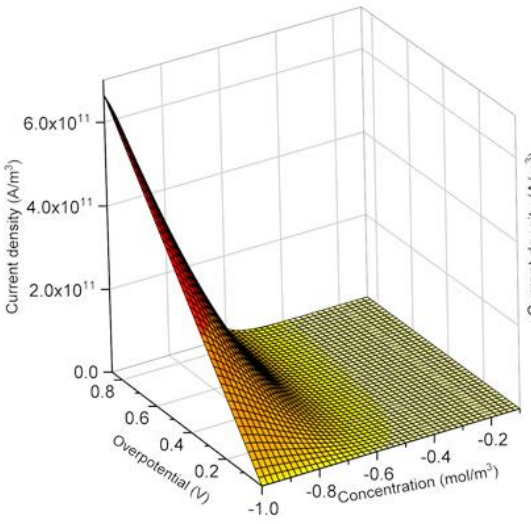

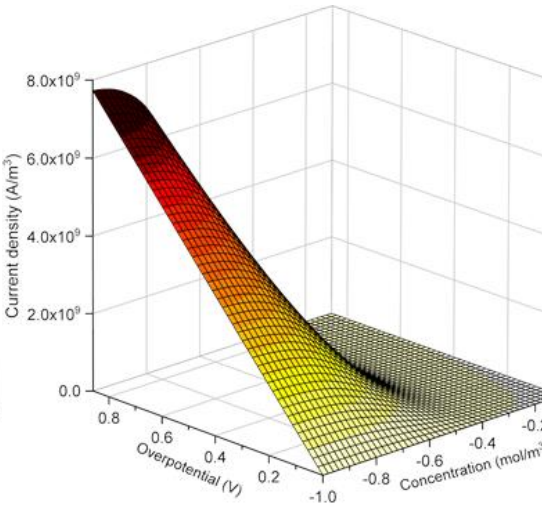

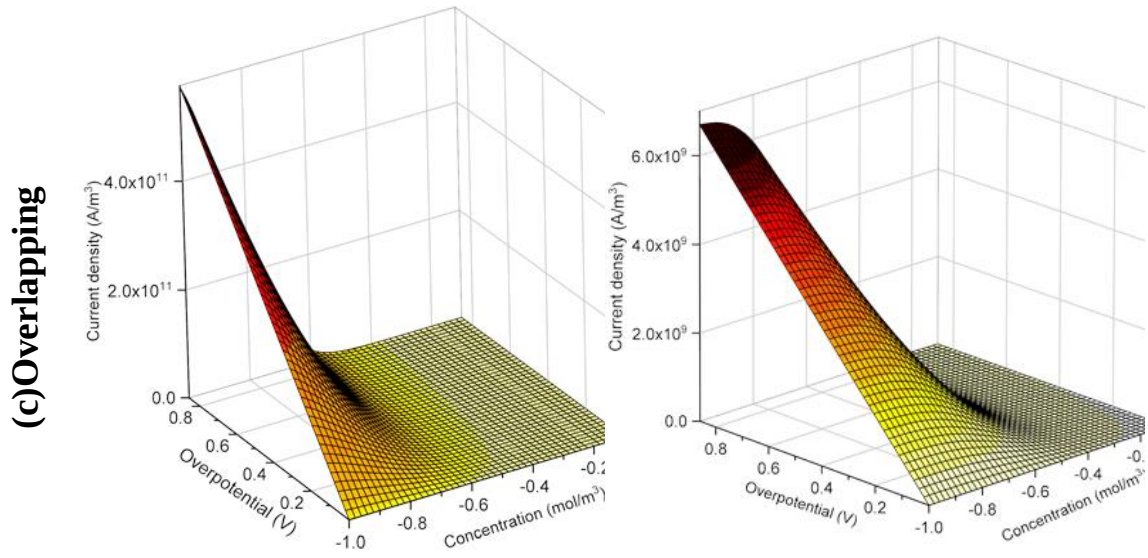

Figure 5.8 The functional relation of the over potential and oxygen concentration and current density of the agglomerate with different internal structure and different radius.

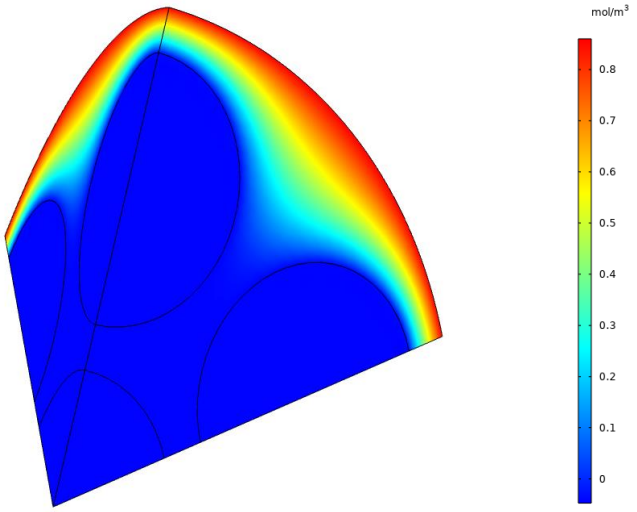

Figure 5.9 The distribution of dissolved oxygen concentration at an activation overpotential of -1 within the modelled section of the catalyst agglomerate with 100 nm radius.

5.4.3 Effect of the agglomerate internal structure and size on the PEFC performance

In Figure 5.10, presents the polarisation curves of the simulated PEFC operating with catalyst agglomerates of two distinct sizes (100 and 1000 nm) and featuring three distinct internal structures (separate, contacting, and overlapping active clusters). It's worth noting that, in general, the fuel cell exhibits superior performance when employing separate active clusters. This notable improvement can be attributed to the larger specific surface area presented by these isolated active clusters in comparison to the other two configurations. The second note is that the impact of the internal structure on the fuel cell performance becomes more significant when reducing the radius of the agglomerate from 1000 to 100 nm see Figure 5.11. For example, for the smaller agglomerates, the maximum currant density with separate active clusters is larger than that with contacting active clusters by less than 1 %. On the other hand, for the larger agglomerates, the maximum currant density with separate active clusters is larger than that with contacting active clusters by more than 12 %. These outcomes can be attributed to the greater diffusion pathways, and consequently, increased mass transport resistance associated with larger catalyst agglomerates when compared to their smaller counterparts. This phenomenon results in the fuel cell's heightened responsiveness to alterations in internal structures, particularly in the high current density range where mass transport limitations become more pronounced. This observed sensitivity of fuel cell performance to agglomerate size aligns with findings previously reported by Ismail et al. [119] and Kamarajugadda et al. [137].

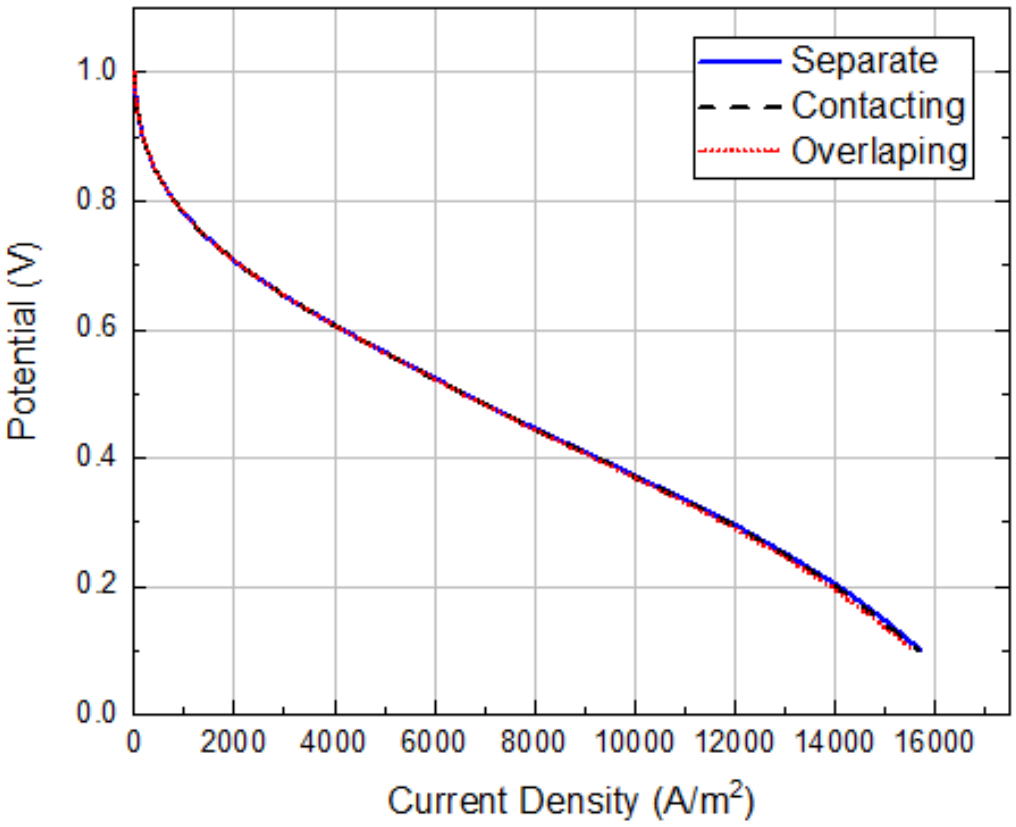

Figure 5.10 The polarisation curve of the multiscale modelling with 0.1 um radius agglomerate and a different internal structure.

These outcomes can be attributed to the greater diffusion pathways, and consequently, increased mass transport resistance associated with larger catalyst agglomerates when compared to their smaller counterparts. This phenomenon results in the fuel cell's heightened responsiveness to alterations in internal structures, particularly in the high current density range where mass transport limitations become more pronounced. This observed sensitivity of fuel cell performance to agglomerate size aligns with findings previously reported by Ismail [119].

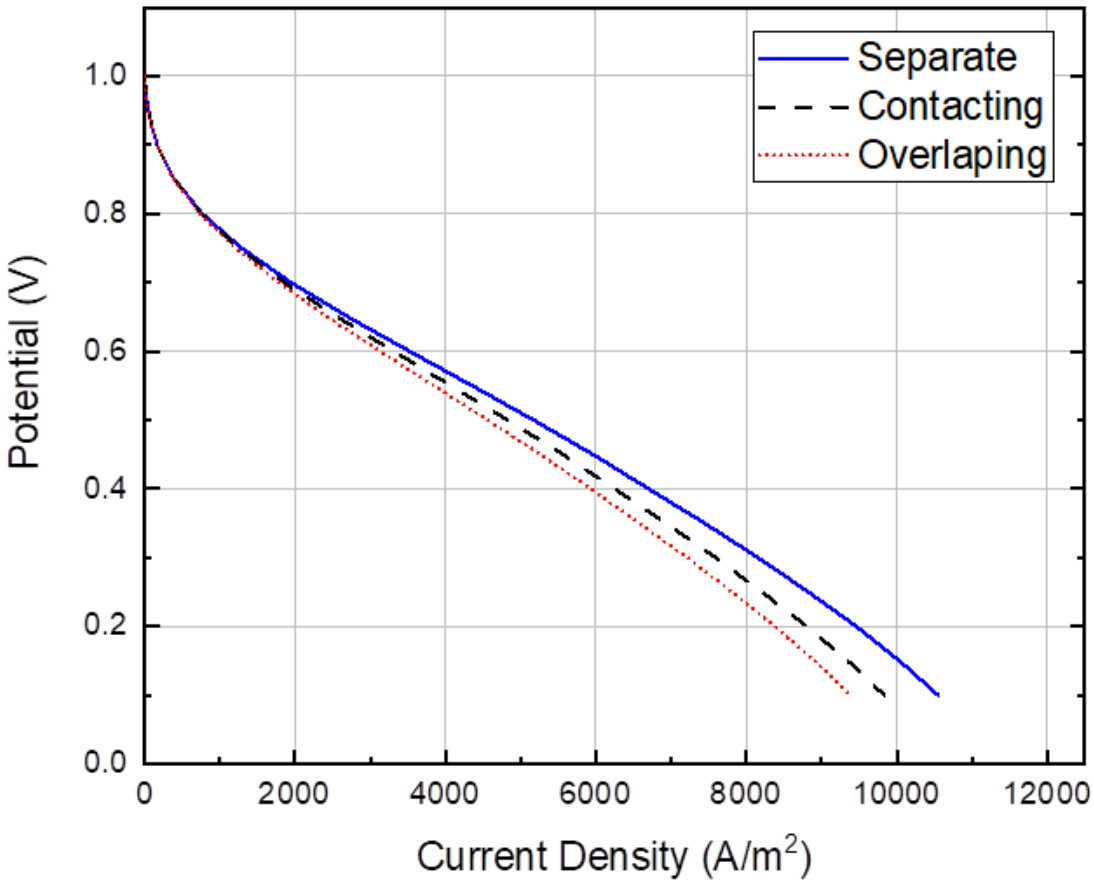

Figure 5.11 The polarisation curve of the multiscale modelling with 1 um radius agglomerate and different internal structure.

It is worth noting that the agglomerates with separate active clusters do not only improve the fuel cell performance but also reduce the amount of platinum catalyst. Namely, the total active volume of the agglomerate with separate active clusters is less than those with contacting and overlapping active clusters by around 20 and 45 %, respectively; this evidently means that significantly less platinum catalyst is used when employing agglomerates with separate active clusters.

5.5 Conclusion

A comprehensive multiscale modeling framework for the Proton Exchange Membrane Fuel Cells (PEFCs) has been developed. This framework comprises two integral components: a

catalyst agglomerate scale model and a fuel cell scale model. Initially, the agglomerate model is solved to generate a performance plot, which illustrates the average volumetric current density variations concerning dissolved oxygen concentration and activation overpotential. This performance plot serves as an interpolation function, seamlessly connecting it to the fuel cell scale model. By doing so, local current density profiles within the cathode catalyst layer for a given cell potential can be generated. This innovative modeling framework has been instrumental in our investigation into how the internal structure of the catalyst agglomerate influences fuel cell performance. To simplify the analysis, only three scenarios were considered for the arrangement of active clusters within the agglomerate: separate clusters, clusters in contact with each other, and overlapping clusters. The following are the key findings derived from these investigations:

i. The fuel cell performs better with catalyst agglomerates featuring “separate” active clusters than those feature “contacting” or “overlapping” clusters and this is due to higher specific surface area demonstrated by the separate active clusters.
ii. This impact (i.e. the impact of the internal structure of the agglomerate on the fuel cell performance) becomes more profound as the size of the agglomerate increases. It was shown that the maximum current density with “separate” active clusters is larger than that with “contacting” active clusters by more than 12% and this is because the fuel cell becomes more mass transport resistance limited with larger agglomerates.
iii. The modelled agglomerate perform better with decreasing size. The volumetric current density was found to increase by two order of magnitude when catalyst agglomerate size decreases from 1000 nm to 100 nm. This is attributed to better catalyst utilisation of the smaller agglomerates.
iv. Considering the current and future advancements in the nano- and micro-fabrication technologies, it is recommended to design catalyst agglomerates with “separate” active clusters as they improve the fuel cell performance and also reduce the catalyst loading.

Chapter 6 Influence of the agglomerate shape of catalyst on the PEM fuel cell performance investigated by a multiscale model

6.1 Abstract

This chapter thoroughly investigates the impact of agglomerate shapes in the catalyst layer of a PEM fuel cell on its overall performance, presenting a novel multiscale model. Traditional models commonly assume a uniformly spherical catalyst layer, whereas micrographs reveal that agglomerates come in various shapes. In contrast, this model numerically integrates the effects of agglomerate microstructure at the scale of the PEM fuel cell. The key assumption is that agglomerates can take any form, with particular focus on spherical, cubic, polyhedral, cylindrical, and ellipsoidal shapes in this study. Initially, the model solves for the agglomerate-scale behaviour, extracting reactant concentrations and current density. These values are then applied to the fuel cell-scale model, yielding the performance curves. Consequently, researchers gain the freedom to explore diverse agglomerate shapes, unrestricted by the limitations of traditional uniform models. The findings indicate that larger agglomerates (radius ≥ 1000 nm) have a more pronounced influence on fuel cell performance, and when agglomerates adopt an ellipsoidal shape, the maximum current density increases by approximately 28%. Furthermore, this study establishes a significant correlation between agglomerate shape and fuel cell performance.

Keywords: Multi-scale model, Agglomerate model, Catalyst layer, PEFCs

6.2 Introduction

Proton Exchange Membrane Fuel Cells (PEMFC) have garnered considerable attention due to their remarkable efficiency, environmental friendliness, and emission-free characteristics as power generation devices [149],[150],[151],[152],[114]. Nonetheless, the commercialization of PEMFC faces impediments owing to the substantial cost of the catalyst employed in the electrochemical process [106]. Currently, platinum (Pt) stands as the predominant catalyst material utilized in low-temperature fuel cells[135]. Although researchers have made notable strides in mitigating platinum loading through alloying with other metals, this strategy presents inherent challenges pertaining to the catalyst's stability and durability[153]. An alternative avenue emerges for cutting the platinum loading: the optimization of the catalyst structure. Such optimization holds the promise of significantly augmenting the catalyst's specific surface area, thereby inducing a more homogenous dispersion of platinum particles and ultimately leading to a substantial enhancement in the utilization efficiency[154],[119].

Controlling the shape and structure of the agglomerate can reduce the cost of catalysts and enhance their performance[155],[156]. Agglomerates with a high surface area are highly favorable for catalytic performance. Numerous reports have shown that controlling the shape of catalyst aggregates can improve the electrochemical activity of the catalysts[157]. These structurally engineered carriers can lead to a more uniform distribution of platinum nanoparticles on the agglomerate and increase the efficiency of reactant transport[158],[159]. While these experiments are very helpful in finding the optimal catalyst structure, they are often extremely expensive and time-consuming. Therefore, it is highly necessary and important to use more efficient and cost-effective methods such as computational models to search for the best catalyst structure[160].

Currently, the most widely employed structure for conventional commercial catalysts is typically believed to consist of aggregates composed of platinum and carbon. Abundant micrographs depict these agglomerates as having a semi-spherical shape[142]. In previous simulations, the most common models used were the homogeneous model and the aggregate model. The homogeneous model assumes that the catalyst layer is a porous material composed of platinum, carbon, and aggregates uniformly distributed in all directions[161],[162],[163]. While this structure can be used to predict the impact of the catalyst layer configuration on fuel cell performance, and it cannot be employed to investigate the influence of the actual microscopic structure within the catalyst layer on performance. Another frequently used model is the agglomerate model, which assumes that the aggregates are spherical and covered by a thin layer of ionomer [148],[132],[134]. While this model is closer to reality than the homogeneous model, it lacks the flexibility to effectively study the impact of aggregate shape on fuel cell performance.

To investigate the influence of the microscopic structure of the catalyst layer on fuel cell performance, it is necessary to construct a multiscale model that examines the impact of microstructures at the agglomerate scale on the fuel cell performance. This model comprises two components: the agglomerate scale and the fuel cell scale. Multiscale models for studying catalyst structure in this manner are not widely reported. Kamarajugadda and Mazumder [164] developed a generalized flooded agglomerate model to study the effect of overlapping unequal-radius spherical aggregates on fuel cell performance. Their research revealed that overlapping aggregates perform better than single agglomerate of the same volume. Hussain et al. [165] developed a three-dimensional numerical model for ordered-structure cathode catalyst layers to investigate the impact of structural parameters on fuel cell performance. The study demonstrated a significant effect of the spacing between carbon nanotubes (CNTs) on reactant transfer. Liang et al. [166] developed a cross-dimensional

model to study oxygen transport, exploring oxygen transport behavior under different structural parameters and operating conditions.

The aim of this study is to investigate the impact of catalyst agglomerate shape on the fuel cell performance. To accomplish this goal, a multi-scale modeling framework for Polymer Electrolyte Fuel Cells (PEFC) has been devised. Within this multi-scale model, the performance of a three-dimensional agglomerate model is intricately connected to that of a one-dimensional PEFC model. Furthermore, an exploration of the modeling framework's sensitivity to the size of the catalyst agglomerate has been conducted.

6.3 Model description

In this study, it was aimed to investigate the impact of catalyst agglomerate shape on the performance of Polymer Electrolyte Fuel Cells (PEFC). To achieve this, two numerical models of different scales were developed, thus creating a robust multiscale approach. The first part involved establishing a model at the agglomerate scale, thus enabling the current density under varying concentrations and overpotentials through iterative solutions to be obtained. This provided valuable insights into the behaviour of the catalyst agglomerate under different conditions. In the second part, the integration of the agglomerate-scale model with the fuel cell-scale model was achieved. By doing so, this could thoroughly examine how the agglomerate's shape influences the overall performance of the fuel cell. This approach allowed one to gain a deeper understanding of the complex interactions occurring at different scale within the PEFC system. Overall, this research provides valuable knowledge for optimizing the design and performance of PEFCs by considering the intricate effects of catalyst agglomerate shape on the fuel cell's performance.

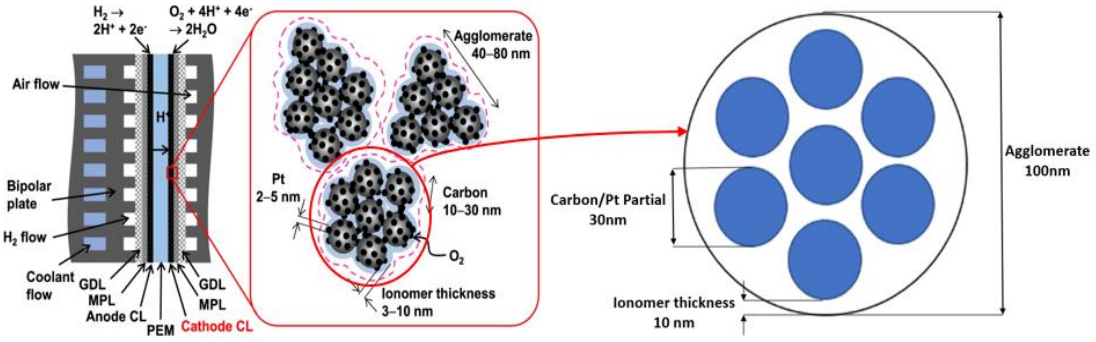

Figure 6.1 A schematic showing the multi-scale structure of the catalyst layer [141]**.**

Analyzing the microscopic images of the catalyst displayed in Figure 6.1 reveals that the agglomerates present within the catalyst layer do not consistently adopt a uniform distribution in the form of spheres. The catalyst agglomerates developed in this study are characterized by distinct active and non-active regions. The active domains (highlighted by the red sections in the figure) are comprised of platinum nanoparticles, carbon particles, and ionomer. Conversely, the non-active regions are assumed to exclusively consist of ionomer material. To facilitate comparisons, the only variable under investigation in this study is the shape of the catalyst, as depicted in Figure 6.2: (i) spherical, (ii) square, (iii) octahedron, (iv) cylindrical, and (v) ellipsoidal. The agglomerate model proposed in this chapter adheres to a 10:1 ratio between the agglomerate's radius and the thickness of the non-active region. Consequently, when the agglomerate radius measures 100 nm, the non-active region maintains a 10 nm thickness. Given the symmetry of the constructed geometries and for computational efficiency, the generated agglomerate represents just 1/8 of its actual size. The equations governing the reactions and transport phenomena within the agglomerate will be expounded upon in the subsequent sections of this chapter.

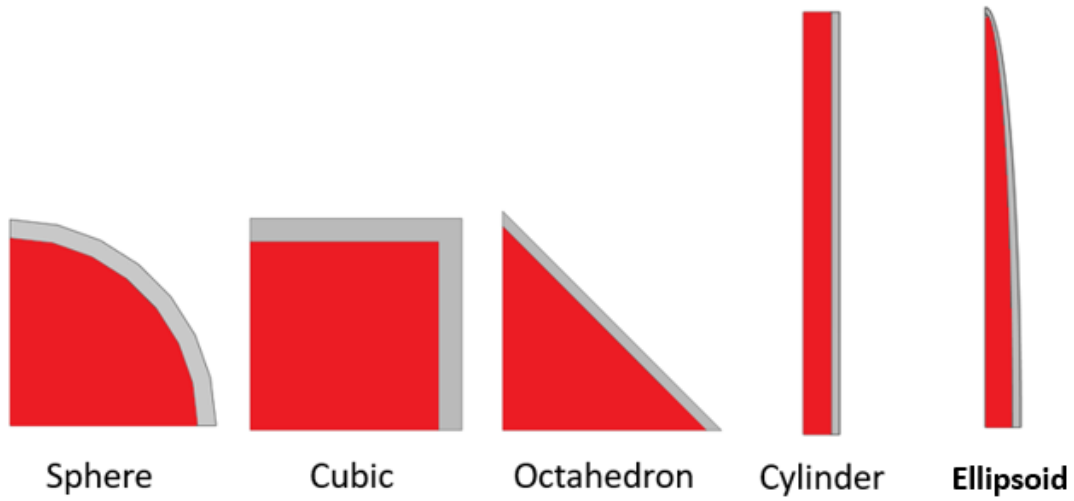

Figure 6.2 A schematic of the shapes of the agglomerate.

6.3.1 Agglomerate model

The transport of the reactant gas (oxygen, in this context) within the agglomerate is realistically envisioned as taking place via diffusion, resulting in its subsequent engagement with the active clusters positioned inside the agglomerate for reaction. and described with the following equation [146]:

$$\nabla D_e^{eff} \nabla C_{O_2} - R_{exn,O_2} = 0 \tag{6.1}$$

where, C_{O_2} stands for the molar concentration of oxygen in solution, while ∇D_e^{eff} denotes the effective diffusivity of dissolved oxygen within the ionomer phase. This value is established by utilizing the Bruggeman relation [26]:

$$D_e^{eff} = \begin{cases} D_e & \text{in the non-active region} \\ \varepsilon_e^{1.5} D_e & \text{in the active clusters} \end{cases} \tag{6.2}$$

Within this formula, D_e denotes the diffusivity of dissolved oxygen within the ionomer, ε_e stands for the volume fraction of the ionomer phase present in the active region, and R_{exn,O_2}

represents the oxygen molar consumption rate. This specific value is determined by the subsequent expression:

$$R_{exn,O_2} = \begin{cases} 0 & \text{in the non-active region} \\ kC_{O_2} & \text{in the active clusters} \end{cases} \quad (6.3)$$

$$k = \frac{i_0 a}{4FC_{O_2}^{ref}} \exp\left(\frac{-\alpha F}{RT}\eta\right) \quad (6.4)$$

In this equation, k represents the reaction rate constant, i_0 denotes the exchange current density, F stands for the Faraday's constant, $C_{O_2}^{ref}$ signifies the reference concentration of the dissolved oxygen, α represents the charge coefficient, T is the temperature, R corresponds to the universal gas constant, η indicates the activation over-potential which is one the input variables for the model, and a represents the specific surface area of the catalyst [108]:

Within this formula, k symbolizes the reaction rate constant, i_0 embodies the exchange current density, F represents Faraday's constant, $C_{O_2}^{ref}$ signifies the reference concentration of dissolved oxygen, α relates to the charge transfer coefficient, T denotes temperature, R stands for the universal gas constant, η signifies the activation over-potential, a vital input parameter for the model, and a represents the specific surface area of the catalyst.

$$a = \frac{l_{pt}A_{pt}}{L_{cl}} \quad (6.5)$$

where l_{pt}corresponds to the quantity of loaded platinum, A_{pt} signifies the electrochemical surface area encompassed by the platinum catalyst, and L_{cl} represents the thickness of the catalyst layer. The average current density of the agglomerate (notated as $\overline{I_{agg}}$) is calculated by applying Faraday's principle:

$$\overline{I_{agg}} = 4Fk\overline{C_{O_2}} \quad (6.6)$$

In this context, $\overline{C_{O_2}}$ symbolizes the average concentration within the active clusters. The boundary conditions, utilized for solving the equations mentioned earlier, are visualized in Figure 6.3. At the agglomerate's surface, a consistent dissolved oxygen concentration ($C_{O_2,o}$) is upheld, while symmetrical lines within the computational domain are subject to a zero flux of dissolved oxygen concentration (∇C_{O_2}=0).

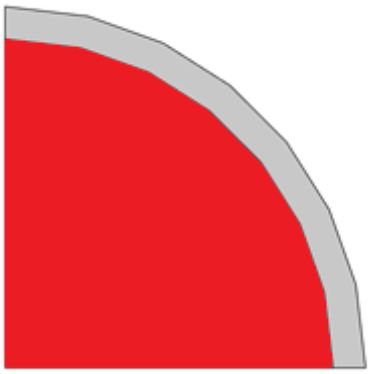

Figure 6.3 The boundary conditions used for the agglomerate model.

For solving Equation (6.1), the software COMSOL Multiphysics 6.0 was utilized. The GMRES (Generalized Minimum Residual) iterative linear solver was implemented. The refinement of the mesh was concentrated around the interfaces connecting active clusters and non-active regions. An assessment of mesh independence was carried out, involving a reduction of the maximum mesh size from 0.003 to 0.0003. This alteration resulted in a minor average current density variation of less than 1%. Consequently, the mesh with a maximum size of 0.003 was chosen. This mesh configuration comprised approximately 110,000 elements; Figure 6.4 illustrates the modelled geometry of the catalyst agglomerate with well-defined active clusters and the accompanying mesh structure. The computational process, encompassing mesh generation and model solution, demanded approximately 60 minutes, utilizing an Intel Xeon 3.80 GHz processor.

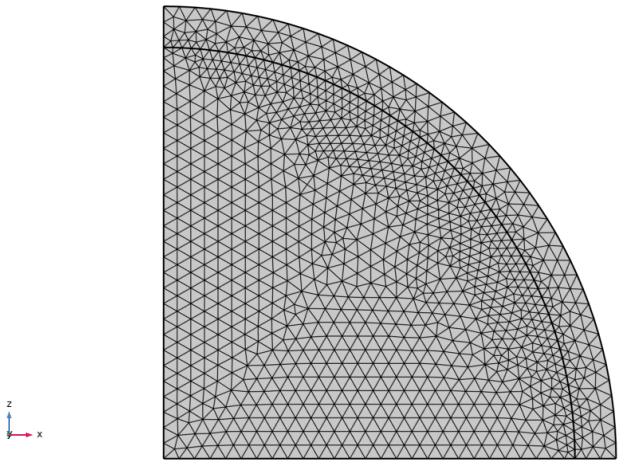

Figure 6.4 Schematic of the meshed geometry of the agglomerate model.

6.3.2 PEFC model

Figure 6.5 presents a schematic of the 1-D PEFC model, highlighting the boundary conditions employed for solving the model – these conditions will be revisited in a later section. To enhance clarity, it is assumed that the fuel cell functions under isothermal and low-humidity conditions, aimed at isolating thermal and saturation impacts. As a result, solely the conservation equations for chemical species and charge are considered. Following this clarification, the subsequent section delineates the fundamental equations that govern the model.

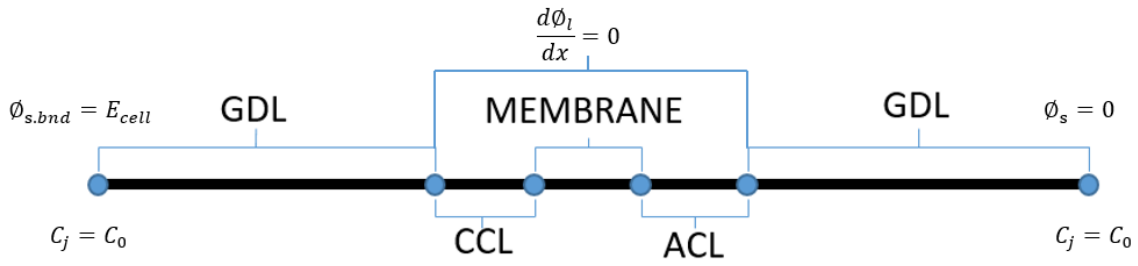

Figure 6.5 A schematic demonstration of the boundary conditions used in the 1-D PEFC model.

The equation representing the continuity is formulated as follows:

$$\nabla \cdot (\rho \vec{u}) = 0 \tag{6.7}$$

The velocity vector is denoted by $\vec{u}$, while ρ represents the gaseous mixture's density. The conservation of species equations are derived from the subsequent expression:

$$\rho(\vec{u} \cdot \nabla) = -\nabla(j_i) + R_i \tag{6.8}$$

where ω_i indicates the fraction of mass associated with species *i*, j_i represents the mass flux relative to the velocity of species *i*, which is averaged by mass, and R_i is the parameter within this equation that signifies the rate of generation or reduction. The specific definition of j_i is provided below [119]:

$$j_i = -\rho\omega_i \sum_k D_{ik}^{eff} \frac{M}{M_k} (\nabla\omega_k + \omega_k \frac{\nabla M}{M}) \tag{6.9}$$

where $D_{ik,eff}$ signifies the effective diffusivity of chemical species i within chemical species k, with ω representing the mass fraction of the species, and ρ indicating the density of the gas mixture. For ideal gas mixtures, the density is formulated as follows:

$$\rho = \frac{pM}{RT} \tag{6.10}$$

where p signifies the absolute pressure. The molecular weight, denoted as *M*, is established as

$$M = \sum \chi_i M_i \tag{6.11}$$

where χ_i is the mole fraction of the chemical species i and M_i is the molar mass, The effective diffusivity $D_{ik,eff}$ in the GDL or the catalyst layer (CL) is calculated by:

where χ_i denotes the mole fraction of the chemical species i, while M_i signifies the molar mass. The computed effective diffusivity value, $D_{ik,eff}$, within either the Gas Diffusion Layer (GDL) or the Catalyst Layer (CL), is calculated by the following equations:

$$D_{ik,eff} = 0.008e^{4.81\varepsilon}D_{ik} \tag{6.12}$$

$$D_{ik,eff} = \varepsilon_{cl}^{1.5}D_{ik} \tag{6.13}$$

The porosity of the GDL is represented by ε, and the source term R_i presented in Equation (6.8) is defined by:

$$R_i = \frac{I}{nF} \tag{6.14}$$

where n corresponds to the number of electrons exchanged in the reaction (4 for oxygen and 2 for hydrogen and water). The computation of the local volumetric current density, represented as *I*, relies on the findings obtained from the agglomerate-scale model, as further detailed later in this section. The determination of water vapor is accomplished by:

$$S_{H_2O} = 2R_i + nd\nabla \cdot i/F \tag{6.15}$$

The drag coefficient, noted as nd, is a factor in the equation, and the equations governing the conservation of charge are provided by:

$$\nabla(-\sigma_s\nabla\phi_s) = \nabla \cdot i \tag{6.16}$$

$$\nabla(-\sigma_l\nabla\phi_l) = -\nabla \cdot i \tag{6.17}$$

where σ_s and σ_l represent the electrical conductivity of the solid phase and the ionic conductivity of the ionomer phase, respectively. Similarly, ϕ_s and ϕ_l characterize the potentials within the solid and ionomer phases. It's noteworthy that Equation (6.17) applies to both Gas Diffusion Layers (GDLs) and Catalyst Layers (CLs), whereas Equation (6.18) is specific to the Catalyst Layer (CL) and the membrane electrolyte. Describing the local activation over-potential η in the cathode's catalyst layer,η_c follows as:

$$\eta_c = \phi_s - \phi_l - E_{eq} \tag{6.18}$$

The theoretical cell potential, denoted as E_{eq}, was computed utilizing the Nernst equation [37] and determined to be 1.221V. Similarly, the local activation over-potential in the anode's catalyst layer,η_a is expressed as:

$$\eta_a = \phi_s - \phi_l \tag{6.19}$$

The calculation of the local volumetric current density within the cathode's catalyst layer, denoted as I_c, is accomplished through the utilization of the subsequent equation [119].

$$I_c = \overline{I_{agg}}(1 - \varepsilon_{cl}) \tag{6.20}$$

The computation of the local volumetric current density within the cathode's catalyst layer, referred to as I_c, involves the utilization of the subsequent equation. Here, $\overline{I_{agg}}$ signifies the average volumetric current density of the modeled agglomerate, derived from Equation (6.6), while ε_{cl} stands for the porosity of the catalyst layer. It's noteworthy that $I_c$varies with both the cathode activation overpotential and the concentration of dissolved oxygen. As a result, $\overline{I_{agg}}$ is recurrently determined by employing realistic values for the cathode activation overpotential and the concentration of dissolved oxygen. The resulting values of $\overline{I_{agg}}$ are subsequently employed as inputs in an interpolation function for the computation of I_c.

Figure 6.6 illustrates a typical interpolation function for the volumetric current density of the agglomerate. On a different note, the local volumetric current density at the anode is derived using the following variation of the Butler-Volmer equation:

$$I_a = i_o a \left(exp\left(\frac{\alpha_a F \eta}{RT}\right) - exp\left(\frac{-\alpha_c F \eta}{RT}\right)\right) \tag{6.21}$$

$$i_o = i_{0,a} \prod_{i:\nu_i>0} \left(\frac{p_i}{p_{i,ref}}\right)^{\alpha_c \nu_i / n} \prod_{i:\nu_i<0} \left(\frac{p_i}{p_{i,ref}}\right)^{-\alpha_a \nu_i / n} \tag{6.22}$$

$$\alpha_a = n - \alpha_c \tag{6.23}$$

Within this equation, i_o represents the reference exchange current density for a single unit of active surface area, a stands for the active surface area, determined through the application of Equation 6.5. Moreover, α_a and α_c stand for the charge transfer coefficients associated with the anode and cathode electrodes, respectively. Additionally, n signifies the number of participating electrons. The overpotential, denoted as η, is calculated using Equation 6.19. Importantly, it should be noted that the exclusive purpose of the Butler-Volmer equation is to compute the anodic local current density, referred to as I_a. Conversely, the cathodic local current density is obtained through the utilization of Equation 6.20.

When considering a specific cell potential, the local volumetric current density at either the cathode or anode is averaged across the length of the catalyst layer. This averaged value is then multiplied by the corresponding length, resulting in a data point on the polarization curve. The arrangement of boundary conditions used in the model is depicted in Figure 6.5. The concentration boundary conditions were imposed on both the left and right sides of the computational domain. Similarly, the solid-phase potential was assigned at the

corresponding positions; it matches the cell potential at the outermost point of the cathode GDL and remains zero at the outermost point of the anode GDL. Conversely, zero-flux ionomer-phase boundary conditions were enforced at the outermost points of the catalyst layers. For solving the governing equations in the fuel cell scale model, COMSOL Multiphysics® 6.0 was utilized. The selected solver for this purpose was MUMPS, a well-known sparsely direct and highly parallel linear system solver. The computational domain was discretized, with particular attention given to refining the mesh near the interface between the catalyst layer and the GDL. This refining process was conducted until a solution that was independent of the mesh size was achieved. The maximum element size was defined as 0.012 μm, along with a maximum element growth rate of 1.2. This choice aimed to prevent any unstable behaviour in the high current density region of the polarization curve. Larger element sizes were determined to be inappropriate, while smaller ones had minimal impact on the current density values. The resulting mesh configuration comprised approximately 125 elements.

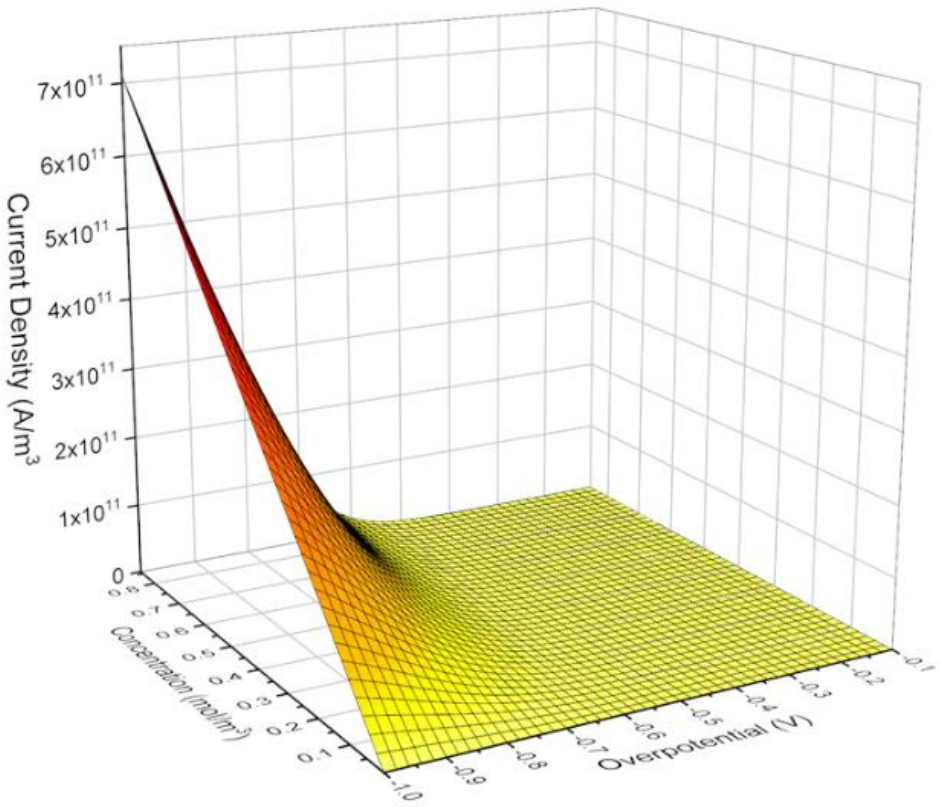

Figure 6.6 Interpolation plot for the agglomerate volumetric current density.

Table 6.1 The parameters used in the models.

Parameter	value
Thickness of membrane (L_{mem})	30um
Thickness of catalyst layer (L_{cl})	15um
Thickness of GDL (L_{GDL})	250um
Cathode charge transfer coefficient (α_a)	3.39
Pressure (p)	1.5atm

Temperature (T)	353K
Faradays' constant (F)	96485Cmol^{-1}
Universal gas constant (R)	$8.314\text{mol}^{-1}\text{K}^{-1}$
Henry's constant (H)	31664 $\text{Pa}\cdot\text{m}^3\text{mol}^{-1}$
Electrochemical active area of platinum particles (A_{pt})	$40\text{m}^2\text{g}^{-1}$ [147]
Platinum loading (l_{pt})	0.4mgcm^{-2}
Anode Exchange current density ($i_{0,a}$)	100Am^{-2}
Cathode Exchange current density ($i_{0,c}$)	0.015Am^{-2} [119]
Reference dissolved O_2 concentration ($c_{O_2}^{ref}$)	0.85molm^{-3} [119]
Porosity of anode/cathode CL (ε_{cl})	0.48
Porosity of anode/cathode GDL (ε)	0.6
Ionomer volume fraction in the agglomerate (ε_e)	0.5 [119]
Oxygen diffusivity in the ionomer (D_{e})	$8.45 \times 10^{-10}\ \text{m}^2/s$ [146]
Oxygen in nitrogen diffusivity ($D_{O_2-N_2}$)	$1.86 \times 10^{-5}\ \text{m}^2/s$ [146]

Oxygen in Water vapour diffusivity ($D_{O_2-H_2o}$)	2.47×10^{-5} m$^2/s$ [146]
Water vapour in nitrogen diffusivity ($D_{H_2o-N_2}$)	2.58×10^{-5} m$^2/s$ [146]
Electric conductivity of gas diffusion layer (σ_{GDL})	100 S/m [119]
Electric conductivity of electrolyte (σ_m)	0.8 S/m
Electric conductivity of catalyst layer (σ_{CL})	30 S/m [119]
Net drag coefficient, (nd)	$1(\eta < 0.25V)$ $46\eta^2 - 31.52\eta + 5.7(0.25 \leq \eta \leq 0.35V)$ $0.3(\eta > 0.2V)$ [146]

6.4 Results and discussion

6.4.1 Validation of the model

To verify the accuracy of the present multi-scale model, it is crucial to compare its output, represented as a polarization curve, with the corresponding results obtained from the conventional model where the impact of agglomerates is analytically linked. Under the assumption of spherical agglomerates, the cathodic current density utilized for validation is formulated as follows [138], [137]:

$$\nabla \cdot i_c = 4F(1-\varepsilon_{cl})C_{O_2,o}\frac{{r_{agg}}^3}{(r_{agg}+\delta_{agg})^3}\left(\frac{1}{E_r k}+\frac{r_{agg}\delta_{agg}}{a_{agg}(r_{agg}+\delta_{agg})D_e}\right)^{-1} \quad (6.24)$$

where $C_{O_{2,o}}$stands for the predetermined oxygen concentration at the surface of the ionomer film. This concentration can be determined through the utilization of Equation 6.25.

$$C_{O_{2,o}} = \frac{C_{O_{2,g}} RT}{H} \tag{6.25}$$

Where $C_{O_{2,g}}$ denotes the concentration of oxygen within the gas phase before it gets assimilated into the ionomer film's surface. **R** stands for the ideal gas constant, and *H* represents Harry's constant. For the purpose of this discussion, the agglomerate is assumed takes on a spherical form. The specific surface area of the agglomerate, defined as a_{agg}, is calculated through the following equation:

$$a_{agg} = \frac{4\pi r_{agg}^2}{4/3\pi r_{agg}^3} = \frac{3}{r_{agg}} \tag{6.27}$$

With the agglomerate's radius designated as r_{agg}, the efficiency factor of the spherical agglomerate E_r employed in Equation 6.24 can be calculated as follows [148], [146]:

$$E_r = \frac{1}{\Phi_L}\left(\frac{1}{\tanh(3\Phi_L)} - \frac{1}{3\Phi_L}\right) \tag{6.28}$$

The Thiele modulus, represented by Φ_L, can be determined through the following equation:

$$\Phi_L = \frac{r_{agg}}{3}\sqrt{\frac{k}{D_e^{eff}}} \tag{6.29}$$

The equations for comparison with the numerical model involve calculating the cathode current density of the analytical model through the utilization of the equation: (6.24), (6.25), (6.26), (6.27), (6.28), (6.29).

Figure 6.6 visually demonstrates the notable correspondence between the polarization curves produced by both approaches. This result instils a sense of confidence in the accuracy of the predictions provided by the multi-scale model developed within this investigation.

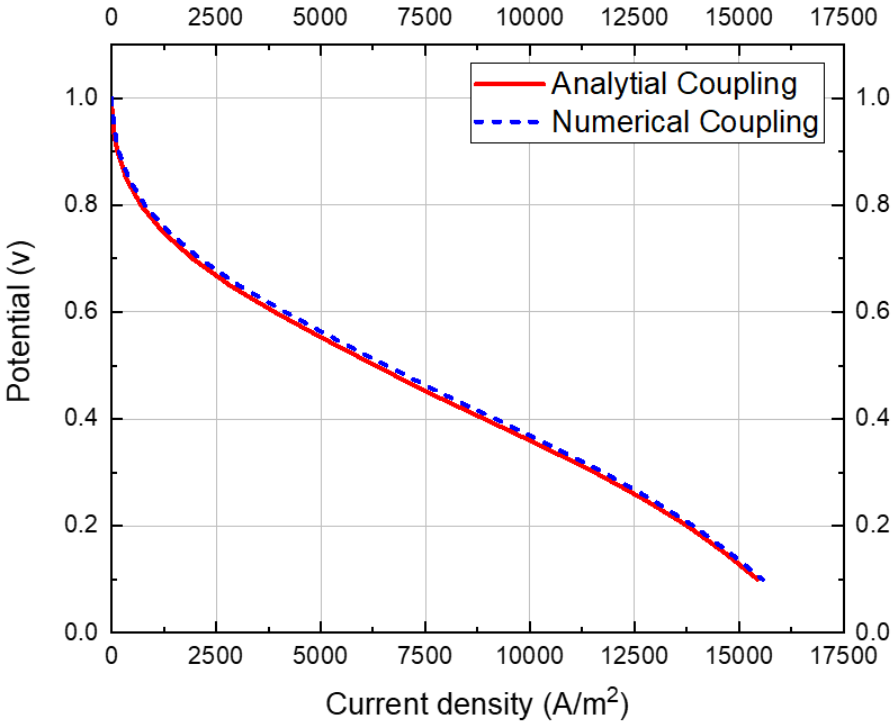

Figure 6.7 The polarisation curves generated from the multi-scale model and the conventional agglomerate PEFC model (red line).

6.4.2 Catalyst agglomerate performance

Figure 6.8 illustrates the performance curves derived from the agglomerate-scale models applied to agglomerates of varying shapes ("spherical", "cubic", "octahedral", "cylindrical", and "ellipsoidal") and sizes (100 and 1000 nanometers). Correspondingly, Table 6.2 (and 6.3) outlines the average volumetric current density for each respective scenario. The findings from these analyses shows that: as the dimensions of the agglomerate decrease, the catalyst agglomerate's performance improves, indicated by an increase in the maximum

current density. To exemplify, in the case of the "ellipsoidal" agglomerate, diminishing the radius from 1000 nanometers to 100 nanometers culminates in an impressive 72-fold escalation in the average volumetric current density. This augmentation can be attributed to the heightened catalyst utilization demonstrated by the smaller agglomerates. Essentially, within these agglomerates, the reactant gas (in this case, oxygen) undergoes swift consumption as it enters the active clusters (see Figure 6.7). Consequently, a noteworthy portion of the active region remains largely untapped. This tendency becomes more significant with larger catalyst agglomerates, resulting in a reduced volumetric current density exhibited by these agglomerates.

Table 6.2 The volumetric current density look up table of the 100nm agglomerates with different internal structure.

	Volumetric Current Density 100(Am^3)				
Overpotential(V)	**spherical**	**cubic**	**octahedron**	**cylinder**	**ellipsoid**
-0.1	1.20E+06	1.20E+06	1.20E+06	1.20E+06	1.20E+06
-0.14	2.68E+06	2.68E+06	2.68E+06	2.68E+06	2.68E+06
-0.18	5.97E+06	5.97E+06	5.97E+06	5.97E+06	5.97E+06
-0.22	1.33E+07	1.33E+07	1.33E+07	1.33E+07	1.33E+07
-0.26	2.96E+07	2.97E+07	2.97E+07	2.97E+07	2.97E+07
-0.3	6.61E+07	6.61E+07	6.61E+07	6.61E+07	6.61E+07
-0.34	4.89E+08	4.89E+08	4.90E+08	4.90E+08	4.91E+08

-0.38	3.54E+09	3.56E+09	3.57E+09	3.62E+09	3.63E+09
-0.42	2.26E+10	2.33E+10	2.37E+10	2.58E+10	2.62E+10
-0.46	9.37E+10	1.04E+11	1.11E+11	1.51E+11	1.62E+11
-0.5	2.47E+11	2.88E+11	3.37E+11	5.05E+11	6.11E+11
-0.6	4.77E+11	5.73E+11	7.75E+11	1.06E+12	1.36E+12
-0.7	7.11E+11	8.69E+11	1.38E+12	1.65E+12	2.22E+12
-0.8	1.20E+06	1.20E+06	1.20E+06	1.20E+06	1.20E+06
-0.9	2.68E+06	2.68E+06	2.68E+06	2.68E+06	2.68E+06
-1	5.97E+06	5.97E+06	5.97E+06	5.97E+06	5.97E+06

Table 6.3 the volumetric current density look up table of the 1000nm agglomerates with different internal structure.

Volumetric Current Density 1000nm(Am^3)					
Overpotential(V)	**spherical**	**cubic**	**octahedron**	**cylinder**	**ellipsoid**
-0.1	1.20E+06	1.20E+06	1.20E+06	1.20E+06	1.20E+06
-0.14	2.67E+06	2.67E+06	2.67E+06	2.67E+06	2.67E+06
-0.18	5.94E+06	5.94E+06	5.95E+06	5.96E+06	5.96E+06
-0.22	1.32E+07	1.32E+07	1.32E+07	1.33E+07	1.33E+07
-0.26	2.90E+07	2.91E+07	2.92E+07	2.95E+07	2.95E+07

-0.3	6.29E+07	6.35E+07	6.39E+07	6.54E+07	6.56E+07
-0.34	3.65E+08	3.83E+08	3.95E+08	4.53E+08	4.62E+08
-0.38	1.30E+09	1.46E+09	1.61E+09	2.31E+09	2.57E+09
-0.42	3.10E+09	3.65E+09	4.45E+09	6.47E+09	8.07E+09
-0.46	5.61E+09	6.65E+09	9.63E+09	1.20E+10	1.62E+10
-0.5	7.87E+09	9.36E+09	1.56E+10	1.69E+10	2.43E+10
-0.6	8.95E+09	1.07E+10	1.89E+10	1.97E+10	2.90E+10
-0.7	9.21E+09	1.11E+10	1.96E+10	2.06E+10	3.05E+10
-0.8	1.20E+06	1.20E+06	1.20E+06	1.20E+06	1.20E+06
-0.9	2.67E+06	2.67E+06	2.67E+06	2.67E+06	2.67E+06
-1	5.94E+06	5.94E+06	5.95E+06	5.96E+06	5.96E+06

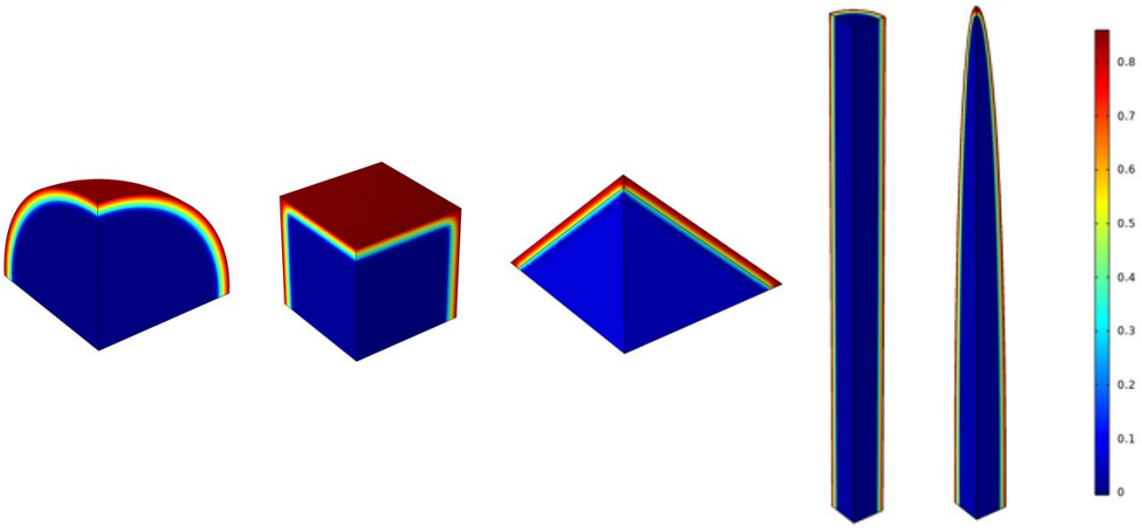

Figure 6.8 The contours of the oxygen distribution in the 100nm agglomerate (a) overlap, (b) contact and (c) separate.

The second observation is that, regardless of the agglomerate size, the performance of agglomerates with larger contact surface area of active clusters is superior. In this study, when the agglomerate has an ellipsoidal shape, its performance is the best. This is because ellipsoidal agglomerates have the largest total surface area, while spherical agglomerates have the smallest total surface area; the larger the surface area of the active region of the agglomerate, the better the catalyst utilization. As explained in Section 6.2, the curves shown in Figure 6.8 are used as interpolation functions for the proton exchange membrane fuel cell scale model.

100nm **1000nm**

(a) spherical

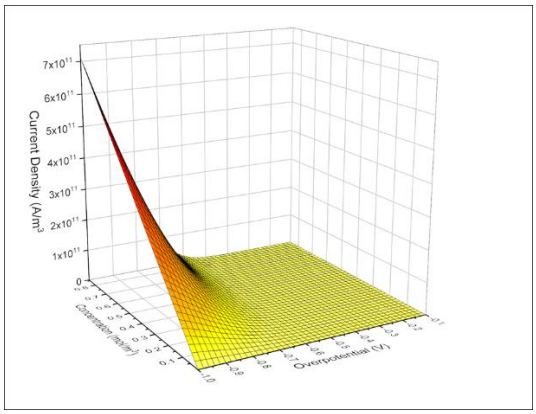

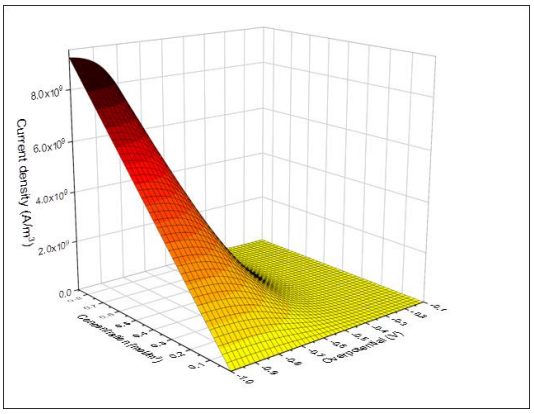

(b) cubic

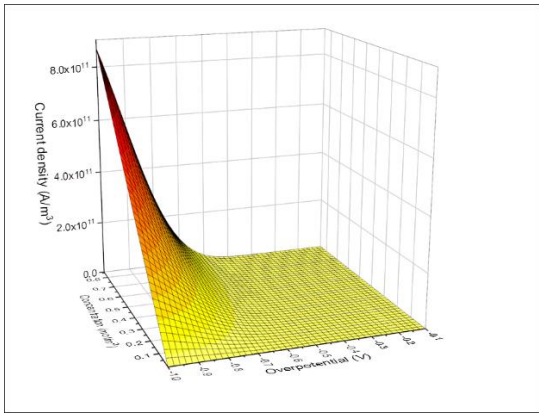

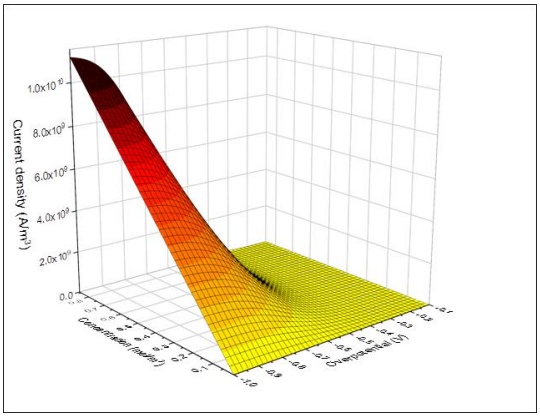

(c) octahedon

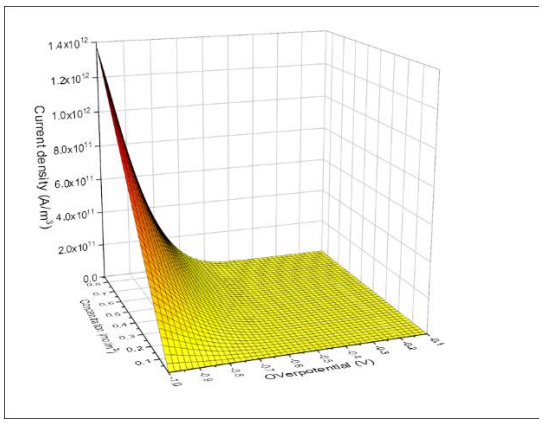

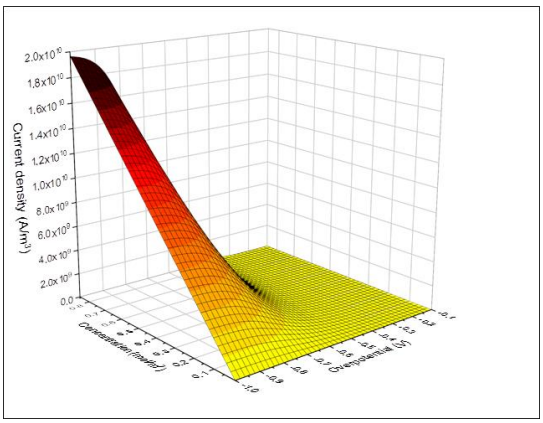

(d) cylinder

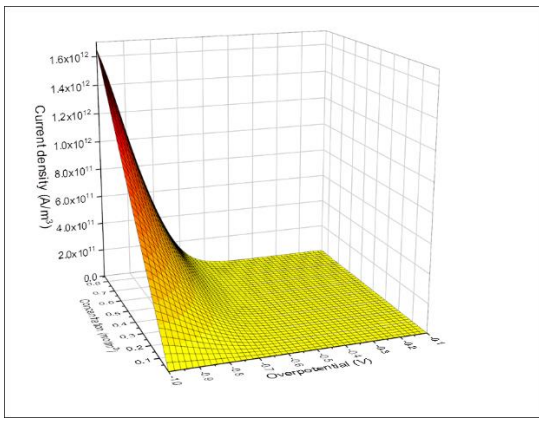

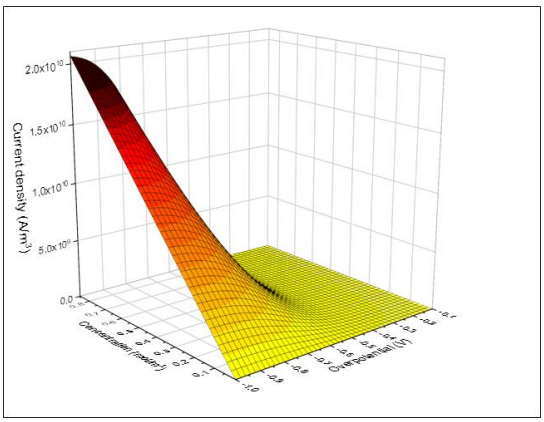

(e) ellipsoid

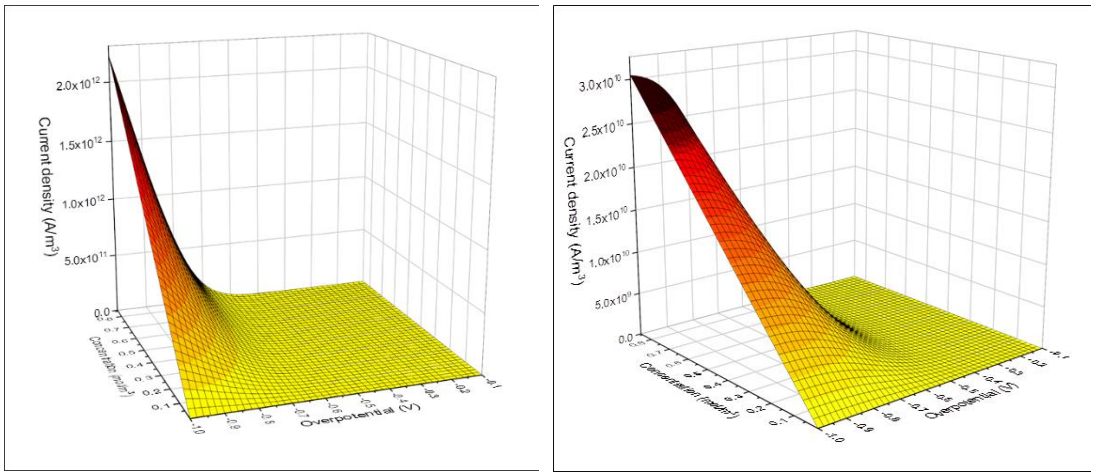

Figure 6.9 The volumetric current density of the agglomerate as a function of activation overpotential and dissolved oxygen concentration for two agglomerate sizes (100 and 1000 nm) and three different internal structures (separate, contacting and overlapping active clusters).

6.4.3 Fuel cell performance

Figure 6.9 presents the polarization curves of proton exchange membrane fuel cells featuring catalyst agglomerates of varying sizes (100 and 1000 nanometers) and five distinct shapes ("spherical", "cubic", "octahedral", "cylindrical", and "ellipsoidal").

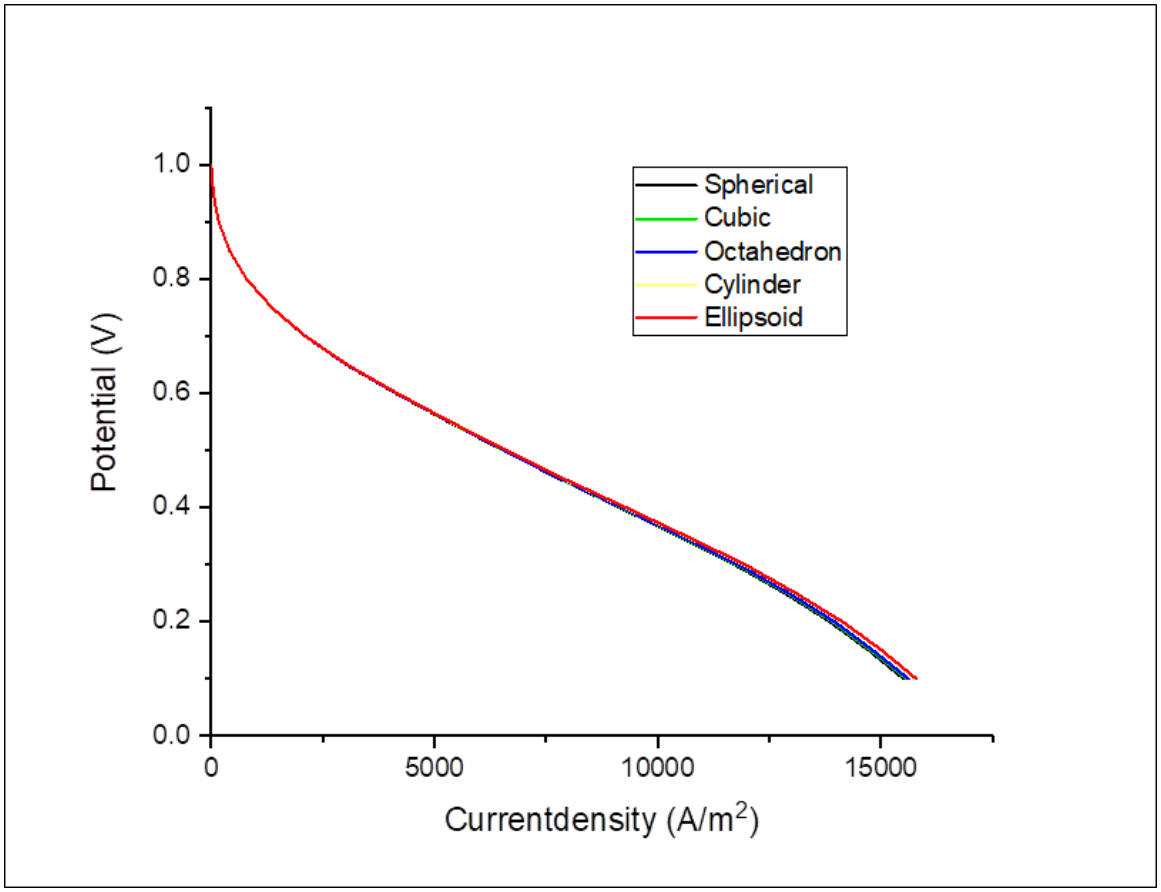

Figure 6.10 The polarisation curves of the modelled fuel cell with 100 nm radius agglomerates characterised by separate, contacting or overlapping active clusters.

Upon examination, it becomes evident that fuel cells equipped with ellipsoidal-shaped agglomerates manifest superior performance. This is attributed to the ellipsoidal agglomerates having a larger specific surface area compared to the other shapes. Beyond the influence of shape, our observations unveil an intriguing trend: as the agglomerate radius increases from 100 to 1000 nanometers (Figure 6.10), the impact of agglomerate shape on fuel cell performance assumes a heightened significance. For instance, among smaller agglomerates, the ellipsoidal-shaped ones exhibit a marginal 1.8% increase in maximum current density compared to spherical-shaped active clusters. On the other hand, for larger agglomerates, the ellipsoidal-shaped agglomerates show a remarkable approximately 28% surge in maximum current density over their spherical-shaped agglomerate.

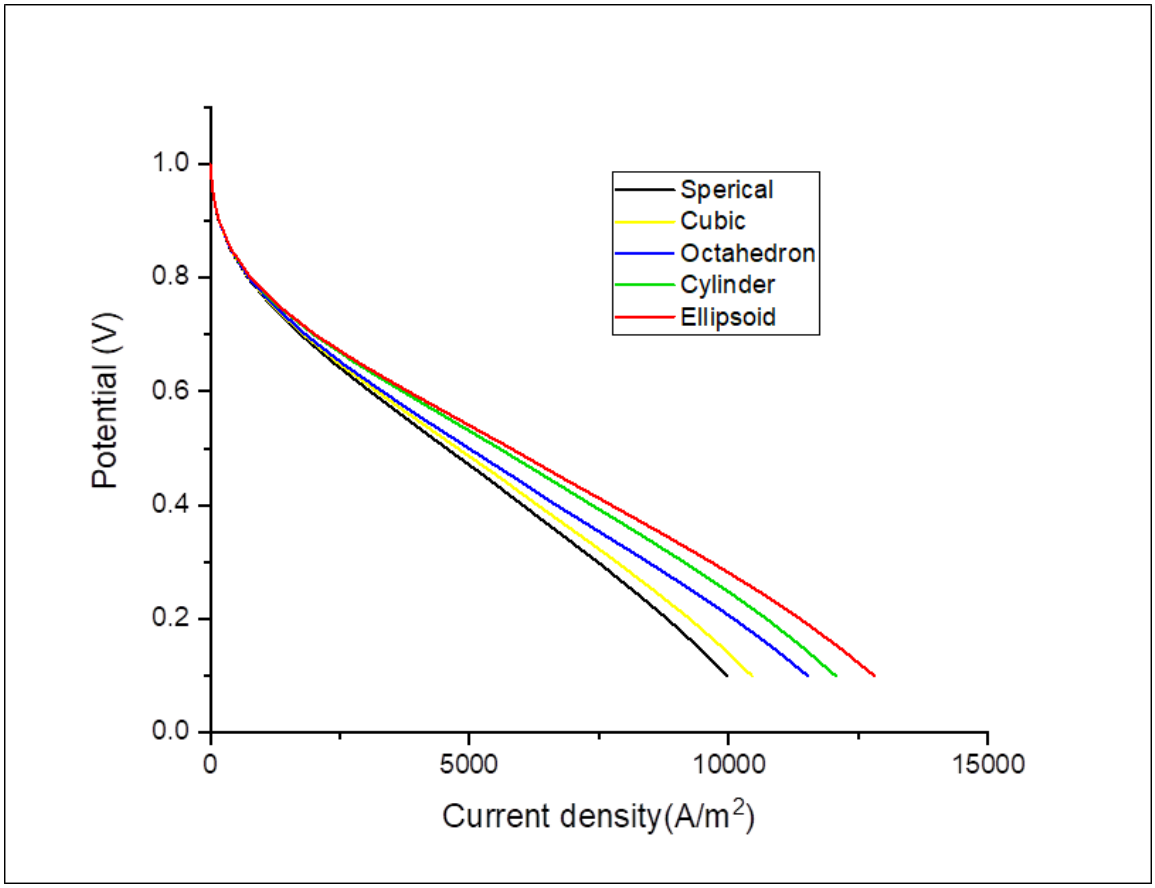

Figure 6.11 The polarisation curves of the modelled fuel cell with 1000 nm radius agglomerates characterised by separate, contacting or overlapping active clusters.

These results highlight the substantial influence of catalyst shape on overall fuel cell performance. This phenomenon can be attributed to larger catalyst agglomerates presenting longer diffusion paths, resulting in an increased mass transport resistance when compared to their smaller agglomerates. This implication is particularly notable in regions of high current density, where the fuel cell's performance is more significantly constrained by mass transport resistance. The sensitivity to agglomerate size aligns cohesively with the research findings reported by Kamarajugadda et al. [137] and Ismail et al. [119].

6.5 Conclusions

This study introduces a novel multiscale model that investigates the impact of catalyst agglomerate micro shapes on the overall performance of fuel cells, aiding in the optimization of catalyst shapes. The main innovation of this model lies in its ability to integrate both the agglomerate scale and fuel cell scale. This integration is crucial because catalyst agglomerates, as observed in micrographs of the catalyst layer, are not always perfectly spherical; they exhibit various geometrical structures. With the emergence of new synthesis methods and continually improving nanomanufacturing technologies, obtained the capability to design catalysts with diverse materials and structures. By combining these scales, the efficiency of designing new catalysts is enhanced. The primary focus of this article is to explore, though not exclusively, the impact of catalyst shapes – spherical, cubic, octahedral, cylindrical, and ellipsoidal – on fuel cell performance. The process involves two steps: first, solving the agglomerate model through reaction-diffusion equations, and then coupling these results with the fuel cell model to obtain polarization curves. These results are compared and validated against traditional models. After achieving good consistency, this multiscale model is used to study the size effect and the impact of agglomerate shapes on overall fuel cell performance. Ultimately, the following findings were uncovered:

i. When agglomerates are small (100nm), the impact of agglomerate shape on fuel cell performance is not significant. The performance differences caused by the five different agglomerate shapes can be almost ignored.

ii. When agglomerates are larger (1000nm), the agglomerate shape has a significant effect on fuel cell performance. Under this size, ellipsoidal-shaped agglomerates yield the best fuel cell performance, with a current density increase of about 28%

compared to spherical-shaped agglomerates. This is because ellipsoidal agglomerates offer a larger specific surface area.

iii. The size effect of agglomerates is substantial. Smaller agglomerates lead to better fuel cell performance, with a 26% increase in maximum current density compared to larger agglomerates. This is due to smaller catalysts providing shorter diffusion paths, resulting in improved catalyst utilization.

Chapter 7 Conclusions and Future Work

7.1 Conclusions

This thesis presents a simulation and optimization study focusing on the flow field channel and catalyst layers in polymer electrolyte membrane fuel cells (PEMFCs). The research on the flow field plates primarily centres on optimizing their cross-sectional shapes using three-dimensional numerical models. In the case of the catalyst layer, two main models were employed. The first is a traditional model used to investigate the fundamental catalyst parameters, while the second is a multiscale model designed to delve into the microstructure and shape of catalyst agglomerates, exploring how these factors influence the overall performance of the fuel cell.

The investigation into the flow channel configurations revealed that there is a shift from square to trapezoidal cross-sections and the adoption of a hybrid cross-section, featuring a square inlet and trapezoidal outlet, which significantly improved the fuel cell performance. The hybrid configuration, in particular, demonstrated a 5% increase in the current density at 0.4 V, attributed to the enhanced reactant gas supply, heat dissipation, and water removal. Furthermore, reducing the outlet height of the hybrid cross-section by transitioning from 1 mm to 0.25 mm led to a 6% increase in the current density at 0.4 V, highlighting the importance of the outlet geometry in the optimizing performance.

Exploring the catalyst layer microstructures yielded valuable and important insights. Higher platinum loading and smaller platinum particle radius were identified as catalyst layer parameters that improve the PEMFC performance. Additionally, increasing the electrochemical active area was found to enhance the fuel cell efficiency, underlining the significance of the catalyst structure and composition. Comparing the agglomerate model to

the homogeneous models revealed that the agglomerate model more accurately simulates the PEMFC operation, particularly in the concentration loss region.

The introduction of a multiscale modeling framework that integrated the catalyst agglomerate-scale and fuel cell-scale models provided a deeper understanding of how the internal structure of the catalyst agglomerates impacts the fuel cell performance. The findings indicated that the fuel cells perform optimally with agglomerates featuring separate active clusters. The impact of the agglomerate structure becomes more pronounced as the agglomerate size increases, with smaller agglomerates exhibiting superior catalyst utilization. This study recommends designing catalyst agglomerates with separate active clusters to improve the fuel cell performance while reducing the catalyst loading.

Furthermore, the multiscale model that explored the influence of catalyst agglomerate shapes on the fuel cell performance, offering valuable insights into the catalyst shape optimization. The model integrated the agglomerate and fuel cell scales and demonstrated that, at smaller agglomerate sizes (100 nm), the agglomerate shape had minimal impact on the performance. However, at larger agglomerate sizes (1000 nm), ellipsoidal-shaped agglomerates exhibited the best performance, with a significant increase in the current density compared to spherical-shaped agglomerates. This underscores the importance of considering the agglomerate size and shape in the catalyst design.

In summary, this study has contributed to a comprehensive understanding of factors influencing the PEMFC performance and optimization, paving the way for more efficient and affordable fuel cell technology.

7.2 Future work

This thesis has introduced a promising novel and important design for flow field channels aimed at improving reactant transportation and water removal. It has also outlined a comprehensive approach to the design of innovative catalysts for PEM fuel cells.

For the flow channel, this thesis has primarily focused on simulating single parallel flow channels. To further advance this research, it is crucial to extend this design and explore its suitability in various other common flow configurations, with particular attention to the serpentine flow configuration. Additionally, it is imperative to investigate the potential application of this hybrid design throughout the entire fuel cell system. These expanded applications hold the promise of offering valuable insights on multiple fronts. Firstly, they will shed light on how the performance of fuel cells equipped with the proposed flow channel design is influenced by different flow configurations and computational domain scales. This will involve comparing the performance of a single turn of the fuel cell to that of the entire fuel cell system. Moreover, this extended research can delve deeper into the sensitivity analysis of other key parameters, including water and thermal management. Furthermore, it is essential to incorporate experimental validation into these future research investigations to ensure the design's practical viability.

For the catalyst, this thesis has explored certain pivotal catalyst parameters using two distinct models. Nevertheless, there remain critical factors that demand further investigation in future research works. For instance, the impact of catalyst degradation, poisoning, and overall durability – factors with profound implications for the catalyst performance – should be subject to more comprehensive exploration. Moreover, within the multiscale modelling, it is worth noting that the agglomerate model developed in this thesis did not account for the influence of liquid water. Given that water generated during the cathode oxygen reduction

reaction can significantly affect the reactant transport, future research should prioritize the development of more precise models that incorporate this aspect. While this thesis successfully achieved coupling between a three-dimensional agglomerate model and a one-dimensional fuel cell, future efforts should be geared towards the creation of even more accurate three-dimensional-to-three-dimensional models. Ultimately, for long-term research goals, integrating experimental data into simulations has the potential to expedite the discovery and synthesis of catalysts that are not only more efficient but also more cost-effective.

References

[1] United Nations FC on CC. Adoption of the Paris Agreement. Science (80-.)., vol. 364, 2015, p. 39.6-40. https://doi.org/10.1126/science.364.6435.39-f.

[2] Shimizu K, Sepunaru L, Compton RG. Innovative catalyst design for the oxygen reduction reaction for fuel cells. Chem Sci 2016;7:3364–9. https://doi.org/10.1039/c6sc00139d.

[3] Jiujun Zhang. PEM Fuel Cell Electrocatalysts and Catalyst Layers. PEM Fuel Cell Electrocatal Catal Layers 2008. https://doi.org/10.1007/978-1-84800-936-3.

[4] DOE/GO. 2019 Annual Merit Review and Peer Evaluation Report 2019. URL:https://www.nrel.gov/docs/fy20osti/74379.pdf.

[5] Schmidt-Rohr K. How Batteries Store and Release Energy: Explaining Basic Electrochemistry. J Chem Educ 2018;95:1801–10. https://doi.org/10.1021/acs.jchemed.8b00479.

[6] Bill Vincent, Jennifer Gangi, Sandra Curtin and ED. Comparison of fuel cell technology. US Non-Automotive Fuel Cell Ind Status Outlook 2012:121. https://www.energy.gov/eere/fuelcells/comparison-fuel-cell-technologies.

[7] Bill Vincent, Jennifer Gangi, Sandra Curtin and ED. 2008 fuel cell technologies market report. 2010.

[8] Lathia RV, Dobariya KS, Patel A. Hydrogen Fuel Cells for Road Vehicles. J Clean Prod 2017;141:462. https://doi.org/10.1016/j.jclepro.2016.09.150.

[9] Ovidiu P. The Study of the Efficiency of a Direct Methanol Fuel Cell. J Electr Electron Eng 2014;7:31–4.

[10] Wei Y, Matar S, Shen L, Zhang X, Guo Z, Zhu H, et al. A novel membrane for DMFC - Na 2Ti 3O 7 Nanotubes/Nafion ® composite membrane: Performances studies. Int J Hydrogen Energy 2012;37:1857–64. https://doi.org/10.1016/j.ijhydene.2011.08.107.

[11] Stambouli AB, Traversa E. Solid oxide fuel cells (SOFCs): A review of an environmentally clean and efficient source of energy. Renew Sustain Energy Rev 2002;6:433–55. https://doi.org/10.1016/S1364-0321(02)00014-X.

[12] Strickland K, Miner E, Jia Q, Tylus U, Ramaswamy N, Liang W, et al. Highly active oxygen reduction non-platinum group metal electrocatalyst without direct metal-nitrogen coordination. Nat Commun 2015;6:1–8. https://doi.org/10.1038/ncomms8343.

[13] Mehrpooya M, Sayyad S, Zonouz MJ. Energy, exergy and sensitivity analyses of a hybrid combined cooling, heating and power (CCHP) plant with molten carbonate fuel cell (MCFC) and Stirling engine. J Clean Prod 2017;148:283–94. https://doi.org/10.1016/j.jclepro.2017.01.157.

[14] Kulkarni A, Giddey S. Materials issues and recent developments in molten carbonate fuel cells. J Solid State Electrochem 2012;16:3123–46. https://doi.org/10.1007/s10008-012-1771-y.

[15] Chen X, Wang Y, Cai L, Zhou Y. Maximum power output and load matching of a phosphoric acid fuel cell-thermoelectric generator hybrid system. J Power Sources 2015;294:430–6. https://doi.org/10.1016/j.jpowsour.2015.06.085.

[16] Kakati BK, Mohan V. Development of low-cost advanced composite bipolar plate for proton exchange membrane fuel cell. Fuel Cells 2008;8:45–51. https://doi.org/10.1002/fuce.200700008.

[17] Kakati BK, Deka D. Differences in physico-mechanical behaviors of resol(e) and novolac type phenolic resin based composite bipolar plate for proton exchange membrane (PEM) fuel cell. Electrochim Acta 2007;52:7330–6. https://doi.org/10.1016/j.electacta.2007.06.021.

[18] Zheng W, Kim SH. The effects of catalyst layer microstructure andwater saturation on the effective diffusivity in PEMFC. J Electrochem Soc 2018;165:F468–78. https://doi.org/10.1149/2.0711807jes.

[19] Larminie J, Dicks A. Fuel cell systems explained: Second edition. 2013. https://doi.org/10.1002/9781118878330.

[20] Kahraman H, Orhan MF. Flow field bipolar plates in a proton exchange membrane fuel cell: Analysis & modeling. Energy Convers Manag 2017;133:363–84. https://doi.org/10.1016/j.enconman.2016.10.053.

[21] Li X, Sabir I, Park J. A flow channel design procedure for PEM fuel cells with effective water removal. J Power Sources 2007;163:933–42. https://doi.org/10.1016/j.jpowsour.2006.10.015.

[22] Ismail M. On the Transport Properties of Gas Diffusion Layers used in Proton Exchange Membrane Fuel Cells 2011:34–61.

[23] Tang H, Peikang S, Jiang SP, Wang F, Pan M. A degradation study of Nafion proton exchange membrane of PEM fuel cells. J Power Sources 2007;170:85–92. https://doi.org/10.1016/j.jpowsour.2007.03.061.

[24] Jayakumar A, Sethu SP, Ramos M, Robertson J, Al-Jumaily A. A technical review on gas diffusion, mechanism and medium of PEM fuel cell. Ionics (Kiel) 2015;21:1–18. https://doi.org/10.1007/s11581-014-1322-x.

[25] Yu X, Ye S. Recent advances in activity and durability enhancement of Pt/C catalytic

cathode in PEMFC. Part II: Degradation mechanism and durability enhancement of carbon supported platinum catalyst. J Power Sources 2007;172:145–54. https://doi.org/10.1016/j.jpowsour.2007.07.048.

[26] Talukdar K, Delgado S, Lagarteira T, Gazdzicki P, Friedrich KA. Minimizing mass-transport loss in proton exchange membrane fuel cell by freeze-drying of cathode catalyst layers. J Power Sources 2019;427:309–17. https://doi.org/10.1016/j.jpowsour.2019.04.094.

[27] Khakbaz Baboli M, Harvey DA, Pharoah JG. Investigating the Performance of Catalyst Layer Micro-Structures with Different Platinum Loadings. ECS Trans 2013;50:765–72. https://doi.org/10.1149/05002.0765ecst.

[28] Obut Erdogan SA. Numerical assessment of dependence of polymer electrolyte membrane fuel cell performance on cathode catalyst layer parameters. J Power Sources 2011;196:1920–31. https://doi.org/10.1016/j.jpowsour.2010.10.030.

[29] Bai B, Chen YT. Simulation of the oxygen reduction reaction (ORR) inside the cathode catalyst layer (CCL) of proton exchange membrane fuel cells using the kinetic Monte Carlo method. Energies 2018;11. https://doi.org/10.3390/en11102529.

[30] Winther-Jensen B, Winther-Jensen O, Forsyth M, MacFarlane D. High Rates of Oxygen Reduction. Science (80-) 2008;321:671–4. https://doi.org/10.1126/science.1159267.

[31] Yu D, Nagelli E, Du F, Dai L. Metal-free carbon nanomaterials become more active than metal catalysts and last longer. J Phys Chem Lett 2010;1:2165–73. https://doi.org/10.1021/jz100533t.

[32] Khelashvili G, Behrens S, Weidenthaler C, Vetter C, Hinsch A, Kern R, et al. Catalytic platinum layers for dye solar cells: A comparative study. Thin Solid Films

2006;511–512:342–8. https://doi.org/10.1016/j.tsf.2005.12.059.

[33] Peng Z, Yang H. Designer platinum nanoparticles: Control of shape, composition in alloy, nanostructure and electrocatalytic property. Nano Today 2009;4:143–64. https://doi.org/10.1016/j.nantod.2008.10.010.

[34] Chou SW, Zhu CL, Neeleshwar S, Chen GL, Chen YY, Chen CC. Controlled growth and magnetic property of fept nanostructure: cuboctahedron, octapod, truncated cube, and cube. Chem Mater 2009;21:4955–61. https://doi.org/10.1021/cm902199p.

[35] Wang C, Daimon H, Onodera T, Koda T, Sun S. A general approach to the size- and shape-controlled synthesis of platinum nanoparticles and their catalytic reduction of oxygen. Angew Chemie - Int Ed 2008;47:3588–91. https://doi.org/10.1002/anie.200800073.

[36] Liang Y, Wang H, Diao P, Chang W, Hong G, Li Y, et al. Oxygen reduction electrocatalyst based on strongly coupled cobalt oxide nanocrystals and carbon nanotubes. J Am Chem Soc 2012;134:15849–57. https://doi.org/10.1021/ja305623m.

[37] Stamenkovic VR, Fowler B, Mun BS, Wang G, Ross PN, Lucas CA, et al. Improved oxygen reduction activity on Pt3Ni(111) via increased surface site availability. Science (80-) 2007;315:493–7. https://doi.org/10.1126/science.1135941.

[38] Stamenković V, Schmidt TJ, Ross PN, Marković NM. Surface composition effects in electrocatalysis: Kinetics of oxygen reduction on well-defined Pt3Ni and Pt3Co alloy surfaces. J Phys Chem B 2002;106:11970–9. https://doi.org/10.1021/jp021182h.

[39] Chen C, Kang YJ, Huo ZY, Zhu ZW, Huang WY. Highly Crystalline Multimetallic Nanoframes with Three-Dimensional Electrocatalytic Surfaces. Science (80-) 2014;343:1339–43. https://doi.org/10.1126/science.1249061.

[40] Kongkanand A, Kuwabata S, Girishkumar G, Kamat P. Single-wall carbon nanotubes

supported platinum nanoparticles with improved electrocatalytic activity for oxygen reduction reaction. Langmuir 2006;22:2392–6. https://doi.org/10.1021/la052753a.

[41] Wang J, Yin G, Liu H, Li R, Flemming RL, Sun X. Carbon nanotubes supported Pt-Au catalysts for methanol-tolerant oxygen reduction reaction: A comparison between Pt/Au and PtAu nanoparticles. J Power Sources 2009;194:668–73. https://doi.org/10.1016/j.jpowsour.2009.06.040.

[42] Guo S, Sun S. FePt nanoparticles assembled on graphene as enhanced catalyst for oxygen reduction reaction. J Am Chem Soc 2012;134:2492–5. https://doi.org/10.1021/ja2104334.

[43] Wu J, Pisula W, Müllen K. Graphenes as potential material for electronics. Chem Rev 2007;107:718–47. https://doi.org/10.1021/cr068010r.

[44] Wu ZS, Yang S, Sun Y, Parvez K, Feng X, Müllen K. 3D nitrogen-doped graphene aerogel-supported Fe 3O 4 nanoparticles as efficient electrocatalysts for the oxygen reduction reaction. J Am Chem Soc 2012;134:9082–5. https://doi.org/10.1021/ja3030565.

[45] Wu G, More KL, Johnston CM, Zelenay P. High-performance electrocatalysts for oxygen reduction derived from polyaniline, iron, and cobalt. Science (80-) 2011;332:443–7. https://doi.org/10.1126/science.1200832.

[46] Chen Z, Higgins D, Yu A, Zhang L, Zhang J. A review on non-precious metal electrocatalysts for PEM fuel cells. Energy Environ Sci 2011;4:3167–92. https://doi.org/10.1039/c0ee00558d.

[47] Ding D, Li K, Liu B, Tang BZ. Bioprobes based on AIE fluorogens. Acc Chem Res 2013;46:2441–53. https://doi.org/10.1021/ar3003464.

[48] Wu G, Zelenay P. Nanostructured nonprecious metal catalysts for oxygen reduction

reaction. Acc Chem Res 2013;46:1878–89. https://doi.org/10.1021/ar400011z.

[49] Muñiz J, Marbán G, Fuertes AB. Low temperature selective catalytic reduction of NO over modified activated carbon fibres. Appl Catal B Environ 2000;27:27–36. https://doi.org/10.1016/S0926-3373(00)00134-X.

[50] Gong K, Du F, Xia Z, Durstock M, Dai L. Nitrogen-Doped Carbon Nanotube 2009;323.

[51] Qu L, Liu Y, Baek JB, Dai L. Nitrogen-doped graphene as efficient metal-free electrocatalyst for oxygen reduction in fuel cells. ACS Nano 2010;4:1321–6. https://doi.org/10.1021/nn901850u.

[52] Geng D, Chen Y, Chen Y, Li Y, Li R, Sun X, et al. High oxygen-reduction activity and durability of nitrogen-doped graphene. Energy Environ Sci 2011;4:760–4. https://doi.org/10.1039/c0ee00326c.

[53] Sheng ZH, Shao L, Chen JJ, Bao WJ, Wang F Bin, Xia XH. Catalyst-free synthesis of nitrogen-doped graphene via thermal annealing graphite oxide with melamine and its excellent electrocatalysis. ACS Nano 2011;5:4350–8. https://doi.org/10.1021/nn103584t.

[54] Wang S, Zhang L, Xia Z, Roy A, Chang DW, Baek JB, et al. BCN graphene as efficient metal-free electrocatalyst for the oxygen reduction reaction. Angew Chemie - Int Ed 2012;51:4209–12. https://doi.org/10.1002/anie.201109257.

[55] Du F, Yu D, Dai L, Ganguli S, Varshney V, Roy AK. Preparation of tunable 3D pillared carbon nanotube-graphene networks for high-performance capacitance. Chem Mater 2011;23:4810–6. https://doi.org/10.1021/cm2021214.

[56] Shui J, Wang M, Du F, Dai L. N-doped carbon nanomaterials are durable catalysts for oxygen reduction reaction in acidic fuel cells. Sci Adv 2015;1:1–8.

https://doi.org/10.1126/sciadv.1400129.

[57] Tylianakis E, Dimitrakakis GK, Melchor S, Dobado JA, Froudakis GE. Porous nanotube network: A novel 3-D nanostructured material with enhanced hydrogen storage capacity. Chem Commun 2011;47:2303–5. https://doi.org/10.1039/c0cc03002c.

[58] Shi Q, Peng F, Liao S, Wang H, Yu H, Liu Z, et al. Sulfur and nitrogen co-doped carbon nanotubes for enhancing electrochemical oxygen reduction activity in acidic and alkaline media. J Mater Chem A 2013;1:14853–7. https://doi.org/10.1039/c3ta12647a.

[59] Yu D, Zhang Q, Dai L. Highly efficient metal-free growth of nitrogen-doped single-walled carbon nanotubes on plasma-etched substrates for oxygen reduction. J Am Chem Soc 2010;132:15127–9. https://doi.org/10.1021/ja105617z.

[60] Choi CH, Chung MW, Kwon HC, Chung JH, Woo SI. Nitrogen-doped graphene/carbon nanotube self-assembly for efficient oxygen reduction reaction in acid media. Appl Catal B Environ 2014;144:760–6. https://doi.org/10.1016/j.apcatb.2013.08.021.

[61] Naqvi SAH, Taner T, Ozkaymak M, Ali HM. Hydrogen Production through Alkaline Electrolyzers: A Techno-Economic and Enviro-Economic Analysis. Chem Eng Technol 2023;46:474–81. https://doi.org/10.1002/ceat.202200234.

[62] Taner T, Naqvi SAH, Ozkaymak M. Techno-economic Analysis of a More Efficient Hydrogen Generation System Prototype: A Case Study of PEM Electrolyzer with Cr-C Coated SS304 Bipolar Plates. Fuel Cells 2019;19:19–26. https://doi.org/10.1002/fuce.201700225.

[63] Taner T. The novel and innovative design with using H2 fuel of PEM fuel cell:

Efficiency of thermodynamic analyze. Fuel 2021;302:121109. https://doi.org/10.1016/j.fuel.2021.121109.

[64] Taner T. Energy and exergy analyze of PEM fuel cell: A case study of modeling and simulations. Energy 2018;143:284–94. https://doi.org/10.1016/j.energy.2017.10.102.

[65] Özgür T, Yakaryılmaz AC. A review: Exergy analysis of PEM and PEM fuel cell based CHP systems. Int J Hydrogen Energy 2018;43:17993–8000. https://doi.org/10.1016/j.ijhydene.2018.01.106.

[66] Al-Baghdadi MARS, Al-Janabi HAKS. Effect of operating parameters on the hygro-thermal stresses in proton exchange membranes of fuel cells. Int J Hydrogen Energy 2007;32:4510–22. https://doi.org/10.1016/j.ijhydene.2007.05.007.

[67] Carcadea E, Ismail MS, Ingham D Bin, Patularu L, Schitea D, Marinoiu A, et al. Effects of geometrical dimensions of flow channels of a large-active-area PEM fuel cell: A CFD study. Int J Hydrogen Energy 2021;46:13572–82. https://doi.org/10.1016/j.ijhydene.2020.08.150.

[68] Ahmadi N, Rezazadeh S, Yekani M, Fakouri A, Mirzaee R. Numerical investigation of the effect of inlet gases humidity on polymer exchange membrane fuel cell (PEMFC) performance. Trans Can Soc Mech Eng 2013;37:12–26. https://doi.org/https://doi.org/10.1139/tcsme-2013-0001.

[69] Samanpour H, Ahmadi N, Jabbary A. Effects of Applying Brand-New Designs on the Performance of PEM Fuel Cell and Water Flooding Phenomena. Iran J Chem Chem Eng 2022;41:618–34. https://doi.org/10.30492/ijcce.2020.130908.4225.

[70] Ashrafi H, Pourmahmoud N, Mirzaee I, Ahmadi N. Introducing a new serpentine configuration of gas channels to enhance the performance and reduce the water flooding in the PEMFC. Iran J Chem Chem Eng 2022.

https://doi.org/10.30492/IJCCE.2022.546616.5111.

[71] Wang XD, Duan YY, Yan WM. Numerical study of cell performance and local transport phenomena in PEM fuel cells with various flow channel area ratios. J Power Sources 2007;172:265–77. https://doi.org/10.1016/j.jpowsour.2007.07.026.

[72] Fontana É, Mancusi E, Da Silva A, Mariani VC, Ulson De Souza AA, Ulson De Souza SMAG. Study of the effects of flow channel with non-uniform cross-sectional area on PEMFC species and heat transfer. Int J Heat Mass Transf 2011;54:4462–72. https://doi.org/10.1016/j.ijheatmasstransfer.2011.06.037.

[73] Kumar A, Reddy RG. Effect of channel dimensions and shape in the flow-field distributor on the performance of polymer electrolyte membrane fuel cells. J Power Sources 2003;113:11–8. https://doi.org/10.1016/S0378-7753(02)00475-5.

[74] Zeng X, Ge Y, Shen J, Zeng L, Liu Z, Liu W. The optimization of channels for a proton exchange membrane fuel cell applying genetic algorithm. Int J Heat Mass Transf 2017;105:81–9. https://doi.org/10.1016/j.ijheatmasstransfer.2016.09.068.

[75] Liu Z, Zeng X, Ge Y, Shen J, Liu W. Multi-objective optimization of operating conditions and channel structure for a proton exchange membrane fuel cell. Int J Heat Mass Transf 2017;111:289–98. https://doi.org/10.1016/j.ijheatmasstransfer.2017.03.120.

[76] Ahmed DH, Sung HJ. Effects of channel geometrical configuration and shoulder width on PEMFC performance at high current density. J Power Sources 2006;162:327–39. https://doi.org/10.1016/j.jpowsour.2006.06.083.

[77] Owejan JP, Trabold TA, Jacobson DL, Arif M, Kandlikar SG. Effects of flow field and diffusion layer properties on water accumulation in a PEM fuel cell. Int J Hydrogen Energy 2007;32:4489–502. https://doi.org/10.1016/j.ijhydene.2007.05.044.

[78] Higier A, Liu H. Optimization of PEM fuel cell flow field via local current density measurement. Int J Hydrogen Energy 2010;35:2144–50. https://doi.org/10.1016/j.ijhydene.2009.12.116.

[79] Karimi S, Fraser N, Roberts B, Foulkes FR. A review of metallic bipolar plates for proton exchange membrane fuel cells: Materials and fabrication methods. Adv Mater Sci Eng 2012;2012. https://doi.org/10.1155/2012/828070.

[80] Xu Y, Peng L, Yi P, Lai X. Analysis of the flow distribution for thin stamped bipolar plates with tapered channel shape. Int J Hydrogen Energy 2016;41:5084–95. https://doi.org/10.1016/j.ijhydene.2016.01.073.

[81] Ismail MS, Berber MR, Alrowaili ZA, Pourkashanian M. Fully-developed laminar flow in trapezoidal ducts with rounded corners: a numerical solution and case study. Int J Numer Methods Heat Fluid Flow 2022;32:2682–99. https://doi.org/10.1108/HFF-09-2021-0620.

[82] Ahmadi N, Kõrgesaar M. Analytical approach to investigate the effect of gas channel draft angle on the performance of PEMFC and species distribution. Int J Heat Mass Transf 2020;152:119529. https://doi.org/10.1016/j.ijheatmasstransfer.2020.119529.

[83] Ahmadi N, Pourmahmoud N, Mirzaee I, Rezazadeh S. Three-dimensional computational fluid dynamic study of effect of different channel and shoulder geometries on cell performance. Aust J Basic Appl Sci 2011;5:541–56.

[84] Ahmadi N, Rezazadeh S, Dadvand A, Mirzaee I. Study of the effect of gas channels geometry on the performance of polymer electrolyte membrane fuel cell. Period Polytech Chem Eng 2018;62:97–105. https://doi.org/10.3311/PPch.9369.

[85] Afshari E, Jazayeri SA. Effects of the cell thermal behavior and water phase change on a proton exchange membrane fuel cell performance. Energy Convers Manag

2010;51:655–62. https://doi.org/10.1016/j.enconman.2009.11.004.

[86] Jiao K, Li X. Three-dimensional multiphase modeling of cold start processes in polymer electrolyte membrane fuel cells. Electrochim Acta 2009;54:6876–91. https://doi.org/10.1016/j.electacta.2009.06.072.

[87] Carcadea E, Varlam M, Ingham DB, Ismail MS, Patularu L, Marinoiu A, et al. The effects of cathode flow channel size and operating conditions on PEM fuel performance: A CFD modelling study and experimental demonstration. Int J Energy Res 2018;42:2789–804. https://doi.org/10.1002/er.4068.

[88] Li S, Yuan J, Andersson M, Xie G, Sundén B. Influence of anisotropic gas diffusion layers on transport phenomena in a proton exchange membrane fuel cell. Int J Energy Res 2017;41:2034–50. https://doi.org/10.1002/er.3763.

[89] Springer TE, Zawodzinski TA, Gottesfeld S. Polymer Electrolyte Fuel Cell. Kobunshi 1991;57:498–501. https://doi.org/10.1295/kobunshi.57.498.

[90] Zhang J, Wang Y, Zhang J, Liang J, Lu J, Xu L. The effect of Pt/C agglomerates in electrode on PEMFC performance using 3D micro-structure lattice models. Int J Hydrogen Energy 2017;42:12559–66. https://doi.org/10.1016/j.ijhydene.2017.03.190.

[91] Khajeh-Hosseini-Dalasm N, Kermani MJ, Moghaddam DG, Stockie JM. A parametric study of cathode catalyst layer structural parameters on the performance of a PEM fuel cell. Int J Hydrogen Energy 2010;35:2417–27. https://doi.org/10.1016/j.ijhydene.2009.12.111.

[92] Wang L, Husar A, Zhou T, Liu H. A parametric study of PEM fuel cell performances. Int J Hydrogen Energy 2003;28:1263–72. https://doi.org/10.1016/S0360-3199(02)00284-7.

[93] Gurau V, Liu H, Kakac S. Two-Dimensional Model 1998;44.

[94] Gu WB. Numerical Modeling of Coupled Electrochemical and Transport Processes in Lead-Acid Batteries. J Electrochem Soc 1997;144:2053. https://doi.org/10.1149/1.1837741.

[95] Darling RM. A Hierarchical Model for Oxygen Transport in Agglomerates in the Cathode Catalyst Layer of a Polymer-Electrolyte Fuel Cell. J Electrochem Soc 2018;165:F571–80. https://doi.org/10.1149/2.1231807jes.

[96] Soboleva T, Malek K, Xie Z, Navessin T, Holdcroft S. PEMFC catalyst layers: The role of micropores and mesopores on water sorption and fuel cell activity. ACS Appl Mater Interfaces 2011;3:1827–37. https://doi.org/10.1021/am200590w.

[97] Zamel N. The catalyst layer and its dimensionality - A look into its ingredients and how to characterize their effects. J Power Sources 2016;309:141–59. https://doi.org/10.1016/j.jpowsour.2016.01.091.

[98] Chang Y, Zhao J, Shahgaldi S, Qin Y, Yin Y, Li X. Modelling of mechanical microstructure changes in the catalyst layer of a polymer electrolyte membrane fuel cell. Int J Hydrogen Energy 2018:1–13. https://doi.org/10.1016/j.ijhydene.2018.10.157.

[99] Berning T, Djilali N. A 3D, Multiphase, Multicomponent Model of the Cathode and Anode of a PEM Fuel Cell. J Electrochem Soc 2003;150:A1589. https://doi.org/10.1149/1.1621412.

[100] Sivertsen BR, Djilali N. CFD-based modelling of proton exchange membrane fuel cells. J Power Sources 2005;141:65–78. https://doi.org/10.1016/j.jpowsour.2004.08.054.

[101] Debe MK. Electrocatalyst approaches and challenges for automotive fuel cells. Nature 2012;486:43–51. https://doi.org/10.1038/nature11115.

[102] Peuckert M. Oxygen Reduction on Small Supported Platinum Particles. J Electrochem Soc 1986;133:944. https://doi.org/10.1149/1.2108769.

[103] Malek K, Mashio T, Eikerling M. Microstructure of Catalyst Layers in PEM Fuel Cells Redefined: A Computational Approach. Electrocatalysis 2011;2:141–57. https://doi.org/10.1007/s12678-011-0047-0.

[104] Watanabe M, Saegusa S, Stonehart P. Electro-catalytic activity on supported platinum crystallites for oxygen reduction in sulphuric acid. Chem Lett 1988;17:1487–90. https://doi.org/10.1246/cl.1988.1487.

[105] Kamarajugadda S, Mazumder S. Numerical investigation of the effect of cathode catalyst layer structure and composition on polymer electrolyte membrane fuel cell performance. J Power Sources 2008;183:629–42. https://doi.org/10.1016/j.jpowsour.2008.05.072.

[106] Antolini E. Carbon supports for low-temperature fuel cell catalysts. Appl Catal B Environ 2009;88:1–24. https://doi.org/10.1016/j.apcatb.2008.09.030.

[107] Marinoiu A, Raceanu M, Carcadea E, Varlam M, Stefanescu I. Iodinated carbon materials for oxygen reduction reaction in proton exchange membrane fuel cell. Scalable synthesis and electrochemical performances. Arab J Chem 2019;12:868–80. https://doi.org/10.1016/j.arabjc.2016.12.002.

[108] Hao L, Moriyama K, Gu W, Wang C-Y. Modeling and Experimental Validation of Pt Loading and Electrode Composition Effects in PEM Fuel Cells. J Electrochem Soc 2015;162:F854–67. https://doi.org/10.1149/2.0221508jes.

[109] Owejan JP, Owejan JE, Gu W. Impact of Platinum Loading and Catalyst Layer Structure on PEMFC Performance. J Electrochem Soc 2013;160:F824–33. https://doi.org/10.1149/2.072308jes.

[110] Calili-Cankir F, Ismail MS, Berber MR, Alrowaili ZA, Ingham DB, Hughes KJ, et al. Dynamic models for air-breathing and conventional polymer electrolyte fuel cells: A comparative study. Renew Energy 2022;195:1001–14. https://doi.org/10.1016/j.renene.2022.06.092.

[111] Ercelik M, Ismail MS, Ingham DB, Hughes KJ, Ma L, Pourkashanian M. Efficient X-ray CT-based numerical computations of structural and mass transport properties of nickel foam-based GDLs for PEFCs. Energy 2023;262:125531. https://doi.org/10.1016/j.energy.2022.125531.

[112] Lee FC, Ismail MS, Ingham DB, Hughes KJ, Ma L, Lyth SM, et al. Alternative architectures and materials for PEMFC gas diffusion layers: A review and outlook. Renew Sustain Energy Rev 2022;166. https://doi.org/10.1016/j.rser.2022.112640.

[113] Okereke IC, Ismail MS, Ingham D, Hughes KJ, Ma L, Pourkashanian M. The effects of GDL anisotropic transport properties on the PEFC performance. Int J Numer Methods Heat Fluid Flow 2023;33:648–72. https://doi.org/10.1108/HFF-05-2022-0284.

[114] Aldakheel F, Ismail MS, Hughes KJ, Ingham DB, Ma L, Pourkashanian M. Effects of compression on mechanical integrity, gas permeability and thermal stability of gas diffusion layers with/without sealing gaskets. Int J Hydrogen Energy 2021;46:22907–19. https://doi.org/10.1016/j.ijhydene.2021.04.087.

[115] Tian J, Ismail MS, Ingham D, Hughes KJ, Ma L. Multiphase, three-dimensional PEM fuel cell numerical model with a variable cross-sectional area flow channel. Int J Numer Methods Heat Fluid Flow 2023. https://doi.org/10.1108/HFF-02-2023-0075.

[116] Litster William K.; Wargo, Eric A.; Kalidindi, Surya R.; Kumbur, Emin Caglan SE. Morphological Analyses of Polymer Electrolyte Fuel Cell Electrodes with Nano-

Scale Computed Tomography Imaging. Fuel Cells 2013;13:935–45. https://doi.org/NA.

[117] Carton Abdul Ghani JG. O. Three-dimensional proton exchange membrane fuel cell model: Comparison of double channel and open pore cellular foam flow plates. Energy 2017;136:185–95. https://doi.org/10.1016/j.energy.2016.02.010.

[118] Fofana Sadesh Kumar; Hamelin, Jean; Bénard, Pierre DN. Low platinum, high limiting current density of the PEMFC (proton exchange membrane fuel cell) based on multilayer cathode catalyst approach. Energy 2014;64:398–403. https://doi.org/10.1016/j.energy.2013.10.021.

[119] Ismail MS, Ingham DB, Ma L, Hughes KJ, Pourkashanian M. Effects of catalyst agglomerate shape in polymer electrolyte fuel cells investigated by a multi-scale modelling framework. Energy 2017;122:420–30. https://doi.org/10.1016/j.energy.2017.01.092.

[120] Esmaeilifar Soosan; Eikani, Mohammad H.; Ghazanfari, E. AR. Synthesis methods of low-Pt-loading electrocatalysts for proton exchange membrane fuel cell systems. Energy 2010;35:3941–57. https://doi.org/10.1016/j.energy.2010.06.006.

[121] Sasikumar J.W; Ryu, H. GI. Dependence of optimum Nafion content in catalyst layer on platinum loading. J Power Sources 2004;132:11–7. https://doi.org/10.1016/j.jpowsour.2003.12.060.

[122] Xie Titichai; Shi, Ken; Chow, Robert; Wang, Qianpu; Song, Datong; Andreaus, Bernhard; Eikerling, Michael; Liu, Zhong-Sheng; Holdcroft, Steven ZN. Functionally Graded Cathode Catalyst Layers for Polymer Electrolyte Fuel Cells II. Experimental Study of the Effect of Nafion Distribution. J Electrochem Soc 2005;152:1171–9. https://doi.org/10.1149/1.1904990.

[123] Ismail M, Ingham D, Hughes KJ, Ma L, Pourkashanian M. The effects of shape on the performance of cathode catalyst agglomerates in polymer electrolyte fuel cells A micro-scale FEM study. Int J Numer Methods Heat Fluid Flow 2016;26:1145–56. https://doi.org/10.1108/HFF-10-2015-0416.

[124] Siegel C. Review of computational heat and mass transfer modeling in polymer-electrolyte-membrane (PEM) fuel cells. Energy 2008;33:1331–52. https://doi.org/10.1016/j.energy.2008.04.015.

[125] Djilali N. Computational modelling of polymer electrolyte membrane (PEM) fuel cells: Challenges and opportunities. Energy 2007;32:269–80. https://doi.org/10.1016/j.energy.2006.08.007.

[126] Song Qianpu; Liu, Zhong-Sheng; Navessin, Titichai; Eikerling, Michael; Holdcroft, Steven DW. Numerical optimization study of the catalyst layer of PEM fuel cell cathode. J Power Sources 2004;126:104–11. https://doi.org/10.1016/j.jpowsour.2003.08.043.

[127] Marr Xianguo CL. Composition and performance modelling of catalyst layer in a proton exchange membrane fuel cell. J Power Sources 1999;77:17–27. https://doi.org/10.1016/s0378-7753(98)00161-x.

[128] Secanell B.; Suleman, Afzal; Djilali, Ned MC. Numerical optimization of proton exchange membrane fuel cell cathodes. Electrochim Acta 2007;52:2668–82. https://doi.org/10.1016/j.electacta.2006.09.049.

[129] Schwarz Nedjib DH. D. 3D Modeling of Catalyst Layers in PEM Fuel Cells Effects of Transport Limitations. J Electrochem Soc 2007;154:B1167-NA. https://doi.org/10.1149/1.2777011.

[130] Jain Lorenz T.; Jhon, Myung S. PB. Sensitivity of PEFC Models to Cathode Layer

Microstructure. J Electrochem Soc 2010;157:B1222-NA. https://doi.org/10.1149/1.3454725.

[131] Xing Xiaoteng; Alaje, T. O.; Kumar, Ravi; Mamlouk, Mohamed; Scott, Keith LL. A two-phase flow and non-isothermal agglomerate model for a proton exchange membrane (PEM) fuel cell. Energy 2014;73:618–34. https://doi.org/10.1016/j.energy.2014.06.065.

[132] Cetinbas Suresh G.; Prasad, Ajay K. FC. A. Three dimensional proton exchange membrane fuel cell cathode model using a modified agglomerate approach based on discrete catalyst particles. J Power Sources 2014;250:110–9. https://doi.org/10.1016/j.jpowsour.2013.10.138.

[133] Xing Qiong; Xu, Chenxi; Liu, Chunbo; Scott, Keith; Yan, Yongsheng LC. Numerical study of the effect of relative humidity and stoichiometric flow ratio on PEM (proton exchange membrane) fuel cell performance with various channel lengths: An anode partial flooding modelling. Energy 2016;106:631–45. https://doi.org/10.1016/j.energy.2016.03.105.

[134] Xing Shangfeng; Chen, Rui; Mamlouk, Mohamed; Scott, Keith L Du. Anode partial flooding modelling of Proton Exchange Membrane Fuel Cells: Model development and validation. Energy 2016;96:80–95. https://doi.org/10.1016/j.energy.2015.12.048.

[135] Pylypenko Tim S.; Carroll, Nick J.; Petsev, Dimiter N.; Atanassov, Plamen SO. Templated Platinum/Carbon Oxygen Reduction Fuel Cell Electrocatalysts. J Phys Chem C 2010;114:4200–7. https://doi.org/10.1021/jp909418m.

[136] Balgis Gopinathan M.; Sago, Sumihito; Ogi, Takashi; Okuyama, Kikuo RA. Nanostructured design of electrocatalyst support materials for high-performance PEM fuel cell application. J Power Sources 2012;203:26–33.

https://doi.org/10.1016/j.jpowsour.2011.11.064.

[137] Kamarajugadda Sandip SM. Generalized flooded agglomerate model for the cathode catalyst layer of a polymer electrolyte membrane fuel cell. J Power Sources 2012;208:328–39. https://doi.org/10.1016/j.jpowsour.2012.02.063.

[138] Moore Phillip; Dobson, P.; Boisvert, Jason J.; Putz, Andreas; Spiteri, Raymond J.; Secanell, Marc MW. Understanding the Effect of Kinetic and Mass Transport Processes in Cathode Agglomerates. J Electrochem Soc 2014;161:E3125–37. https://doi.org/10.1149/2.010408jes.

[139] Larminie Andrew JD. Fuel cell systems explained. vol. NA. 2000. https://doi.org/NA.

[140] Siddique Fuqiang NA. L. Process based reconstruction and simulation of a three-dimensional fuel cell catalyst layer. Electrochim Acta 2010;55:5357–66. https://doi.org/10.1016/j.electacta.2010.04.059.

[141] Jinnouchi R, Kudo K, Kodama K, Kitano N, Suzuki T, Minami S, et al. The role of oxygen-permeable ionomer for polymer electrolyte fuel cells. Nat Commun 2021;12. https://doi.org/10.1038/s41467-021-25301-3.

[142] Middelman E. Improved PEM fuel cell electrodes by controlled self-assembly. Fuel Cells Bull 2002;2002:9–12. https://doi.org/10.1016/s1464-2859(02)11028-5.

[143] Zlotorowicz A, Jayasayee K, Dahl PI, Thomassen MS, Kjelstrup S. Tailored porosities of the cathode layer for improved polymer electrolyte fuel cell performance. J Power Sources 2015;287:472–7. https://doi.org/10.1016/j.jpowsour.2015.04.079.

[144] Suter TAM, Smith K, Hack J, Rasha L, Rana Z, Angel GMA, et al. Engineering Catalyst Layers for Next-Generation Polymer Electrolyte Fuel Cells: A Review of Design, Materials, and Methods. Adv Energy Mater 2021;11. https://doi.org/10.1002/aenm.202101025.

[145] Wang M, Park JH, Kabir S, Neyerlin KC, Kariuki NN, Lv H, et al. Impact of Catalyst Ink Dispersing Methodology on Fuel Cell Performance Using in-Situ X-ray Scattering. ACS Appl Energy Mater 2019;2:6417–27. https://doi.org/10.1021/acsaem.9b01037.

[146] Sun Brant A.; Karan, Kunal WP. An improved two-dimensional agglomerate cathode model to study the influence of catalyst layer structural parameters. Electrochim Acta 2005;50:3359–74. https://doi.org/10.1016/j.electacta.2004.12.009.

[147] Yoon Adam Z. WW. Modeling Low-Platinum-Loading Effects in Fuel-Cell Catalyst Layers. J Electrochem Soc 2011;158:B1007-NA. https://doi.org/10.1149/1.3597644.

[148] Ismail Derek B.; Hughes, Kevin J.; Ma, Lin; Pourkashanian, Mohamed MS. I. Effective diffusivity of polymer electrolyte fuel cell gas diffusion layers: An overview and numerical study. Int J Hydrogen Energy 2015;40:10994–1010. https://doi.org/10.1016/j.ijhydene.2015.06.073.

[149] Ercelik M, Ismail MS, Hughes KJ, Ingham DB, Ma L, Pourkashanian M. X-ray CT-based numerical investigation of nickel foam-based GDLs under compression. Int J Hydrogen Energy 2023:1–20. https://doi.org/10.1016/j.ijhydene.2023.07.001.

[150] Calili-Cankir F, Ismail MS, Ingham DB, Hughes KJ, Ma L, Pourkashanian M. Air-breathing polymer electrolyte fuel cells: A review. Renew Energy 2023;213:86–108. https://doi.org/10.1016/j.renene.2023.05.134.

[151] Okereke IC, Ismail MS, Ingham DB, Hughes K, Ma L, Pourkashanian M. Single- and Double-Sided Coated Gas Diffusion Layers Used in Polymer Electrolyte Fuel Cells: A Numerical Study. Energies 2023;16:1–16. https://doi.org/10.3390/en16114363.

[152] Lee FC, Ismail MS, Zhang K, Ingham DB, Aldakheel F, Hughes KJ, et al. Optimisation and characterisation of graphene-based microporous layers for polymer electrolyte membrane fuel cells. Int J Hydrogen Energy 2023:1–15.

https://doi.org/10.1016/j.ijhydene.2023.05.003.

[153] Seo A, Lee J, Han K, Kim H. Performance and stability of Pt-based ternary alloy catalysts for PEMFC. Electrochim Acta 2006;52:1603–11. https://doi.org/10.1016/j.electacta.2006.03.097.

[154] Belenov S, Alekseenko A, Pavlets A, Nevelskaya A, Danilenko M. Architecture Evolution of Different Nanoparticles Types: Relationship between the Structure and Functional Properties of Catalysts for PEMFC. Catalysts 2022;12. https://doi.org/10.3390/catal12060638.

[155] Fang B, Kim JH, Kim M, Kim M, Yu JS. Hierarchical nanostructured hollow spherical carbon with mesoporous shell as a unique cathode catalyst support in proton exchange membrane fuel cell. Phys Chem Chem Phys 2009;11:1380–7. https://doi.org/10.1039/b816629c.

[156] Kim JH, Yu JS. Erythrocyte-like hollow carbon capsules and their application in proton exchange membrane fuel cells. Phys Chem Chem Phys 2010;12:15301–8. https://doi.org/10.1039/c0cp00698j.

[157] Job N, Lambert S, Chatenet M, Gommes CJ, Maillard F, Berthon-Fabry S, et al. Preparation of highly loaded Pt/carbon xerogel catalysts for Proton Exchange Membrane fuel cells by the Strong Electrostatic Adsorption method. Catal Today 2010;150:119–27. https://doi.org/10.1016/j.cattod.2009.06.022.

[158] Wang Michael; Song, Datong; Liu, Zhong-Sheng QE. Structure and performance of different types of agglomerates in cathode catalyst layers of PEM fuel cells. J Electroanal Chem 2004;573:61–9. https://doi.org/10.1016/j.jelechem.2004.06.022.

[159] Wang ZB, Zhao CR, Shi PF, Yang YS, Yu ZB, Wang WK, et al. Effect of a carbon support containing large mesopores on the performance of a Pt-Ru-Ni/C catalyst for

direct methanol fuel cells. J Phys Chem C 2010;114:672–7. https://doi.org/10.1021/jp909022j.

[160] Ismail Derek B.; Hughes, Kevin J.; Ma, Lin; Pourkashanian, Mohamed MS. I. The effects of shape on the performance of cathode catalyst agglomerates in polymer electrolyte fuel cells: A micro-scale FEM study. Int J Numer Methods Heat Fluid Flow 2016;26:1145–56. https://doi.org/10.1108/hff-10-2015-0416.

[161] Xing Mohamed; Kumar, Ravi; Scott, Keith LM. Numerical investigation of the optimal Nafion® ionomer content in cathode catalyst layer: An agglomerate two-phase flow modelling. Int J Hydrogen Energy 2014;39:9087–104. https://doi.org/10.1016/j.ijhydene.2014.03.225.

[162] Alhazmi Derek B.; Ismail, M.S.; Hughes, Kevin J.; Ma, Lin; Pourkashanian, Mohamed N. I. Effect of the anisotropic thermal conductivity of GDL on the performance of PEM fuel cells. Int J Hydrogen Energy 2013;38:603–11. https://doi.org/10.1016/j.ijhydene.2012.07.007.

[163] Rakhshanpouri Soosan S. R. Water transport through a PEM (proton exchange membrane) fuel cell in a seven-layer model. Energy 2013;50:220–31. https://doi.org/10.1016/j.energy.2012.10.053.

[164] Kamarajugadda S, Mazumder S. Generalized flooded agglomerate model for the cathode catalyst layer of a polymer electrolyte membrane fuel cell. J Power Sources 2012;208:328–39. https://doi.org/10.1016/j.jpowsour.2012.02.063.

[165] Hussain MM, Song D, Liu ZS, Xie Z. Modeling an ordered nanostructured cathode catalyst layer for proton exchange membrane fuel cells. J Power Sources 2011;196:4533–44. https://doi.org/10.1016/j.jpowsour.2010.10.111.

[166] Liang J, Li Y, Wang R, Jiang J. Cross-dimensional model of the oxygen transport

behavior in low-Pt proton exchange membrane fuel cells. Chem Eng J 2020;400:125796. https://doi.org/10.1016/j.cej.2020.125796.